

MECHANICAL BEHAVIOR OF CARBIDE-FREE  
MEDIUM CARBON BAINITIC STEEL

MECHANICAL BEHAVIOR OF CARBIDE-FREE MEDIUM CARBON  
BAINITIC STEEL

BY

XIAOXU ZHANG, B ENG

A Thesis

Submitted to the School of Graduate Studies  
in Partial Fulfilment of the Requirements  
for the Degree  
Doctor of Philosophy

McMaster University

© Copyright by Xiaoxu Zhang, January 2016



Doctor of Philosophy (2016)  
(Engineering)

McMaster University  
Hamilton, Ontario

TITLE: Mechanical Behavior of Carbide-Free Medium Carbon Bainitic Steel

AUTHOR: Xiaoxu Zhang, B. Eng. (McMaster University)

SUPERVISOR: Professor H. S. Zurob and Professor G. R. Purdy

NUMBER OF PAGES: xxv, 228

# ABSTRACT

Carbide-free bainitic (CFB) steels have gained increasing attention in recent years because of their excellent mechanical properties. The excellent combination of strength, ductility and toughness achieved in these steels is only matched by that of Maraging steels which cost 10 to 100 more than the carbide-free bainitic steels. The excellent mechanical behavior of CFB steel is mainly due its complex microstructure (bainitic ferrite, retained austenite and martensite) consisting of a high strength phase (ultra fine bainitic ferrite) and TRIP effect from retained austenite. Carbide formation is avoided due to high silicon content which suppresses cementite precipitation from austenite.

The effect of bainitic transformation time on the microstructure and mechanical properties was investigated in a steel containing 0.4%C-2.8%Mn-1.8%Si. The microstructure was characterized using optical and transmission electron microscopy; it consisted of bainitic ferrite, martensite and retained austenite. This microstructure exhibited an extended elasto-plastic transition leading to very high initial work hardening rates. The work-hardening behavior was investigated in detail using strain-path reversals to measure the back-stresses. These measurements point to a kinematic hardening due to the mechanical contrast between the microstructural constituents.

The strain aging effect at room temperature on the CFB steel was also been analyzed in great detail. The static strain aging effect at room temperature can not be overlooked in the carbide free bainitic steel. After isothermal bainite heat treatment, the yield strength of the material is increased by about 80MPa, and the ultimate tensile strength is improved by more than 100MPa after aging at room temperature for one week. This phenomenon could be related to the interactions between carbon atoms and the dislocations, grain boundaries and the residual stresses. Examination of the fracture surfaces indicated that the prior austenite grain boundaries play an important role in the fracture process.

A set of experiments were designed to study the effect of ausforming on the microstructure and mechanical properties of CFB steels. Based on its mechanical behavior under tensile tests and microstructural analysis by EBSD, the TRIP effect was contributing to the work hardening behavior. The changes in morphology and variant selection of the bainitic ferrite lath in the ausformed carbide free bainitic steel were also observed.

A new set of chemistry was design with reduced carbon and manganese content to further improve the weldability and the reproducibility of the carbide free bainitic steel.

## **ACKNOWLEDGEMENTS:**

Though only my name appears on the cover of this dissertation, a great many people have contributed to its production. I owe my gratitude to all those people who have made this dissertation possible.

My deepest gratitude is to my supervisor, Dr. Hatem Zurob. I could not have imagined having a better advisor and mentor for my Ph.D. study. He introduced me to metallurgy especially to the field of steel. His great passion and enthusiasm for science really impacts me throughout my research work. His guidance and support encourage me to explore my ideas and overcome many difficult situations.

I would like to express my sincere gratitude to my co-supervisor, Dr. Gary Purdy, for his insightful suggestions, generous help and immense knowledge. I am also thankful to him for encouraging the use of correct grammar in my writings and for carefully reading and commenting on countless revisions of this manuscript.

Besides my supervisors, my sincere thanks also goes to Dr. Joey Kish, Dr. David Embury, Dr. Olivier Bouaziz and Dr. Yves Brechet for numerous discussions, comments and lectures on related topics that helped me improve my knowledge.

I am grateful to Dr. Xiang Wang, Dr. Xiaogang Li, Doug Culley and Jim Garret for their help and support in laboratory experiments. Without their great support, it would not be possible to conduct this research. I also thank the departmental staff for their help throughout the studies.

I would like to thank my family and friends. Words can not express how grateful I am to my mother for being my strongest support throughout my 21 years of education. I would also like to thank my beloved husband Yunfei Bai, for being my companion on this experience and gives me great courage to overcome all the challenges. I would also like to thank my dearest daughter Raelyn Bai. Watching you growing up everyday reminds me all the beauty and happiness in my life. I also warmly appreciate the generosity and understanding of my parents-in-law. To my best friends, Sarah Parisio and Charmaine Silveira Da Graca Costa, I would like to thank you for listening, offering me advice and supporting me through this process.

This research would not have been possible without the financial supports from ArcelorMittal and NSERC.

This dissertation is dedicated in loving memory of my father. Thank you for always believe in me and your guiding hand on my shoulder will remain with me forever.

# Table of Contents

<b>ABSTRACT</b>	iii
<b>ACKNOWLEDGEMENTS:</b>	iv
<b>Chapter 1: Literature Review</b>	
1.1    Introduction	1
1.2    Bainite	5
1.2.1    Origin of bainite	5
1.2.2    Bainite: definition and general characteristics	6
1.2.3    Upper and lower bainite	9
1.2.4    New classification of bainite	11
1.2.5    Difference from pearlite	13
1.2.6    Growth mechanism	14
1.2.7    Incomplete reaction phenomenon	21
1.2.8    Surface relief	23
1.2.9    Crystallography	24
1.3    Carbide free bainite	26
1.3.1    Chemistry	27
1.3.2    Heat treatment procedure	33

1.3.3	Microstructure	33
1.3.4	Previous studies on carbide free bainitic steel	40
1.4	Work hardening	46
1.4.1	Kocks-Mecking Model	49
1.4.2	Residual stress	51
1.4.3	Isotropic work hardening	53
1.4.4	Kinematic work hardening	53
1.4.5	Masing Model	54
1.4.6	Bauschinger effect	55
1.4.7	TRIP effect	56
1.4.8	Strain aging	59
1.5	Fracture Behavior	60
1.5.1	Brittle Fracture	61
1.5.2	Ductile Fracture	64
1.5.3	Microscopic features of fracture	66
1.6	Ausforming	70
1.6.1	Definition	71
1.6.2	Bainite transformation kinetics change	71

## **Chapter 2: Materials and experimental methods**

2.1	Preparation of materials	73
2.2	Heat treatment procedure	73
2.2.1	Bainite treatment - two step isothermal heat treatment	73
2.2.2	Homogenization heat treatment	74
2.2.3	Prior austenite size modification heat treatment	74
2.2.4	Ausforming – thermo-mechanical treatment	76
2.3	Characterization of Microstructures	78
2.3.1	Optical Microscopy	78
2.3.2	Scanning Electron Microscopy (SEM)	79
2.3.3	Transmission Electron Microscopy (TEM)	80
2.3.4	Electron Backscatter Diffraction (EBSD)	80
2.3.5	X-ray Diffraction (XRD)	81
2.4	Characterization of mechanical behavior	81
2.4.1	Hardness test	81
2.4.2	Tensile test	81
2.4.3	Bauschinger test	82

### **Chapter 3: Bainite treatment at 300°C for different times**

3.1	Bainite transformation kinetics	84
3.1.1	CCT diagram	84



3.1.2	TTT diagram	85
3.2	Microstructures	86
3.2.1	Main phases	86
3.2.2	Banding Structure	89
3.3	Mechanical Testing Results	93
3.3.1	Tensile test results	93
3.3.2	Bauschinger tests	99
3.3.3	Strain aging of specimens 90min heat treatment	101
3.3.4	Stability of Retained Austenite	105
3.3.5	Prior austenite grain (PAG) refinement	106
3.4	Structure-Property Relationships	108
3.4.1	Work hardening behavior	108
3.4.2	Yield Strength	110
3.4.3	Masing Model	113
3.4.4	Kinematic Hardening	115
3.4.5	Kocks-Mecking Model	121
3.4.6	Banded structure	124
3.4.7	Strain Aging	125
3.4.8	Retained austenite and TRIP effect	131

3.5	Fracture behavior	135
3.5.1	Brittle Intergranular Fracture	135
3.5.2	Quasi-cleavage fracture	138
3.5.3	Ductile fracture	140
3.5.4	Retained austenite	141
3.5.5	Prior austenite grain boundary	142

#### **Chapter 4: Ausforming**

4.1	Influence on Bainite Transformation Kinetics	147
4.2	Influence on the volume fraction of bainite	150
4.3	Ausforming by Gleeble	155
4.3.1	Microstructure	157
4.3.2	Mechanical behavior and discussion	176
4.4	Ausforming by rolling	180
4.4.1	Microstructure	181
4.4.2	Mechanical behavior and discussion	185

#### **Chapter 5: New material design**

5.1	Carbon content	192
5.2	Alloying Elements	194
5.3	Chemistry design	195

## **Chapter 6: Conclusion and Future Work**

6.1	Summary of results and trends	203
6.1.1	Correlation of tensile strength with microstructure	203
6.1.2	Work-hardening response	203
6.1.3	Banding structure	204
6.1.4	Aging effect	204
6.1.5	Retained austenite and TRIP effect	205
6.1.6	Fracture behavior	206
6.1.7	Mechanical behavior of ausformed CFB	206
6.2	Conclusion	208
6.3	Future work	209
	<b>Reference</b>	<b>211</b>

## Table of Figures

Figure 1 Summary of ultimate tensile strength and total elongation data for various classes of conventional and advanced high strength steels (AHSS) [1] .....	2
Figure 2 Classification of the first and second generation of AHSS and the opportunity for the third generation of AHSS. [2] .....	3
Figure 3 Schematic illustration of the time-temperature-transformation (TTT) diagram when the C-curves of pearlite and bainite (a) overlap or (b) separate [23] .....	7
Figure 4 Schematic illustration of the morphology of a sheaf of bainite outlining the sub-units [26] .....	8
Figure 5 Schematic representation of the carbide precipitation in upper and lower bainite [29] .....	10
Figure 6 Optical micrograph of bainite microstructures in Fe-Ni-C alloys: (a) upper bainite in Fe-7Ni-0.2C (mass%), (b) lower bainite in Fe-7Ni-0.8C (mass%) [32] .....	10
Figure 7 New morphological classification based on Zajac et al.'s categorization scheme. [39] .....	13
Figure 8 Schematic illustration of the concept of $T_0$ where austenite and ferrite of the same composition have the same free energy, and the $T_0$ line on an Fe-C phase diagram [52] .....	16

Figure 9 Schematic illustration of how the $T_0$ line in the phase diagram determines bainite start temperature shown in the TTT diagram [53] .....	17
Figure 10 Schematic representation of the formation of a bainite sheaf by repeated nucleation and limited growth of sub-units and its effect on overall transformation kinetics. [52] .....	18
Figure 11 (a) atomic force microscope image of a bainite subunit and (b) atomic force microscope scan across the subunit AA', showing a tent-like surface relief of a subunit scale, taken as an evidence of diffusive growth mechanism of bainite [72] .....	24
Figure 12 Three-dimensional schematic illustration of the orientation relationship between the bainitic ferrite and the parent austenite phase [74] .....	25
Figure 13 Schematic illustration of packets of bainitic ferrite laths inside one prior austenite grain. [31] .....	26
Figure 14 Calculated transformation start temperatures of bainite and martensite phase in Fe-2Si-3Mn steel as a function of the carbon concentration. [90] .....	32
Figure 15 TEM micrograph exhibiting the fine-scale microstructure of the carbide free bainitic steel with chemical composition of Fe-0.98C-1.46Si-1.89Mn-0.26Mo-1.26Cr-0.09V (wt%), transformed at 200 °C for 15 days. The dark phase represents the austenite whereas the white	

phase is the bainitic ferrite [92] .....	34
Figure 16 Experimental data of the bainite plate thickness as a function of bainite transformation temperature (a) steels containing 0.65-0.99(wt%)C and 2-2.78(wt%)Si, with and without Cr. [94] (b) several steel compositions under isothermal heat treatment at various temperatures [95] .....	36
Figure 17 Experimental data of fracture toughness versus ultimate tensile strength for Ni alloy and Mn alloy compared with some commercial steel grades [81] .....	41
Figure 18 TEM micrograph of Fe-0.98C-1.46Si-1.89Mn-0.26Mo-1.26Cr-0.09V (wt%), transformed at 200 oC for 15 days. The dark phase represents the austenite whereas the white phase is the bainitic ferrite [113] .....	42
Figure 19 Effect of volume fraction of retained austenite and bainite transformation temperature on (a) the yield strength and (b) the ultimate tensile strength of the carbide free bainitic steel [94] .....	43
Figure 20 The combination of fracture toughness and ultimate tensile strength of the carbide free bainitic steel versus those of quenched and tempered (QT) low alloy martensitic alloys and maraging steels [9] .....	45
Figure 21 Schematic illustration of the stress-strain curve and the strain hardening rate curve, both the strength and ductility are increased with upward shift of the strain hardening rate curve due to work hardening .....	49

Figure 22 Schematic sketch of hardening rate versus flow stress illustrating the hardening stages for polycrystals in comparison to those for single crystals deformed in single slip [128].....	51
Figure 23 Illustration of concentration distribution in blocky and filmy retained austenite [16].....	57
Figure 24 Schematic illustration of the plastic zone in front of the crack tip [136] .....	61
Figure 25 Schematic illustration of the repeated initiation cleavage cracks throughout grains at the crack tip [88] .....	62
Figure 26 Schematic illustration of (a) cleavage crack in traditional dual phase or TRIP steel, (b) quasi-cleavage crack in carbide free bainitic steel [14] .....	63
Figure 27 Section through the neck area of a tensile specimen of copper showing cavities and crack formed at the center of the specimen as the result of void coalescence. [138].....	67
Figure 28 Feather pattern on a single grain of a chromium steel weld metal that failed by cleavage [135].....	68
Figure 29 Fracture surface from a ferritic steel failed by cleavage showing a sharply defined river pattern with arrow indicating the crack propagation direction. [142].....	68
Figure 30 SEM fractography of the fracture surface of a high-purity, coarse-grained	

Al-4.2Cu alloy with intergranular facets at low magnification (10x) [144] ....	70
Figure 31 Heat treatment process .....	74
Figure 32 Prior austenite grain refinement by thermal cycling .....	75
Figure 33 Prolonged austenitization for higher grain size of prior austenite.....	75
Figure 34 Ausforming experiment procedure with hot rolling .....	77
Figure 35 Ausforming experiment procedure with Gleeble .....	78
Figure 36 Bauschinger Test and offset method .....	82
Figure 37 CCT diagram of the steel with 0.4C-2.8Mn-1.8Si (wt%) chemical composition [156].....	85
Figure 38 TTT diagram of the steel with 0.4C-2.8Mn-1.8Si (wt%) chemical composition [157].....	86
Figure 39 Microstructure of the banded specimens isothermally transformed at 573K(300oC) for (a) 30, (b) 60, (c) 90 and (d) 120 minutes. ....	87
Figure 40 TEM micrograph of a specimen that was austenitized at 1133K(860oC) for 10 min and isothermally transformed at 573K(300oC) for 30 minutes. The microstructure consists of bainite, martensite and retained austenite. ....	89
Figure 41 Severe banding appears in the carbide free bainitic steel due to the high Mn content. ....	91
Figure 42 Microstructure of the homogenized specimens isothermally transformed at	



573K(300oC) for (a) 30, (b) 60, (c) 90 and (d) 120 minutes. ....	92
Figure 43 Effect of the bainitic transformation time on the engineering stress-strain curves of the (a) banded and (b) homogenized steels. ....	94
Figure 44 Fracture surface of the banded specimens transformed at 573K(300oC) for (a) 30, (b) 60, (c) 90 and (d) 120 min. ....	96
Figure 45 engineering stress-strain curves of the specimens heated at 300oC for 30 minutes .....	99
Figure 46 (a) True stress-strain curves obtained from the strain-reversal tests on the homogenized specimens that were transformed at 573K(300oC) for 120 minutes. (b) Back-stress measurements using the 0.01% off-set method for the same steel for homogenized and banded steel transformed under the same conditions. ....	100
Figure 47 engineering stress-strain curves of the specimens heated at 300oC for 90 minutes and aged at room temperature for different periods of time .....	101
Figure 48 Fracture surfaces of the specimens transformed at 573K(300oC) for 90 min and then aged at room temperature for (a) 1 hour, (b) 1day and (c) 7days. ....	104
Figure 49 Retained austenite films are imaged in (a) bright field and (b) dark field in a cold-rolled specimen which was transformed for 90 minutes at 573K(300oC) and cold-rolled to an equivalent strain of 0.3. ....	106

Figure 50 TEM of prior austenite grain [159] .....	107
Figure 51 Fracture surface after (a) prolonged austenitizing, (b) regular heat treatment and (c) thermal cycling .....	108
Figure 52 (a) Work-hardening rate as a function of the bainitic transformation time in the homogenized specimens, (b) the calculated fraction of the material which has yielded ( $f$ in Eq. 2). .....	109
Figure 53 Comparison between the original F-curve and the Avrami fit curve for the specimen after 30 minutes of bainite transformation.....	117
Figure 54 Linear relationship between bainite transformation time and $n/\sigma_0$ .....	117
Figure 55 Avrami equation to fit the Volume fraction of elements in the plastic regime of specimens after bainite transformation for 30, 60, 90 and 120 minutes at 300°C .....	118
Figure 56 Probability density distribution function of elements with different yield stress levels for specimens after bainite transformation for 30, 60, 90 and 120 minutes at 300°C .....	119
Figure 57 Work-hardening rates of the homogenized specimens as a function of (a) the applied stress and (b) the reduced stress ( $\sigma - \sigma_y$ ). .....	122
Figure 58 Work-hardening rate as a function of the aging time at room temperature for specimens after bainite treatment for 90 minutes .....	127

Figure 59 The comparison of the stress vs. strain curves in tension and in compression of the specimen after the same heat treatment (a) isothermal at 300oC for 30 minutes, (b) isothermal at 300oC for 120 minutes .....	129
Figure 60 Dilation curves showing the effect of ausforming at low temperature on bainitic transformation. [187] .....	153
Figure 61 Full martensite structure in the sample after 25% plastic strain of ausforming in compression at isothermal transformation temperature of 300°C and directly quenched to room temperature. (a) an overview in low magnification, (b) lath martensite with high dislocation density and (c) fine scale twins in plate martensite [191] .....	154
Figure 62 (a) The hardness profile throughout the heating zone and (b) the width and thickness of the designed tensile samples with the calculated hardness x cross section area.....	156
Figure 63 Optical micrographic images for carbide free bainitic steel after ausforming in tension with strain of 0% followed by (a) 30 minutes and (b) 60 minutes holding; with strain of 10% followed by (c) 30 minutes and (d) 60minutes; with strain of 20% followed by (e) 30 minutes and (f) 60 minutes at 300oC. Bainite: bright phase; martensite/austenite: dark phase.....	158
Figure 64 Volume fraction of bainitic ferrite measured by manual line intercept method	

.....	159
Figure 65 The orientation maps of (a) the non-ausformed specimen under bainite transformation for 60 minutes; (b) the specimen ausformed (10% strain) in tension before bainite transformation for 30 minutes; (c) the specimen ausformed (10% strain) in tension before bainite transformation for 60 minutes; (d) the specimen ausformed (20% strain) in tension before bainite transformation for 60 minutes.....	161
Figure 66 Phase map of the carbide free bainite (red, bainitic ferrite; blue, austenite) on (a) the non-ausformed specimen under bainite transformation for 60 minutes; (b) the specimen ausformed (10% strain) in tension before bainite transformation for 30 minutes; (c) the specimen ausformed (20% strain) in tension before bainite transformation for 60 minutes at 300oC. ....	162
Figure 67 bainitic ferrite lath thickness for specimens after ausforming by 10% and 20% pre-strain followed by isothermal bainite heat treatment at 300oC for 30 or 60 minutes compared to the non-ausformed specimen with same bainite heat treatment .....	162
Figure 68 Aspect ratio (length/thickness) of bainitic ferrite of the ausformed carbide free bainitic steel .....	163
Figure 69 TEM micrographs of specimens after ausformation (a) 10% prior compression	

followed by isothermal heat treatment at 300oC for 30 minutes and (b) 25% prior compression followed by isothermal treated at 300oC for 1 hour [191]	164
Figure 70 TEM micrographs in high magnifications showing great dislocation density in the ausformed specimen (25% prior compression followed by isothermal treated at 300oC for 1 hour) [191]	165
Figure 71 TEM images (left image) and corresponding SAD patterns (right image) for (a) dark area with SAD pattern showing fcc lattice structure (austenite) and (b) bright area with SAD pattern showing bcc lattice structure (bainitic ferrite or martensite) [191]	166
Figure 72 DF images taken from an austenite reflection of specimen with or without ausformation followed by isothermal bainite treatment at 300oC for 30 minutes (a) without ausforming, (b) ausformed in compression by 10%, (c) ausformed in compression by 25% [191]	168
Figure 73 EBSD orientation map of the specimen (20% of strain followed by 60 minutes at 300oC)	171
Figure 74 The interlocking structure of austenite (dark region) and ferrite (bright region) mixture in specimen with prior compression by 25% at 300oC and then isothermal transformation at 300oC for 1 hour [191]	171

Figure 75 Pole figures obtained from single austenite grain in ausformed specimen (20% pre-strain followed by 60 minutes at 300oC) of (a) austenite, (b) bainitic ferrite type A and (c) bainitic ferrite type B .....	173
Figure 76 Pole figures obtained from single austenite grain in ausformed bainite (pre-strain of 10% followed by isothermal heat treatment at 300oC for 30 minutes): (a) retained austenite and (b) bainitic ferrite.....	174
Figure 77 The true stress vs. strain curves are plotted for specimens with 0% and 20% of ausforming strain followed by bainite isothermal heat treatment at 300oC for 60 minutes.....	177
Figure 78 Work-hardening rate of the specimen after 60 minutes of isothermal heat treatment with 0 and 20% strain of ausforming by Gleeble .....	178
Figure 79 Fracture surface of the specimens transformed at 573K(300oC) for 60 minutes by Gleeble with deformation of (a) 0% strain and (b) 20% strain in tension	179
Figure 80 Optical micrographic images for carbide free bainitic steel after bainite transformation at 300oC for 90 minutes (a) after ausforming by rolling at 350°C and (b) without ausforming. Bainite: bright phase; martensite/austenite: dark phase. ....	182
Figure 81 SEM images for transformed product after ausforming by rolling at 350°C in (a) lower and (b) higher magnifications. Darker region: bainitic ferrite; Brighter	

region: martensite/austenite. ....	182
Figure 82 EBSD micrographs of the carbide free bainite microstructure with ausforming by rolling at 350°C with austenite in white. (a) before the tensile test and (b) after the tensile test. ....	184
Figure 83 engineering stress-strain curves of the specimens heated at 300oC for 90 minutes with and without ausforming by rolling.....	186
Figure 84 Work-hardening rate of the specimen after 90 minutes of isothermal heat treatment with and without ausforming by rolling .....	187
Figure 85 SEM image on the fracture surface topography on the specimen after bainite heat treatment at 300oC for 90min (a) without ausforming and (b) with ausforming .....	190
Figure 86 A summary of the ultimate tensile strength of carbide free bainitic steel with different carbon content. ....	193
Figure 87 CCT diagram of alloy #1 .....	198
Figure 88 CCT diagram of alloy #2.....	198
Figure 89 CCT diagram of alloy #3.....	199
Figure 90 CCT diagram of alloy #4.....	199
Figure 91 CCT diagram of alloy #5.....	200
Figure 92 CCT diagram of alloy #6.....	200

Figure 93 CCT diagram of alloy #7 .....	201
Figure 94 CCT diagram of alloy #8 .....	201



# **1 Literature Review**

## **1.1 Introduction**

The automobile industry is facing big challenges in our time to reduce the weight of modern cars while keeping high crash safety standards. Weight reduction of automobiles needs to happen in order to fulfill customer expectations related to gas consumption and meet government regulations on CO<sub>2</sub> emission. The application of high strength steel is very encouraging in the automobile industry, making steel sections thinner without compromising performance, hence reducing CO<sub>2</sub> emissions due to mass savings. Moreover, modern car parts are designed in more complicated shapes, requiring good formability and ductility of steel. Accordingly, an excellent combination of strength and ductility is crucial in the industrial application of steel. The advanced high strength steel (AHSS) is designed to not only reach higher strength, but may also have some improvement in its ductility and formability. Steel is designed to have a multi-phase microstructure with the mixture of harder and softer phases like the composite material. The first generation of AHSS includes dual phase steel (DP steel). The low yield point and good ductility of dual phase steel is the result of the soft ferrite phase, while a high ultimate tensile strength is due to the hard martensite as the second phase in the microstructure. The second generation of AHSS is a group of austenitic

steel grades containing a relatively high amount of manganese content. It includes high manganese TRIP (transformation induced plasticity) steel and high manganese TWIP (twinning induced plasticity) steel. The high manganese TRIP or TWIP steel grades perform much better ductility and formability in comparison to the 1<sup>st</sup> generation of AHSS, while keeping ultra high tensile strength (above 700MPa) as shown in the Figure 1 below. Their extraordinary combination of strength and ductility is a result of the occurrence of the phase transformation or the twinning phenomena during plastic deformation. [1]

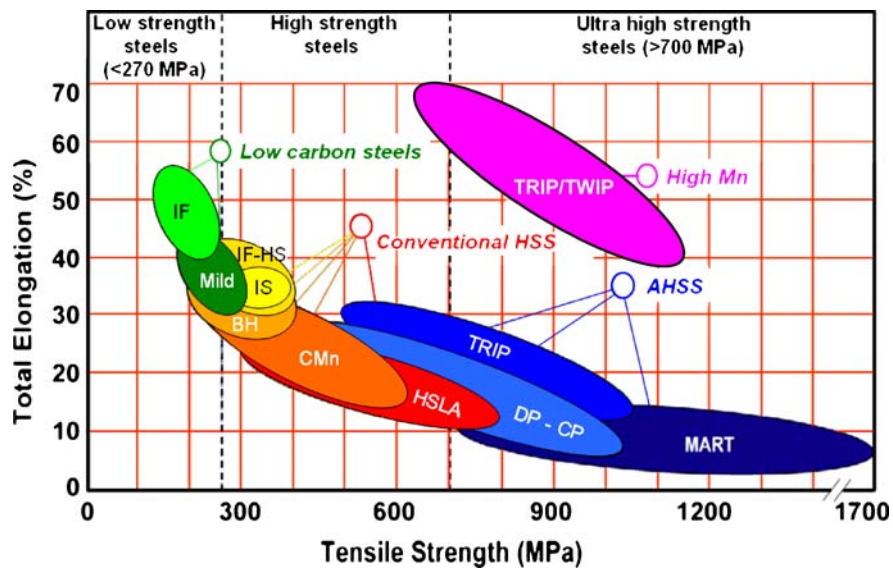
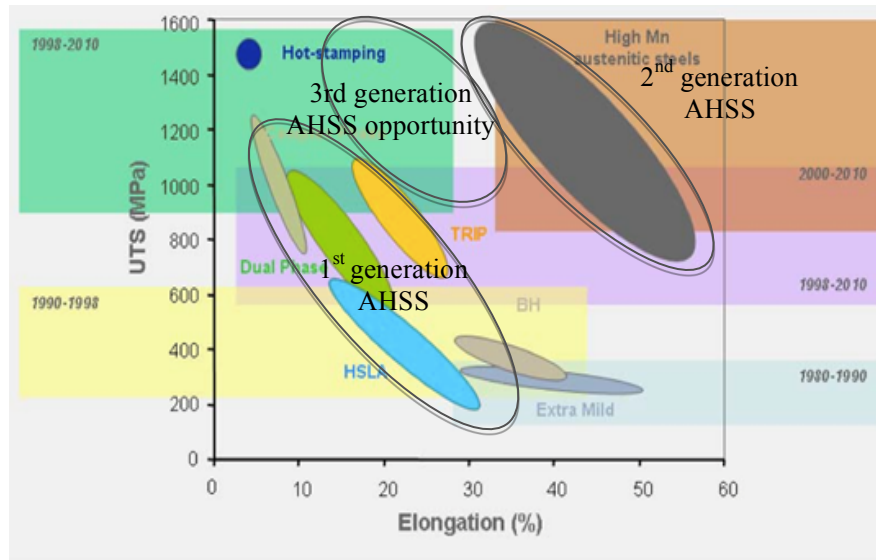


Figure 1 Summary of ultimate tensile strength and total elongation data for various classes of conventional and

advanced high strength steels (AHSS) [1]



**Figure 2 Classification of the first and second generation of AHSS and the opportunity for the third generation of AHSS. [2]**

The second generation of the automobile high strength steel (High Mn TRIP/TWIP steel) with tremendous improvements in both strength and ductility, as shown in Figure 2 above, was considered a great success. However, these steel grades have not been commercially applied for automobile industry yet. The high Mn steel is poor in corrosion resistance because the main chemical component manganese is electrochemically reactive in chloride and the acidic solution. [3] Moreover, Mn tends to form an oxidized layer on the surface of the steel product that reduces the quality of coating by hot-dip galvanizing. [3] It is also much more expensive than conventional steel grades due to its high alloy content. [1] On the contrary, the hot-stamping steel has been

successfully applied commercially to automobile industry worldwide, to attain a combination of drastic weight reduction and strong crash performance. The hot stamping (hot-forming or die quenching) is a thermo-mechanical forming process while a steel sheet is heated up in the furnace and then pressed and quenched to room temperature simultaneously to form a martensitic part. [4-6] The hot stamping process fabricates automotive members such as a center-pillar that requires tensile strength above 1000MPa. However, there are still some limitations involved in this hot pressed steel grades including welding issues, expensive or insufficient coating, relatively insufficient residual ductility for energy absorption during crashes and expensive processing costs. [4] Thus, there is an opportunity for a new generation of automobile steel. The third generation of AHSS is expected to fill the gap between the first and second generation steel grades in Figure 2 with a better combination of strength and ductility compared to the first generation automobile steel grades. Moreover, the 3<sup>rd</sup> generation of AHSS needs to have good weldability and formability for low-cost cold stamping process. The 3<sup>rd</sup> generation of the automobile high strength steel typically contains a lower amount of austenite stabilizers (Mn, Ni, Cu) compared to the 2<sup>nd</sup> generation automobile steel, for better corrosion resistance and lower cost. On the other hand, the 3<sup>rd</sup> generation AHSS may require more complicated alloy design and annealing process compared to the conventional 1<sup>st</sup> generation. Since the microstructure of the 3<sup>rd</sup> generation needs to be

multi-phase and ultra-fine for a significant improvement in strength, while maintaining good ductility and formability. Carbide free bainitic steel (CFB) as one of the potential candidates for the 3rd generation automobile high strength steel is meeting all those criterions by a relatively simple heating procedure.

Carbide-free bainitic steels have attracted much attention due to their excellent combination of strength and ductility [7]. The key to these excellent properties appears to be the fine-scale microstructure which consists of nano-scale bainitic ferrite and retained austenite plates. In order to obtain these microstructures it is necessary to carry out the bainitic transformation at low temperatures. A key requirement is, therefore, a chemistry which suppresses the martensite-start temperature ( $M_s$ ). In addition, high silicon (Si) content is needed to suppress cementite precipitation and retain the austenite [8-10]. The first generation of ultra-fine bainitic steels contained up to 0.8 wt%C [11]. A new generation of compositions, with lower carbon content and better weldability, was later developed by various groups [12-19]. The new compositions contain 0 to 0.4%C, 1.5 to 3%Mn and 1.5 to 2.0% Si.

## **1.2 Bainite**

### **1.2.1 Origin of bainite**

In the late 1920's, bainite was first identified in steel by Davenport and Bain, who

reported the achievement of a constituent by isothermal heat treatment after ausnitening. The heat treatment temperature was above that at which martensite transformation took place, and below that at which pearlite formed. The constituent was, hence, initially named “martensite-troostite” due to its similarity to martensite; subsequently, it was renamed “Bainite” after E. C. Bain. The microstructure of bainite, which consisted of an “acicular, dark etching aggregate”, was also distinguishable from martensite and pearlite phases. [20] The bainite got more attention later due to its mechanical properties been discovered to be “tougher for the same hardness than tempered martensite”.

### **1.2.2 Bainite: definition and general characteristics**

The bainite phase forms at intermediate temperatures between those of diffusive pearlite and displacive martensite. The bainite transformation from austenite is time dependent, which means that the volume fraction of bainite under a given isothermal bainite transformation temperature increases as a sigmoidal function of time. Accordingly, the bainite transformation kinetics or progress is represented by a C-curve in the time-temperature-transformation (TTT) diagrams (Figure 3). [21] There may be some overlap between the C-curves of bainite and pearlite, and in some extreme cases, there is only one set of C-curve shown in the TTT diagram. On the contrary, martensite transformation occurs extremely quickly when reaching the required  $M_s$  temperature. The transformation of martensite is also classified to be athermal since no thermal

activation is needed, and it is independent of time. As a result, martensite transformation appears as straight lines parallel to the time axis in the TTT diagrams. [22]

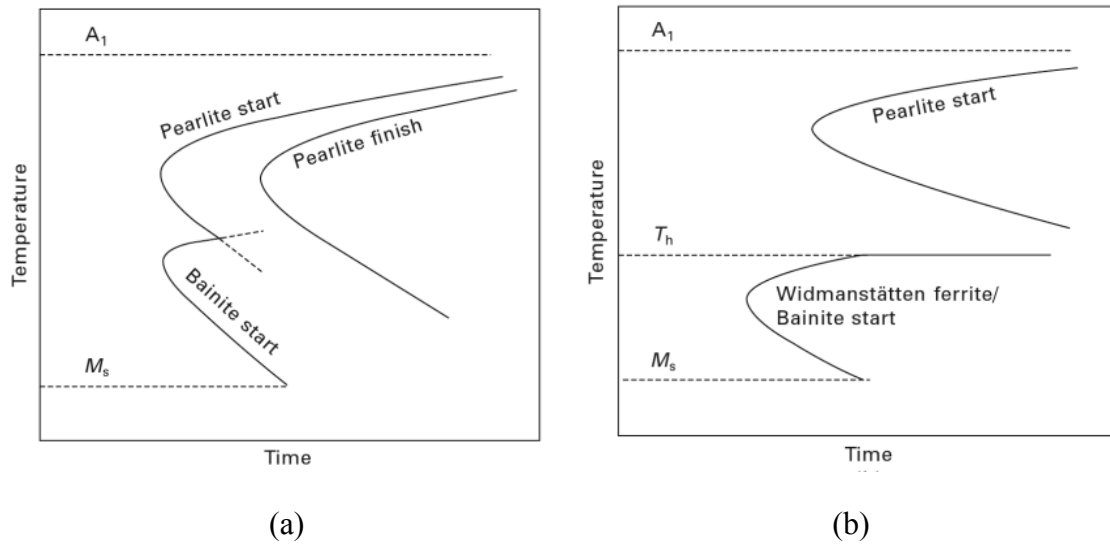


**Figure 3 Schematic illustration of the time-temperature-transformation (TTT) diagram when the C-curves of pearlite and bainite (a) overlap or (b) separate [23]**

Put simply, bainite is a “non-lamellar aggregate of lath or plate-shaped ferrite and carbide”. [20, 24, 25] The term bainitic ferrite stands for the ferrite component in bainite. Bainite is composed of lath or plate-shaped bainitic ferrite grains that are also sometimes called subunits. These lath-like or plate-like subunits nucleate adjacent to each other and grow with similar crystallographic orientations to form a close-packed clusters of subunits. These close-packed clusters are called sheaves. [26] A schematic representation of a characteristic bainitic sheaf is shown in Figure 4. The austenite grain boundaries, seen in Figure 4, hinder the growth of bainitic sheaves and the component subunits. [26]

The close-packed subunits in each sheaf are characterized by almost identical crystallographic orientation and low-angle grain boundaries between each adjacent subunit. [27] These fine-scale subunits may not be resolved by an optical microscope, and the thickness of each subunit decreases with decreasing transformation temperature. [26, 28] Cementite precipitates inside or between subunits depending on the bainite transformation temperature and the carbon content of the steel. Other phases including untransformed austenite and martensite occupy the regions between the subunits or sheaves in thin-film or granular form. [27]

Typically, bainite is classified into two categories: upper bainite and lower bainite that form at upper and lower temperature ranges, respectively, and have distinctive morphological differences. [29]

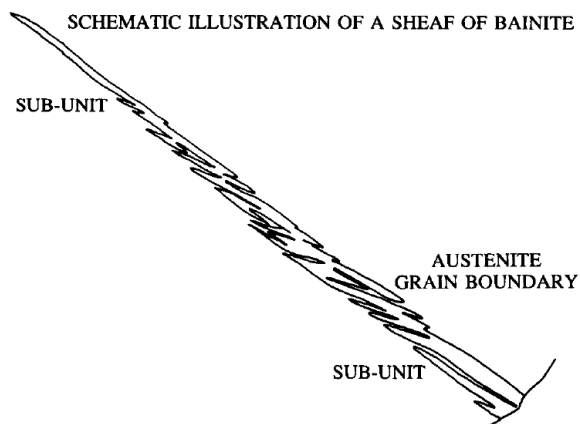


**Figure 4 Schematic illustration of the morphology of a sheaf of bainite outlining the sub-units [26]**



### 1.2.3 Upper and lower bainite

The classification of bainite is based on the morphological differences in the phases formed at different transformation temperature ranges. These differences include variations in the size and shape of subunits and the carbide distribution. The latter attribute is the principal variant used to define and distinguish between upper and lower bainite.

Upper bainite forms at a higher temperature; as the temperature decreases, lower bainite forms instead. In upper bainite, carbide only forms between ferrite subunits resulting in inter-lath carbide dispersion, while the ferrite subunits remain free of carbide precipitation. In the lower bainite, on the other hand, carbide precipitates both between subunits (inter-lath carbide) and within individual ferrite subunits. This latter process, seen in Figure 5, forms intra-lath carbides in the lower bainite. [24] Moreover, both the bainitic ferrite grain size and shape change with the bainite transformation temperature. The driving force that promotes the formation of nucleation sites of bainitic ferrite is greater with a decrease in bainite transformation temperature. As a result, the ferrite grains in lower bainite are finer than those in upper bainite. [30]

The morphology of upper bainite is feather-like (as shown in Figure 6(a)). Each bainitic ferrite subunit is in the shape of a lath or needle, which nucleates primarily at the prior austenite grain boundaries. [31] On the contrary, the lower bainite is composed of finer

bainitic ferrite grains in the form of a plate. These ferrite crystals not only nucleate at the prior austenite grain boundaries but also within the austenite grain as seen in Figure 6(b). [32] The shape of bainitic ferrite may also change from lath-like to plate-like due to an increase of carbon content. [33] This nomenclature of upper and lower bainite is widely used in industry. [24]

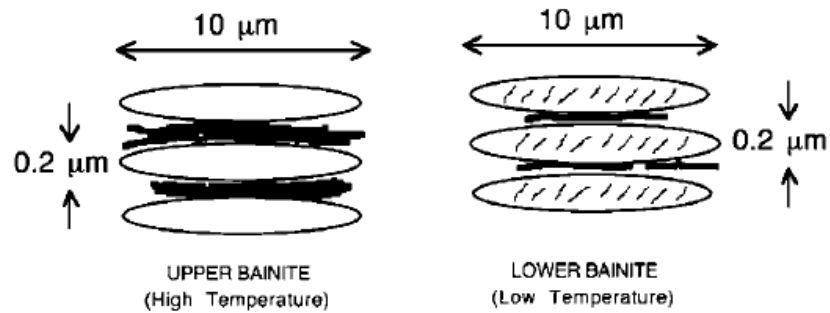


Figure 5 Schematic representation of the carbide precipitation in upper and lower bainite [29]

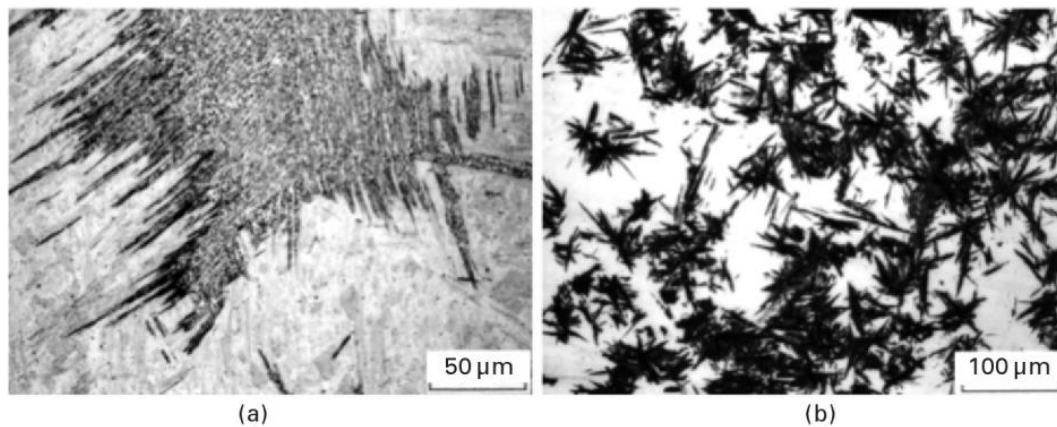


Figure 6 Optical micrograph of bainite microstructures in Fe-Ni-C alloys: (a) upper bainite in Fe-7Ni-0.2C (mass%), (b) lower bainite in Fe-7Ni-0.8C (mass%) [32]

### **1.2.4 New classification of bainite**

The classical term of both the upper and lower bainite is for the bainite composed of the acicular ferrite grain as the leading phase and carbide. Over time, some other less familiar but more complex microstructures are referred to as “bainite” including granular bainite[34], columnar bainite[35] and inverse bainite[36]. The granular bainite, as the most accepted term of those three, is formed during a continuous cooling process in low-carbon, low-alloy steels. Granular bainite appears as a coarse granular or equiaxed ferrite matrix composed of dispersed islands of martensite and/or retained austenite (M/A constituent) when observed on an optical scale. [34] Its blocky morphology diverges from that of the ordinary upper and lower bainite with acicular bainitic ferrite grains. Coarse granular bainite results from gradual bainite transformation during continuous cooling or coiling, particularly at a slow cooling rate. Later studies on granular bainite using the electron microscope identify sheaves of bainitic ferrite with thin films of austenite between the subunits. This experimental result suggests that the nature of the blocky ferrite matrix in granular bainite is the same as that of the classical bainite. [37]

Carbides, the main component in upper and lower bainite, can be inhibited with sufficient addition of alloying elements such as silicon or aluminum to the steel. The final carbide-free acicular ferrite matrix is comparable to the conventional bainite with carbide precipitation since they both consist of aggregates of fine-scale ferrite laths or plates.

The aforementioned matrix is, therefore, classified as carbide-free bainite for its retention of austenite in the inter-lath replacing carbide precipitation. The retained austenite is stabilized at room temperature due to the carbon dissipation from the adjacent ferrite phase. A new classification system of bainite is proposed according to the bainitic ferrite matrix morphology and the type of distribution of second phases including carbide and M/A constituent. [24, 27, 38]

Recently, Zajac *et al.* provide a more unified terminology of bainite. [39] The new classification system can be applied to both low carbon and high carbon bainitic steel including granular bainite and carbide free bainite (Figure 7). The new classification divides bainite into three main groups: granular bainite, upper bainite and lower bainite. Zajac *et al.* define upper bainite as the lath-like ferrite with inter-lath second phases including cementite and martensite/austenite (M/A) film. This upper bainite that contains M/A fine films instead of the carbide is also called carbide free bainite. Second, lower bainite is the lath-like or plate-like ferrite with cementite or carbide inside the ferrite subunits. Lower bainite is divided into two subgroups according to the bainitic ferrite morphology. The first is the lath morphology, typical of low carbon steel grade, and the second is plate morphology attributed to steel with higher carbon content. [39]

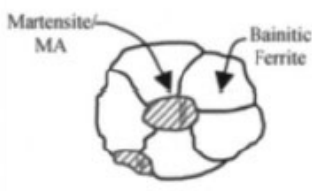
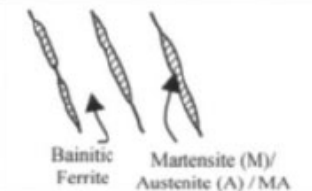
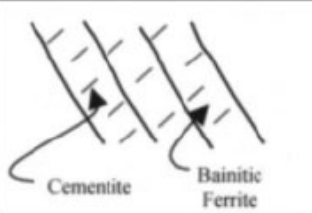
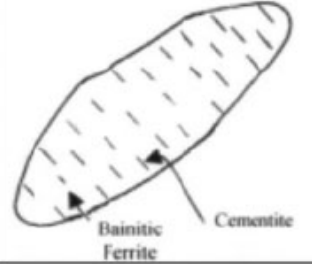
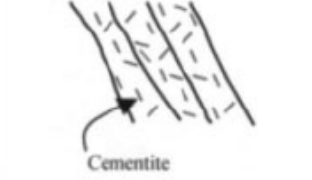
Bainite	Morphology	Bainite description
<b>Granular bainite</b>	Irregular ferrite with M/A.	
<b>Cementite-free lath-like upper bainite</b>	Lath-like ferrite with M/A on lath boundaries.	
<b>Lath-like lower bainite</b>	Lath-like ferrite with cementite inside the ferrite laths	
<b>Plate-like lower bainite</b>	Plate-like ferrite with cementite inside the ferrite plates	
<b>Lath-martensite</b>	Tempered lath martensite	

Figure 7 New morphological classification based on Zajac et al.'s categorization scheme. [39]

### 1.2.5 Difference from pearlite

Bainite is distinct from pearlite in structure, nucleation and growth mechanism despite both deriving from eutectoid transformation of ferrite and carbide. Compared to the

acicular or needle-like microstructure of bainite, the ferrite and carbide form a lamellar morphology in pearlite. The ferrite phase nucleates first followed by the precipitation of carbide inside or between each bainitic ferrite lath in bainite, whereas pearlite is nucleated by carbide precipitation followed by ferrite formation. [40, 41] The ferrite and carbide grow cooperatively at the same rate in pearlite, while these two phases grow independently in bainite. [42]

### **1.2.6 Growth mechanism**

Bainite transformation occurs at the intermediate temperature range between that of widmanstatten ferrite occurring at a higher range and of the martensite phase at a lower range. Widmanstatten ferrite is formed by diffusion, while martensite grows displacively. The mechanism of bainite transformation exhibits some characteristic features of both diffusive and displacive transformation. Bainite morphology, transformation velocity, surface relief and incomplete reaction phenomenon resemble those of widmanstatten ferrite and martensite. For this reason, the controversy over the bainite transformation mechanism in steel has lasted decades since its discovery in the late 1920s. This ongoing debate centers on is two alternative theories to explain the fast growth of the bainitic ferrite phase. The first theory posits a diffusional transformation, in which a diffusion controlled lateral mechanism is used to describe the bainite growth, similar to that observed for Widmanstatten ferrite growth from austenite. The other

theory is the displacive, diffusionless model to describe the bainite growth. In this view, bainite formation is comparable to martensite transformation. Nowadays, with the improvement in characterization technologies, more results and shreds of evidence are provided to support or contradict either of these two theories. However, a consensus has not been reach as to which theory is the correct one.

### **1.2.6.1 Displacive Mechanism**

The displacive theory was first proposed by Hultgren in 1926. [43] It is reasonable to suggest that the origin of this theory is mainly influenced by the similarity of morphology between bainite and martensite. Subsequently, based on this theory, other groups described the bainite transformation as the rapid growth of bainitic ferrite laths fully-supersaturated with carbon. The carbon is then thought to be subsequently discarded from the ferrite to form carbide. [44-47] The growth rate of bainitic ferrite is slower than that of martensite but is faster than classical diffusion-controlled ferrite growth. [48-50] According to this theory, the bainite transformation is under a shear mechanism. The displacive transformation mechanism involves corresponding motion of atoms across a glissile interface and an invariant plane shear strain caused by the shape change during the formation of bainite. The parent phase austenite adjacent to the bainite subunits formed by shear deforms plastically to release the large shape strain. The growth of bainite is fully diffusionless or displacive, even though the carbon

diffusion is taking place at the nucleation stage under paraequilibrium condition. The concept of  $T_0$  temperature is refers to the temperature at which both austenite and ferrite of the same composition have the same free energy, as illustrated in Figure 8. Thus, the  $T_0$  line is the upper limit for bainite formation (bainite start temperature  $B_s$ ) since it is thermodynamically impossible for the bainite transformation to occur above this temperature. (Figure 9) The existence of the strain energy due to shape deformation during bainite growth needs to be overcome by supercooling below the  $T_0$  temperature. As a result, the  $T_0$  line is shifted to be  $T_0'$  temperature, taking account the strain energy of 400J/mol that is calculated and measured by Bhadeshia. [51]

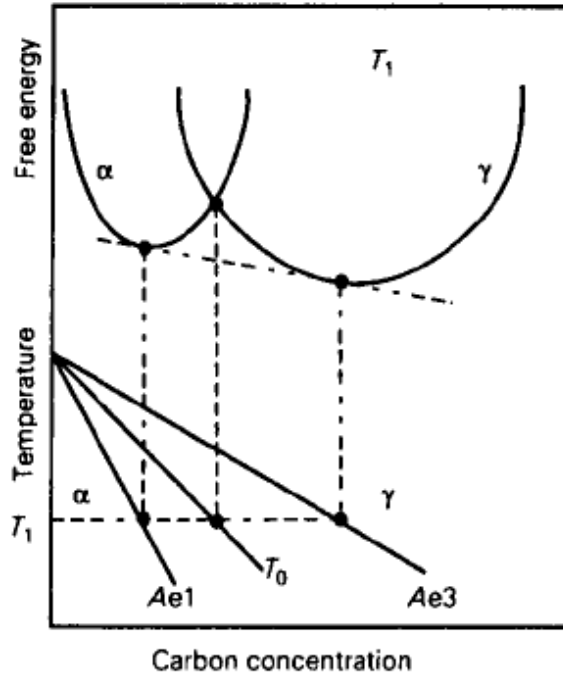
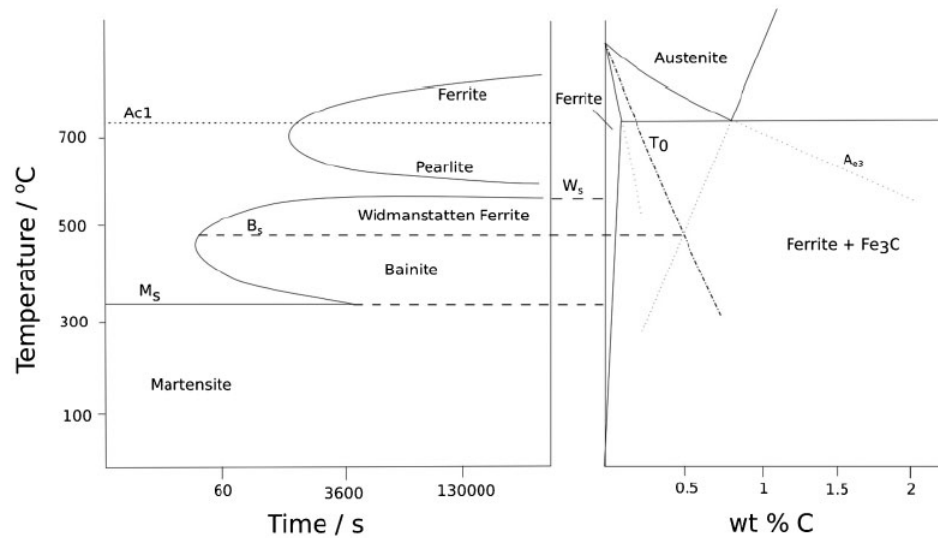


Figure 8 Schematic illustration of the concept of  $T_0$  where austenite and ferrite of the same composition have the same free energy, and the  $T_0$  line on an Fe-C phase diagram [52]





**Figure 9 Schematic illustration of how the  $T_0$  line in the phase diagram determines bainite start temperature shown in the TTT diagram [53]**

Since the austenite phase adjacent to the bainite subunits is under plastic relaxation, the dislocation density is increased to stifle the movement of the glissile interface during bainite transformation. [54] As a result, the growth of a subunit is hindered by the increasing amount of dislocations created at the growth front, and a new subunit is nucleated instead at the tip of the existing one. The formation mechanism of a sheaf is this repeated cycle of rapid growth of subunits by shear followed by nucleation of subunits controlled by carbon diffusion. Consequently, the lengthening rate for each sheaf is much less than that for individual subunits (Figure 10), taking into account the time consumed for each subunit to slow down and stop growing and for the new subunits to nucleate. [52] This overall transformation rate of bainite is slower than that of

martensite. Therefore, the volume fraction of bainite increases with a rise of the bainite transformation time at a given temperature, resulting in a sigmoidal relationship between the amount of bainite formed and the isothermal bainite transformation time. [23]

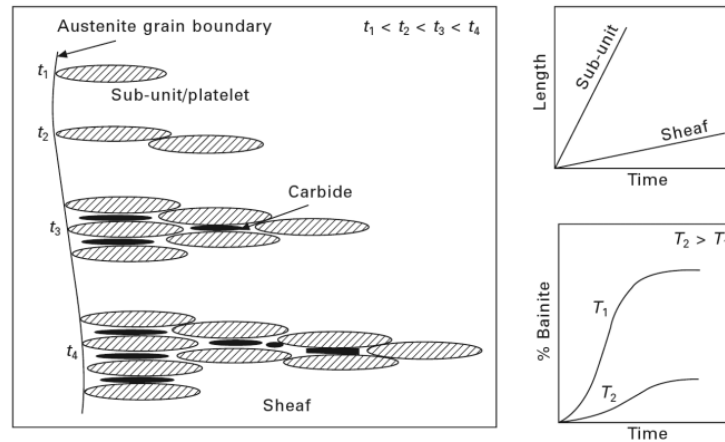


**Figure 10 Schematic representation of the formation of a bainite sheaf by repeated nucleation and limited growth of sub-units and its effect on overall transformation kinetics. [52]**

In the view of the displacive formation of bainite, the carbon content is the same in the freshly formed bainitic ferrite and the parent austenite. Each bainitic ferrite subunit is supersaturated with carbon at first. After its formation, carbon is rejected from bainitic ferrite due to its negligible carbon solubility and precipitates to form carbides inside or between subunits, or dissipates into the adjacent residual austenite. [23] The formation of ferrite subunits and the carbide precipitation in bainite is non-cooperative, according to the school supporting the displacive mechanism theory.

### **1.2.6.2 Diffusive Mechanism**

Originally, the diffusive theory of bainite transformation is attributed to Robertson in 1929. [55] He compared bainite with pearlite and suggested that the growth of both constituents is controlled by diffusion. The differences of crystallography between these two phases are presumed due to pearlitic ferrite being nucleated by carbide, and to bainitic ferrite being nucleated directly from austenite. According to this theory, the diffusion-controlled growth mechanism of bainitic ferrite is not essentially different from that of widmanstätten ferrite. [29, 55-58] The bainitic and widmanstätten ferrite both grow by diffusion of carbon in this theory. As a result, the bainitic and widmanstätten ferrite transformation are continuous represented by one C-curve in the TTT diagram (Figure 9).

The rate of transformation of the bainitic ferrite and that of the widmanstätten ferrite is much faster than idiomorphic ferrite due to its edge-wise growth mechanism. [49, 50, 59, 60] The ferrite precipitates from the austenite phase are bounded by interfaces with different degree of coherency between the parent and the product phase. The coherent or semi-coherent interfaces are immobile and are unable to migrate in the normal direction, and act as strong growth barriers for bainitic ferrite. [61] The incoherent interface, on the other hand, is very mobile with poor matching of the lattice structures between the austenite and ferrite phases. Ferrite subunits can grow much faster

diffusively along the lateral direction. The interface at the ledge is incoherent, and atoms can bond freely to the migrating ledge interface. [62] Due to the immobile coherent or semi-coherent interfaces and its ledge-wise growth mechanism, the bainitic ferrite grains are in the platelike or lathlike shape. [63] Numbers of experimental studies have been done on this edge-wise diffusional growth mechanism of bainitic ferrite by different approaches including in-situ hot stage optical microscopy. The growth rate of bainite is comparable to the ledgewise growth rate of widmanstatten ferrite. [60] Additionally, numbers of experimental evidence show that the lengthening of bainitic ferrite plates and the growth of sheaf take place at a constant rate. [26, 49, 59, 64, 65]

Thermodynamically, Hultgren proposed “paraequilibrium”: a metastable pseudo-equilibrium state in which substitutional alloy elements do not diffuse. Meanwhile, carbon diffusion is still fast enough during the bainite growth, and is thought to attain a constrained local (interfacial) equilibrium. [56] Other research groups also found evidence that the bainitic ferrite growth rate is comparable to the ledgewise growth of widmanstatten ferrite. Accordingly, the fast growth rate of bainitic ferrite can be achieved by the diffusion-controlled growth mechanism. [60] During the edgewise growth of bainitic ferrite lath or plates, the sidewise diffusion of carbon from ferrite to the parent austenite and the precipitation of carbide are taking place simultaneously. In upper bainite, the cementite or carbides are precipitated at the carbon enriched austenite

inter-lath films. [28, 66] In the case of lower bainite, carbide precipitation occurs adjacent to the edge-wise lengthening bainitic ferrite and triggers the thickening of the bainitic ferrite. Thus, the bainitic ferrite and carbide are forming cooperatively in lower bainite at the growth rate controlled by diffusion of carbon. [23]

### **1.2.7 Incomplete reaction phenomenon**

One of the typical characteristic features of bainite is its “incomplete reaction phenomenon” or “transformation stasis”. During isothermal bainite heat treatment, as the bainite phase reaches its maximum volume fraction, the bainite transformation ceases. There is a considerable amount of retained austenite that remains untransformed, and the composition of carbon in the remaining austenite does not reach its paraequilibrium value. This bainite transformation is, therefore, incomplete. This premature cessation of bainite transformation causes the maximum volume fraction of bainitic ferrite to be less than the theoretical value. The theoretical maximum volume fraction of bainitic ferrite can be calculated by the lever rule based on the paraequilibrium phase diagram. As a result, there is still a considerable amount of austenite that remains untransformed that may transform to martensite or retain in the austenite state under cooling to room temperature. The maximum volume fraction of bainite increases with decreasing bainite transformation temperature. [51, 67]

In the view of diffusive-control theory, the incomplete reaction phenomenon is explained

by solute drag effect. Nevertheless, the substitutional alloying atoms do not participate in the partitioning procedure during bainite transformation due to their low diffusivities. These alloy elements are thermodynamically attracted by the interface between bainitic ferrite and austenite to reduce the overall free energy level. The segregation of the substitutional solute atoms at the interface applies a dragging force to the migrating interface of bainitic ferrite. This drag effect varies with the temperature that it is more effective at the lower temperature range. As the bainite transformation progresses, the dragging force continuously increases with the increasing amount of segregation at the interface. Consequently, the growth of bainitic ferrite is retarded and further ceased when the dragging force is greater than the chemical driving force of ferrite formation at the bainite transformation temperature. [62, 68] In the future, more detailed analysis is expected to confirm how influential the solute drag effect is to the transformation stasis of bainite. The high-resolution analysis can be achieved by atom probe or scanning transmission electron microscopy (STEM) analysis.

According to the displacive mechanism theory of bainite transformation, plastic deformation of the austenite is cooperating with the formation of bainite due to its shape change. Plastic deformation introduces induced stress or strain, and the dislocation debris into the austenite phase. These stabilize the parent austenite phase from further transforming to bainite. Correspondingly, the maximum volume fraction of bainite is,

therefore, less than the theoretical value. This mechanical stabilization of austenite phenomenon is also observed in martensite with same transformation mechanism as that of bainite.

### **1.2.8 Surface relief**

Surface relief on a pre-polished free surface is found for martensite, bainite and widmanstatten ferrite. [69, 70] For martensite, the surface relief is caused by invariant plane strain (IPS) due to shear during transformation. [54, 71] However, the surface relief phenomenon is also found possible for widmanstatten ferrite formed with diffusional ledge-wise growth mechanism. Since the ferrite transformation from austenite is associated with volume expansion, the ferrite grain is constrained to keep coherency at the ferrite-austenite interface, thus inducing surface relief at the free surface. Moreover, the existence of ledges at the free surface can also be relieved. STM and AFM research has found a “tent-like” surface relief of a bainite subunit as evidence of the edgewise diffusion mechanism of bainitic ferrite formation. [72]

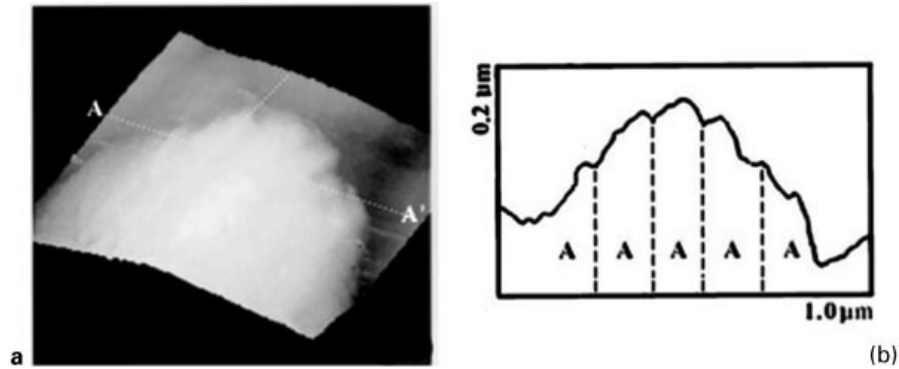


Figure 11 (a) atomic force microscope image of a bainite subunit and (b) atomic force microscope scan across the

subunit AA', showing a tent-like surface relief of a subunit scale, taken as an evidence of diffusive growth

mechanism of bainite [72]

## 1.2.9 Crystallography

Sandvik conducted a systematic study of the crystallography of bainitic ferrite using transmission electron microscopy (TEM) in 1982. The orientation relationship between bainitic ferrite and austenite closely follows the classical Kurdjumov-Sachs (K-S) relationship and the Nishiyama-Wasserman (N-W) relationship. The average ferrite/austenite orientation relationship is represented by  $(111)_\gamma // (011)_\alpha$ ,  $[\bar{1}01]_\gamma \sim 4 \pm 1^\circ$  from  $[\bar{1}\bar{1}1]_\alpha$ , where the K-S relationship is  $(111)_\gamma // (011)_\alpha$ ,  $[\bar{1}01]_\gamma // [\bar{1}\bar{1}1]_\alpha$  and the N-W relationship is expressed as  $(111)_\gamma // (011)_\alpha$ ,  $[101]_\gamma // [\bar{1}00]_\alpha$ . The bainite crystallography in three-dimension is observed by Moritani later in 2003 by TEM and the measured ferrite orientation relationships with the parent austenite phase correspond to those reported by Sandvik. Figure 12 illustrates the 3D crystallography of the bainitic ferrite



schematically. [73, 74]

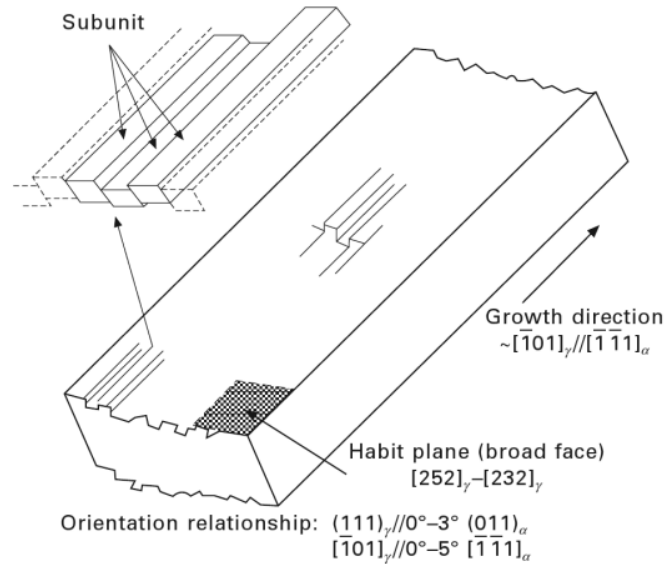


**Figure 12 Three-dimensional schematic illustration of the orientation relationship between the bainitic ferrite and the parent austenite phase [74]**

As mentioned above, all of the subunits in each sheaf share almost identical orientation following one of the variants in the Kurdjumov-Sachs(K-S) relationship. Each prior austenite grain is composed of numbers of parallel close-packed packets or substructures as shown schematically in Figure 13. [31] The crystallography of bainitic ferrite resembles that of martensite and widmanstatten ferrite. These three product phases all share the same orientation relationships (Kurdjumov-Sachs) with the parent austenite phase. [66, 75, 76]

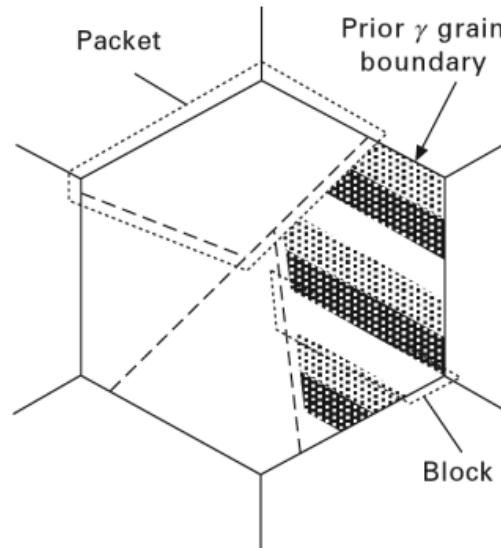


Figure 13 Schematic illustration of packets of bainitic ferrite laths inside one prior austenite grain. [31]

### 1.3 Carbide free bainite

Studies by Irvine and Pickering in the 1960's have established that the mechanical performance of conventional bainitic steels cannot reach up to that of quenched and tempered martensitic steels. [77] The relatively poor fracture behavior of bainite is due to the existence of brittle cementite or carbide in the microstructure. Cracks initiate at matrix/carbide interfaces under the influence of the external stress accompanied by dislocation slips and pile-ups. [78] The carbide phase as the potential crack nucleation site does not play a desirable role in conventional bainite, bringing some limitation of the industrial application of the conventional bainite. This is the primary motivation for studying the carbide free bainite. [79]

The existence of coarse and brittle carbides in bainitic steel can be prohibited by the

addition of ~2wt% silicon to steel to improve the ductility and fracture toughness. The excessive carbon atoms are ejected from the bainitic ferrite to enrich the neighboring residual austenite making it stable at room temperature. [80] Carbide free bainitic steel performs very good mechanically both in strength and fracture toughness. Its performance is comparable to other commercial steel grades with much higher alloy content, including the maraging steel. The maraging steel is strengthened by intermetallic alloy carbide precipitation during tempering of martensite to achieve both strength and ductility. [81, 82] Maraging steel is expensive due its high alloy composition and is used in golf club heads and missile skins. [83]

### **1.3.1 Chemistry**

#### **1.3.1.1 Silicon**

The commercial application of conventional bainite is limited because of the undesirable, coarse and brittle carbides in its microstructure. Carbide has been shown to be detrimental to fracture strength and toughness since it is one of the main contributors to the early cleavage fracture and crack and damage initiation. [8, 80] As a carbide-inhibitor, silicon in the steel suppresses and prevents carbide precipitation during bainite formation, leading to the carbide-free product. The precipitation of carbide or cementite is suppressed by the minimum of 1.5wt% of silicon. [84] The solubility of silicon is

negligible in carbide. The free energy change associated with the carbide precipitation is reduced tremendously due to the silicon trapped inside the carbide, making it less thermodynamically favorable to precipitate. The mobility of this substitutional atom is limited at the bainite transformation temperature range. The precipitation of carbide is significantly retarded since it involves the partition of silicon atoms from carbide to the parent phase during the growth of bainite. Due to the large reduction in carbide precipitation kinetics, the carbide formation can be prohibited by the addition of silicon to the bainite steel. For carbide free bainitic steels, instead of carbide precipitation, carbon diffuses into and enriches the neighboring austenite film instead. As a result, the mechanical and thermal stability of retained austenite are increased due to the carbon enrichment. [8, 79, 80, 85]

#### **1.3.1.2 Mn**

Manganese is added to ensure good hardenability of the material. “Hardenability” is defined as the ability of the steel to resist pearlite and proeutetoid ferrite formation while cooling after austenitization. Alloying elements act as the austenite-stabilizer to postpone or delay the time required for austenite decomposition in steel. Good hardenability allows the austenitized steel to be cooled at a relatively slow rate and form bainite without any pearlite formation. There are two ways to reduce the rate of decomposition. Steel can be hardened by either reducing the nucleation rate or the

growth rate of pearlite and proeutetoid ferrite. One of the main purposes of adding substitutional alloying element to steel is to increase its hardenability. It allows slower cooling rates to produce martensite with no pearlite or ferrite formation. Pearlite transformation time increases with the introduction of increasing amounts of the Mn alloy to steel. [41]

#### **1.3.1.2.1 Mn Segregation and banding structure**

One of the biggest problems associated with the addition of Mn is its segregation during the solidification step of casting. During solidification, the diffusivity of the solute in the solid phase cannot keep up with the fast cooling rate and is negligible compared to that in the liquid phase. Therefore, it is assumed, in most cases, that there is no diffusion in solid phase during solidification. The composition of the alloy element at the solidification front of the solid/liquid interface follows the solidus line in the phase diagram as the casting process proceeds. Correspondingly, the alloy element distribution in the as-cast material is heterogeneous. The degree of segregation depends not only on the cooling rate during casting, but also on the slope of the solidus line. The intensity of partition from liquid to solid at the initial and the final stages of solidification correspond to the level of segregation of alloying elements. For manganese, concentration at the core of a dendrite that solidifies in the initial stage is much lower than in the inter-dendrite regions that solidify last. The mobility of manganese as the

substitutional solute in steel is very limited due to its low diffusion coefficient. Respectively, the heterogeneous distribution of Mn cannot be eliminated after forging and hot rolling. Instead, it gives a macroscopic scale banding structure in the final bainite microstructure. [41]

During bainite transformation from the austenite phase, the manganese as an austenite-stabilizer influences the start temperature of austenite decomposition ( $A_{r3}$  temperature). The higher concentration of Mn correlates with the decreasing  $A_{r3}$  temperature. [86] Subsequently, as the cooling start from the austenitization temperature range, bainite forms first in the low-Mn regions with a higher  $A_{r3}$  temperature. The austenite bands enriched with manganese at a lower  $A_{r3}$  temperature transform to ferrite at a later stage or shear to form martensite. The Mn segregation influences not only the microstructure but also the carbon distribution. The regions mainly composed of bainitic ferrite are low in carbon since the carbon solubility is negligible in ferrite. Instead, the martensite bands are enriched in carbon due to the carbon partitioning from the adjacent bainitic ferrite bands.

Thompson and Howell's study on the banding structure in steel with 1.4wt% Mn demonstrates that the intensity of the banding structure can be reduced by increasing the cooling rate from the austenite temperature range. As a result, the time differences between the bainite transformation at the segregated bands with different Mn

concentration are reduced. [87]

### **1.3.1.3 Carbon**

Carbon is the main interstitial solute atom in steel; it makes a significant contribution to the solid solution strengthening of the material. The strength of a material increases when the movement of the dislocation is inhibited or hindered. The carbon strengthening mechanism results from the attractive or repulsive energy between the slipping dislocations and the adjacent carbon atoms. The energy associated with the interaction between dislocations and the carbon atoms obstructs the mobility of the dislocation. [88] Steel with higher strength can be achieved by increasing its carbon content as illustrated in the Equation 1 below. Flow stress  $\tau$  is proportional to  $c^{1/2}$  where  $\gamma$  is a constant, while  $G$  is the young's modulus and  $c$  is the concentration of carbon. [88, 89]

$$\tau \cong \gamma G c^{1/2} \qquad \text{Equation 1}$$

The bainite start temperature ( $B_s$ ) is the highest temperature at which bainite formation can take place in a steel grade with a given composition. The martensite start temperature ( $M_s$ ) is equally defined as shown in Figure 9. The bainite start temperature ( $B_s$ ) and the martensite start temperature ( $M_s$ ) decrease as the carbon content in the material increases. [90] To avoid martensite formation, the bainite transformation

temperature cannot be lower than the  $M_s$  temperature of the given steel grade.

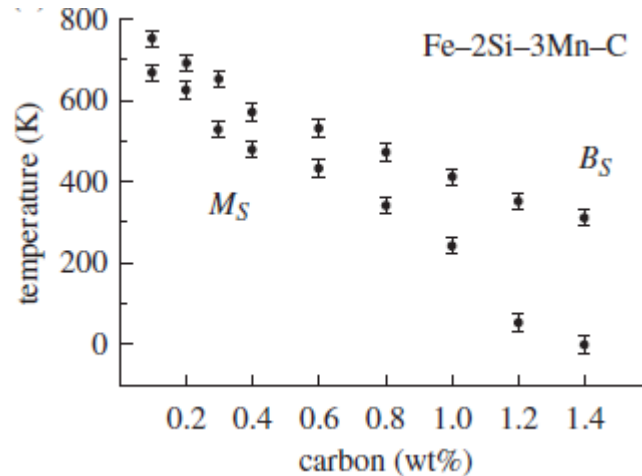


**Figure 14** Calculated transformation start temperatures of bainite and martensite phase in Fe-2Si-3Mn steel as a function of the carbon concentration. [90]

Welding is one of the most common fabrication or sculptural process that joins steel. When welding steel parts together, an extremely severe thermal cycle is applied to the alloy reaching its melting point before cooled to room temperature. Since steel absorbs heat effectively as a strong thermal sink, the cooling rate after heating is very high, and the temperature gradient is steep in the heat-affected zone. The major problem in welding on steels is the formation of martensite after the severe heating and cooling thermal cycle. During heating, hydrogen atoms in the environment diffuse rapidly into the heat-affected zone of the material. When martensite forms during cooling, hydrogen atoms are dissipated from martensite due to its low solubility and migrate to the prior austenite grain boundaries. Under residual stress after welding, hydrogen at boundaries



weakens the lattice structure and acts as the crack initiation site. The existence of hydrogen is usually difficult to avoid due to humidity in the air. On the other hand, the carbon content of steel should be designed low enough to prevent martensite formation during welding, to prevent early failure of the welded part. [41] As a result, the low carbon steels are preferable for industrial application because of their good weldability. [91]

### **1.3.2 Heat treatment procedure**

The heating procedure for carbide free bainitic steel is not different from conventional bainite production. Carbide free bainite can be formed by continuous cooling to room temperature after austenitization, or by 2-step isothermal treatment (full austenitization above  $A_{e3}$  temperature followed by cooling to bainite transformation temperature for a period of time). The cooling rate needs to be controlled in both heat treatment approaches to avoid pearlite formation while cooling from austenitization temperature.

### **1.3.3 Microstructure**

#### **1.3.3.1 Main phases**

Carbide free bainite is composed of fine plates or laths of bainitic ferrite and inter-plate or inter-lath carbon-enriched films of austenite as shown in Figure 15. Because carbide

formation is suppressed, carbide free bainitic steel is more resistant to cleavage fracture and crack initiation. [8]

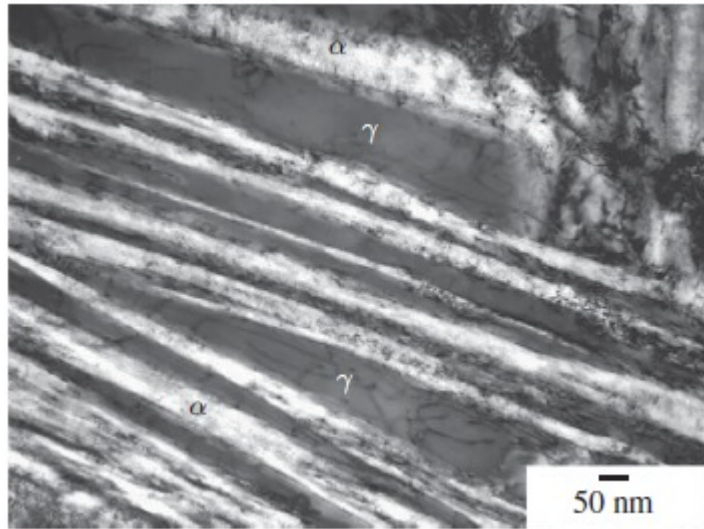


**Figure 15 TEM micrograph exhibiting the fine-scale microstructure of the carbide free bainitic steel with chemical composition of Fe-0.98C-1.46Si-1.89Mn-0.26Mo-1.26Cr-0.09V (wt%), transformed at 200 °C for 15 days. The dark phase represents the austenite whereas the white phase is the bainitic ferrite [92]**

Retained austenite is the soft and tough phase that leads to a decrease in the yield strength. [93] During isothermal bainite heat treatment, austenite in the microstructure takes one of two forms: a block or a thin film. The blocky retained austenite locates between the packets of bainite subunits. The thin film shaped residual austenite is separated by the bainitic ferrite lath within each packet. By replacing carbide, austenite films between the bainitic ferrite laths are enriched with carbon in the carbide free bainite. The carbon-enriched retained austenite in thin films is stabilized at room temperature. Under

deformation, the relatively soft austenite in the microstructure enhances the toughness but reduces the strength of carbide free bainite. [80] Depending on the degree of stability of the austenite, the strength and the toughness of the material may be further improved by transformation induced plasticity effect (TRIP effect). [9]

The blocky austenite, on the other hand, has a larger grain size and is much less stable; it tends to transform into martensite when cooled to room temperature or at the early stage of deformation. As a result, the soft austenite is replaced by brittle martensite that reduces fracture resistance and toughness. [80] Efforts should, therefore, be made to reduce the volume fraction of the blocky austenite.

The amount of the thin film austenite positively correlates to the volume fraction of bainite, thus the greater the ratio of the film austenite over the blocky austenite. By decreasing the isothermal bainite heat treatment temperature, the volume fraction of bainite increases and the bainite laths are finer. As a result, carbide free bainite can be made to achieve greater toughness with a decrease in the bainite transformation temperature. [80]

The thickness of the bainitic ferrite plate or lath corresponds to the bainite transformation temperature. The bainite lath or plate thickness lessens with reduced transformation temperatures. [91] Figure 16 illustrates the expansion of bainite plate thickness with increasing bainite transformation temperature in several steel compositions.

High-carbon carbide free bainitic steel with relatively lower  $M_s$  temperature allows the bainite transformation to take place at lower temperatures, and consequently provides greater supercooling to form finer bainite. On the contrary, platelets of bainite tend to form in coarser morphology in the steel with low carbon content.

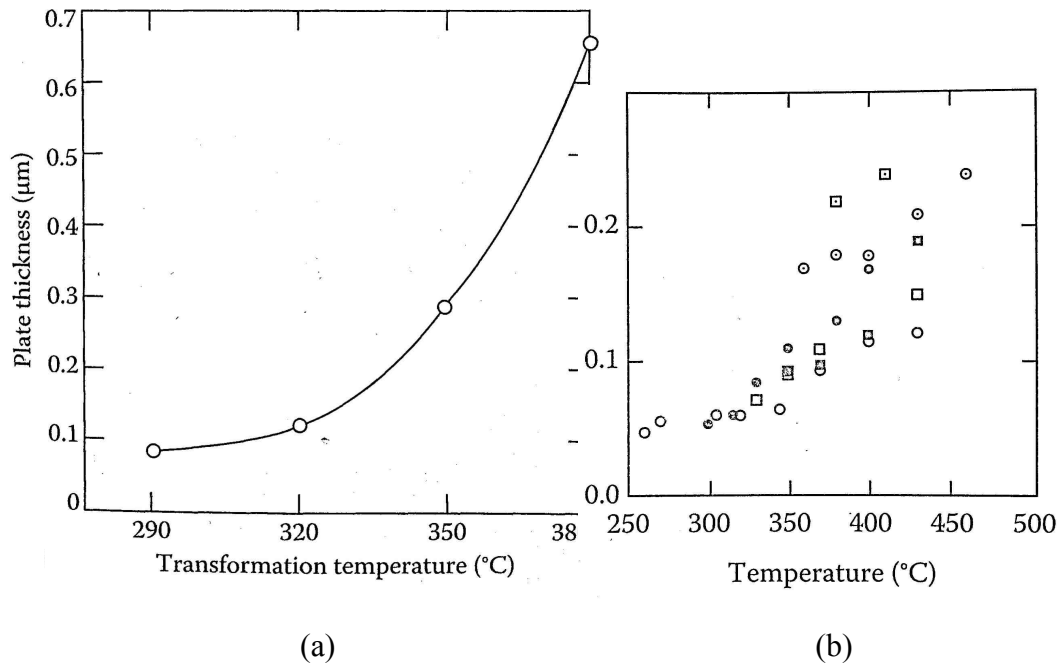


Figure 16 Experimental data of the bainite plate thickness as a function of bainite transformation temperature (a)

steels containing 0.65-0.99(wt%)C and 2-2.78(wt%)Si, with and without Cr. [94] (b) several steel compositions under isothermal heat treatment at various temperatures [95]

The Hall-Petch equation (Equation 2) shows the correlation between yield stress  $\sigma_y$  and the grain size  $d$  of a polycrystalline material. The yield strength is linearly proportional to  $d^{1/2}$ . According to the Hall-Petch effect, there is an increase in strength with a decrease in grain size  $d$  of the bainitic steel that can be achieved by reducing bainite

transformation temperature.

$$\sigma_y = \sigma_o + k d^{-1/2} \quad \text{Equation 2}$$

### 1.3.3.2 Dislocation density in bainitic ferrite

The high dislocation density in bainitic ferrite lath has been observed experimentally with the use of hot-stage TEM. Such observations show that the growth of bainite is accompanied by the dislocation formation in and around each bainitic ferrite lath. [96] A dislocation density has been estimated by TEM imaging on bainitic steel transformed at 300 °C to be  $5.1 \pm 2.7 \times 10^{14} \text{ m}^{-2}$ . [97] The displacive theory of bainite transformation may relate to the high dislocation density found in carbide free bainite. According to displacive theory, a shape change is accompanying the shear transformation of the bainitic ferrite. The microstructure possesses a relatively high amount of dislocation debris, due to plastic deformation adjacent to the ferrite subunits. [85] Some studies also suggest that the product bainite phase inherits the defects in the parent austenite. [51, 98, 99] The dislocation density of bainitic ferrite is higher with descending bainite reaction temperature. [100] Moreover, the dislocation density in the bainitic ferrite is found to be greater than that in the polygonal and widmanstatten ferrites, as these two phases transform at a higher temperature. [79]

### **1.3.3.3 Carbon distribution**

The carbon enriched retained austenite stabilized at room temperature in carbide free bainitic steel makes considerable contributions to its excellent mechanical behavior. Since carbide formation is inhibited in this type of steel, it is thermodynamically favorable for carbon to partition from bainitic ferrite to the adjacent austenite. Consequently, the stability of austenite is improved from martensite transformation at room temperature. On the other hand, the paraequilibrium carbon content in ferrite is negligible at bainite isothermal holding temperature and room temperature. Since the mobility of carbon is very high at the bainitic transformation temperature, it only takes a few milliseconds for the supersaturated carbon content to diffuse from the lath-like or plate-like bainitic ferrite grains to the neighboring inter-lath austenite. [101] However, a previous study using internal friction techniques shows that the carbon content in bainitic ferrite is higher than its paraequilibrium value. [102] Later, atom-probe field-ion microscope techniques further confirm the unexpected supersaturation of carbon in bainitic ferrite. [103-107]

This carbon supersaturation in carbide free bainitic ferrite may correspond to its transformation mechanism. In the displacive theory, the carbon diffusion is not involved in the formation of bainitic ferrite. Instead, the carbon atoms are trapped inside the product ferrite phase, similar to martensite transformation. However, in the case of

bainite formation, carbon partitions into the neighboring austenite immediately after the formation of bainitic ferrite laths. As a result, the carbon content in the final bainitic ferrite phase should follow its paraequilibrium concentration at a given temperature. Another approach to explain the supersaturation phenomenon in ferrite is to relate it to the relatively high dislocation density in the bainitic ferrite. The interstitial carbon atoms attract themselves to the dislocations or defects inside each bainitic ferrite lath causing supersaturation of carbon in the bainitic ferrite phase. This binding to dislocations behavior is a competing reaction with the partitioning from bainitic ferrite to austenite. Researchers suggest that the carbon atom is trapped by dislocations and forms a carbon cluster in the vicinity of a dislocation. This is also called Cottrell atmosphere. [108]

The carbon supersaturation in bainitic ferrite has some influence on the final microstructure and the mechanical behavior of the carbide free bainite. It is correlated with the “incomplete reaction phenomenon” where the formation of bainite ceases before reaching the volume fraction calculated by lever rule. [109] Carbon distribution in bainitic ferrite and retained austenite affect the final volume fraction of the untransformed austenite at the end of the bainite heat treatment, as well as its stability at room temperature. The mechanical behavior of carbide free bainitic steel is also correlated with the carbon distribution in its microstructure, because the strength of the bainitic ferrite, as the main constituent in the compound matrix, is prone to the effects of its

carbon concentration. The TRIP effect, which will be discussed in great detail in the next section, is strongly influenced by the stability of retained austenite that is governed by its carbon content. Furthermore, the interactions between interstitial carbon atoms and the dislocations or defects in the material may also have a strain aging effect, similar to that in martensite, which cannot be overlooked during mechanical analysis.

### **1.3.4 Previous studies on carbide free bainitic steel**

As discovered in 1970, the introduction of silicon to steel can slow down or even inhibit the formation of carbide. [84] In the 1980's, Bhadeshia and Edmonds, [7, 79] and Miihkinen and Edmonds [110, 111] conducted numerous studies on carbide free bainitic steel. Their studies primarily focus on the effect of additional silicon on the transformation kinetics, microstructure and mechanical behavior of bainitic steel. [7, 79] The first generation of carbide free bainite with a 0.2-0.4wt% carbon content shows promising mechanical results with an excellent combination of both strength and ductility. Under tensile test, the ultimate tensile strength of the material reaches up to 1420MPa while the elongation is 22%. Moreover, it possesses extraordinary fracture toughness after simple isothermal bainite heat treatment for 30-60 minutes. [7] The combination of strength and fracture toughness, shown in Figure 17, approaches that of 18wt% Ni maraging steel that is a high alloy steel grade hardened by intermetallic alloy carbides in martensite during tempering. [82, 110]



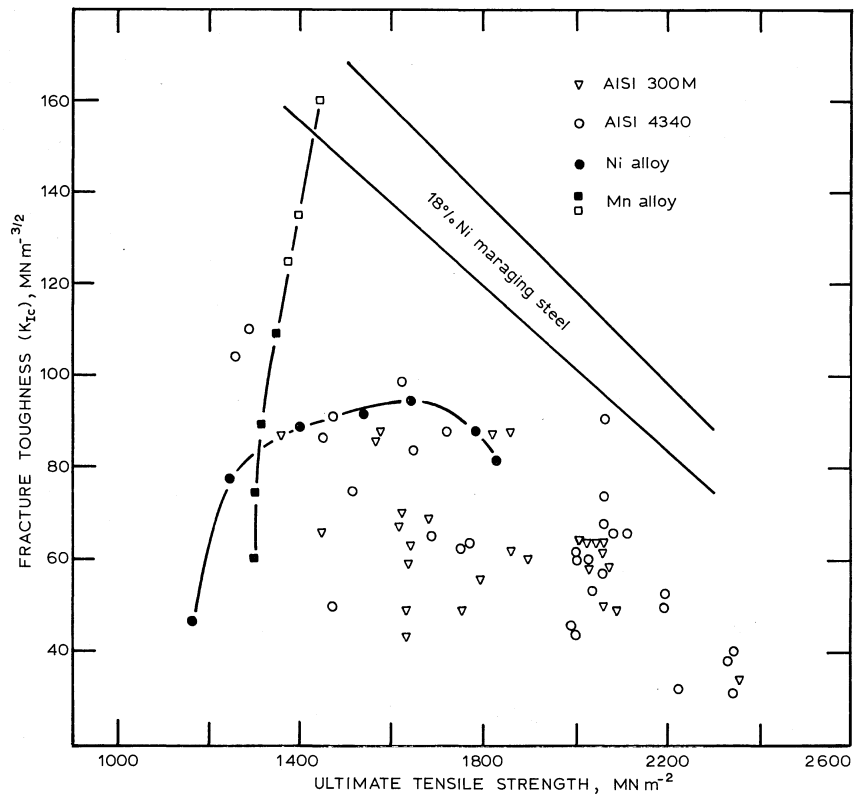


**Figure 17 Experimental data of fracture toughness versus ultimate tensile strength for Ni alloy and Mn alloy compared with some commercial steel grades [81]**

More than twenty years later beginning in 2002, Caballero, Garcia-Mateo and Bhadeshia conduct and develop studies on the second generation of the carbide free bainite with a 0.8-1.0wt% carbon content. [10, 92, 112, 113] The mechanical properties of this second generation of high-carbon, silicon-rich carbide free bainitic steel are further improved relative to their first generation counterparts, reaching 2.3 GPa in ultimate tensile strength and  $30\text{MPa m}^{1/2}$  in toughness. The isothermal bainite transformation temperature of this generation reaches as low as 125 degree Celsius, since the martensite start temperature

( $M_s$ ) decreases with an increase in the carbon content. The bainite that forms under greater undercooling gives finer ferrite plates with a thickness of 20-40nm as shown in Figure 18 below. Because bainite transformation time decreases with finer microstructure, it extends to a range of 8 hours to 25 days to achieve the maximum bainite volume fraction. [113] High strength is, thus, associated with fine scale microstructure. [10, 92] Lastly, both yield strength and ultimate tensile strength increase with lower transformation temperature, because the low temperature results in bainite of finer grain size. (Figure 19) [94]

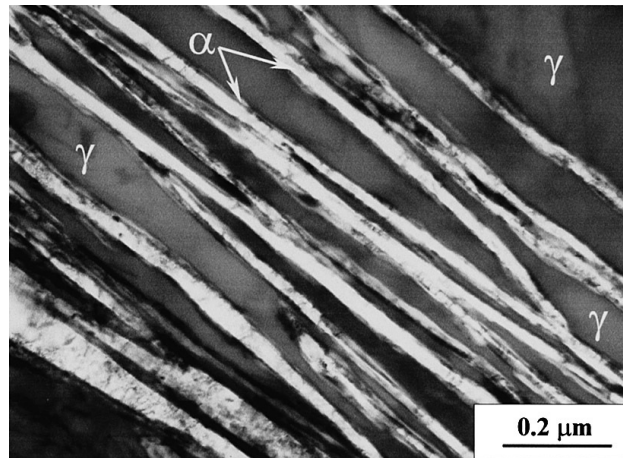
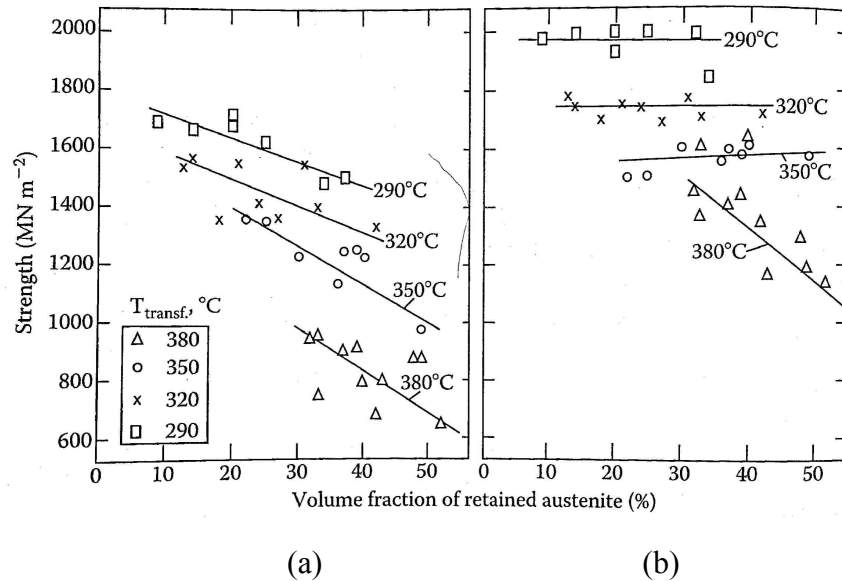


Figure 18 TEM micrograph of Fe-0.98C-1.46Si-1.89Mn-0.26Mo-1.26Cr-0.09V (wt%), transformed at 200 °C for 15

days. The dark phase represents the austenite whereas the white phase is the bainitic ferrite [113]



**Figure 19 Effect of volume fraction of retained austenite and bainite transformation temperature on (a) the yield strength and (b) the ultimate tensile strength of the carbide free bainitic steel [94]**

Since the aforementioned work on the second generation of the carbide free bainite, numerous studies examine the effects of alloy composition and heat treatment procedure on carbide free bainite transformation kinetics, its final microstructure and its mechanical behavior. Today, the carbon content in carbide free bainitic steel lingers around ~1 wt% for better weldability.

Recently, instead of focusing on isothermal heat treatment at the bainite transformation temperature range, a series of studies attend to carbide free bainitic steel formed by continuous cooling. [9, 114] In these experiments, researchers carefully control and monitor the cooling process. They note that after austenitization, the material is initially under accelerated cooling reaching 750 °C or 500 °C followed by air cooling approaching

room temperature. This simplified heating and cooling procedure is more practical in industry productions, despite the need for an additional alloying element, such as Mo and Cr, to reach maximum bainite volume fraction before cooling to room temperature. The ultimate tensile strength and fracture toughness of the carbide free bainitic steel are measured accordingly. The continuous cooling process yields a material with a comparable combination of strength and toughness in relation to the first generation of carbide free bainite. This is illustrated in Figure 20 in which the two large points correspond to experimental data after continuous cooling, whereas the smaller points represent the properties of the first generation of carbide free steel by isothermal bainite treatment. Both fracture toughness and ultimate tensile strength of carbide free bainitic steel are superior to quenched and tempered (QT) low alloy martensitic steel grades. Moreover, this combination matches the properties of maraging steel at a thirtieth of the cost, at most. [9]

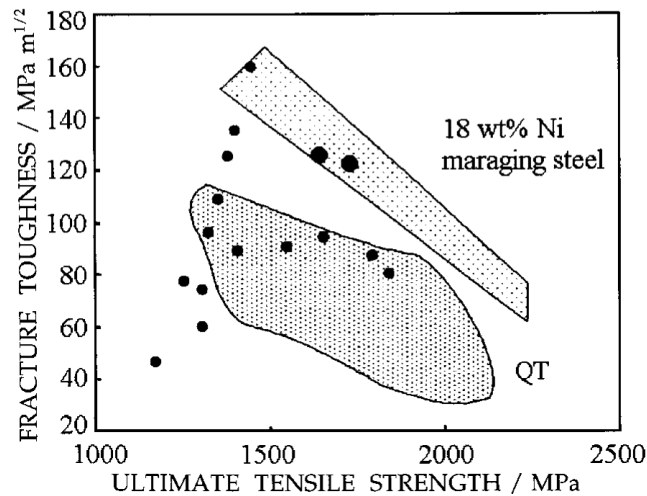


**Figure 20** The combination of fracture toughness and ultimate tensile strength of the carbide free bainitic steel versus those of quenched and tempered (QT) low alloy martensitic alloys and maraging steels [9]

Finally, Sugimoto's ongoing research on carbide free bainitic steel focuses on steel with 0.2wt% carbon content and much coarser microstructure due to its relatively high  $M_s$  temperature. The isothermal heat treatment procedure is designed at temperatures above and below the  $M_s$  temperature with holding time in the range between 10 to 10000 seconds. The steel grades have high stretch-flangeability, as well as acceptable tensile strength in the range of 800-1300 MPa. [115-119] Hell also isothermally heat treats the carbide free bainitic steel with 0.2-0.3wt% carbon at temperatures 50 degrees above and below the  $M_s$  temperature for 40-60 minutes. The optimum combination of strength and ductility (ultimate tensile strength: 1400MPa, uniform elongation: 14%) is obtained from the material with 0.3wt%C after bainite treatment at  $M_s+50^\circ\text{C}$ . [120]

One of the major advantages of the carbide free bainitic steel is its production method. It is relatively applicable in the industry since it only involves the conventional heat treatment process. The ultra-fine microstructure with both bainitic ferrite and retained austenite in the scale of nanometer can be achieved in conventional two-step isothermal heat treatment or continuous cooling after hot rolling. Contrariwise, other nanomaterial production techniques, including powder metallurgy technology, are limited by thermal stability, contamination and porosity. [121]

These previous works [7, 8, 80, 115, 122-124] on carbide free bainitic steel show its complicated microstructure and intriguing mechanical properties. To further understand the work hardening behavior of the carbide free bainitic steel, additional analytical studies are required. Specific and quantitative analysis need to be performed on the material to understand the features of the complex microstructure in greater detail. Hence, further studies are necessary to comprehend the relationship between the mechanical behavior and the microstructure features to optimize its performance.

## **1.4 Work hardening**

Carbide free bainitic steel exhibits extraordinary ductility (high uniform elongation) with great strength at the same time. It allows this type of strong steel grade to be cold-pressed into complex shapes, which is one of the most important in-use properties for the automobile industry. [125] The main purpose of this project is to study the

mechanical behavior of the carbide free bainitic steel and its correlation with its microstructure. There are some fundamental concepts and approaches related to the improvement of work hardening behavior of materials in general that need to be described first.

Crystalline solids become more resistant to deformation under plastic deformation itself. The behavior that the material hardens during deformation is called “work hardening”. Work hardening occurs while the plastic flow strength of the crystalline material increases due to various restricting dislocation motions. The interactions between dislocations and the microstructure influence the work hardening behavior of the material. The work hardening rate at the microscopic scale is the outcome from the dislocation dynamics, which is the balance between the creation and annihilation of dislocations. Dislocation itself is one of the main obstacles to dislocation movement that dominates the work hardening. Besides, dislocations form during plastic deformation. The increase in dislocation density leads to the decrease of inter-planar spacing between dislocations. The greater flow stress is required for the dislocations to break through obstacles with smaller inter-planar spacing, thus the greater strengthening performance of the material during deformation. Moreover, dislocations are mobile under deformation and can intersect each other to form immobile jogs. These jogs act as hard obstacles to dislocation mobility, and the possibility of jogs creation is also proportional to the overall

dislocation density. The flow stress  $\tau$  is shown in the Equation 3,

$$\tau = \tau_0 + \alpha G b (\rho)^{1/2} \quad \text{Equation 3}$$

where  $\tau_0$  is the intrinsic strength of a material and  $\rho$  is the dislocation density. [88]

The work hardening rate increases with more sources of dislocations and less recovery. A high work-hardening rate is essential for delaying the onset of necking leading to an excellent balance of strength and ductility. [88] “Necking” is defined by the Considere criterion:

$$\sigma_T = d\sigma_T/d\varepsilon_T \quad \text{Equation 4}$$

According to the Considere criterion (Equation 4), the necking point is determined by the intersection between the true stress-strain curve and the strain hardening rate ( $d\sigma_T/d\varepsilon_T$ ) curve as shown in Figure 21. A better combination of high tensile strength and ductility of the carbide free bainitic steel can be obtained by an upward shift of the strain hardening rate curve. By work hardening, the load-carrying capacity of the material increases with the increase in the strain of deformation. This gives a higher strain hardening rate leading to a better strength and ductility combination. [126] The strain hardening rate is also called the work hardening rate.



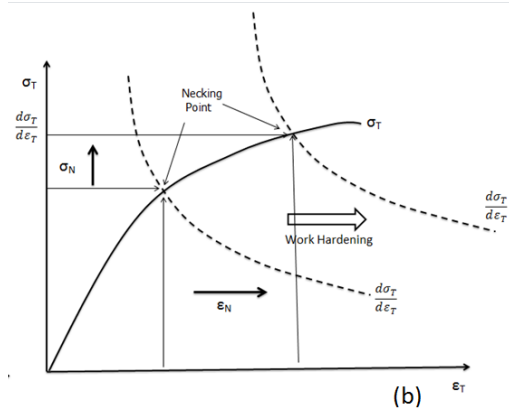


**Figure 21** Schematic illustration of the stress-strain curve and the strain hardening rate curve, both the strength and ductility are increased with upward shift of the strain hardening rate curve due to work hardening

### 1.4.1 Kocks-Mecking Model

The theory of work hardening had been studied over a century but still had not met an agreed upon conclusion, until the concept of “stage” in work hardening introduced as a milestone in the development of work hardening mechanisms in the 1950s. [127] Nonetheless, complete knowledge of the work hardening has not been achieved. A successful model has been developed to rationalize the macroscopic observations of work hardening as the Kocks-Mecking model. This model is based on well-established physical principles involving dislocation accumulation and dynamic recovery that simultaneously occur throughout the whole process of deformation. It separates the work hardening behavior of a single crystal or polycrystal material into four stages while one of the mechanisms may dominate a particular stage. [128]

#### **1.4.1.1 Stages I, II, III and IV for single crystal and polycrystalline material**

In Stage I (easy glide), the rate of work hardening depends solely on the orientation of the single crystal. The Stage I cannot be applied to the deformation of polycrystalline material where multiple slip takes place from the beginning. Stage II is correlated to the elasto-plastic transition period of the material showing the highest strain hardening rate. The grains and phases in the material with different yield strengths deform plastically under different stress levels. These differences in yield strength of each element in microstructure create the constraint strains to the adjacent neighbors and induce internal stresses. This elasto-plastic transition period is also called “gradual yielding” and can be studied by the Bauschinger effect and the Masing Model. The Stage II is mainly contributed by dislocation storage, which is an athermal hardening mechanism. Thus, the strain hardening rate at this stage is independent of the material and is insensitive to the temperature and the strain rate. The following Stage III starts when  $d\sigma/d\varepsilon$  approximately equals to  $E/50$  in polycrystal ( $E$  is the young’s modulus). The beginning of the Stage III means that all the elements in the material have yielded. The strain hardening rate is mostly observed to have a linear relationship with the true stress in both single crystal and polycrystal materials. Stage III is dominated by both dislocation storage and recovery. Hence, it strongly depends on the temperature and the strain rate.

The Voce law is mainly introduced to study the stage III and can determine the intercept on the true stress axis from the linear part in the middle of the Stage III. Stage IV may appear when the lower strain rate is achieved as referred to Figure 22. [128]

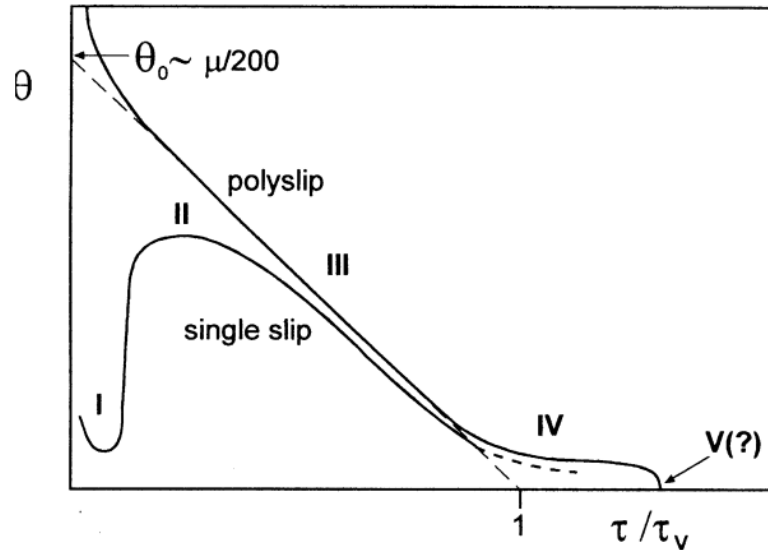


Figure 22 Schematic sketch of hardening rate versus flow stress illustrating the hardening stages for polycrystals in comparison to those for single crystals deformed in single slip [128]

## 1.4.2 Residual stress

### 1.4.2.1 Microscopic residual stress

For polycrystalline material, stresses may occur within each single grain when dislocations pileup near obstacles such as grain boundaries. Internal stresses may also vary from one grain to another. Since the orientation of each grain is different, it will cause grain-to-grain variations. For multiphase materials, each phase has different yield

strength, elastic modulus and thermal expansion coefficient. Under temperature change or plastic deformation, the internal stresses are induced due to the properties difference of each constituent in the microstructure. [89]

Under deformation, some grains or phases will deform at lower stress, due to the orientation of the grain or strength of the phase. During unloading, the grains that were under plastic deformation in tension will be left under residual compression. The grains that are still under elastic deformation will be under tension. [89] Residual stress also can be induced during phase transformation, including martensite and bainite, when these phases are transformed by shear or rapid lateral growth.

#### **1.4.2.2 Macroscopic residual stress**

Residual stresses may vary from center to the surface for one part after a bar is stretched plastically in tension and unloaded. The surface grains are less constrained by the neighboring grains compared to the interior grains under tensile deformation. After deformation, the grains in the surface of the bar will be under residual compression. During the heating procedure, the heating and cooling rate is different between the surface and the interior of a body causing volume expansion differences that induce residual stresses macroscopically. [89]

### **1.4.3 Isotropic work hardening**

Isotropic work hardening happens when the yield surface expands symmetrically during plastic flow. [129] Due to the preferred orientation or texture of each grain or phase, as well as difference in the shape or morphology of some phases or precipitations, the resistance to deformation is greater in some directions than the others. Hence, the assumption that the work hardening behavior is isotropic is rarely true, especially in the early stage of plastic deformation. The kinematic work hardening model is used to describe the anisotropic work hardening behavior of a material. [88, 89]

### **1.4.4 Kinematic work hardening**

Kinematic work hardening is related to the magnitude of internal stresses created within the deforming material opposing the applied stress. Kinematic work hardening is determined mainly by the amount of internal stresses due to the inhomogeneity of the microstructure. As the deformation strain increases, the internal stress increases as well, thus, more work is needed to offset it. The strain hardening rate increases with the increment of flow stress required at higher deformation strain level. [130] Microscopic inhomogeneity is crucial in order to understand the development of internal stresses in the material and the associated kinematic hardening. Studies had been done on the kinematic work hardening behavior of the dispersion strengthened alloys, where second

phase particles are introduced to the microstructure as hard, undeformable inclusions or isolated islands. [131] Kinematic work hardening is scale dependent. The finer the scale, the higher the internal stresses. The existence of unreleased internal stresses stored inside the material can be revealed by the Bauschinger test which is a set of uniaxial forward and reverse loading tests. The stress from the reverse load stress curve at a given strain is less than that stress at the same strain level under tension. [130] Kinematic work hardening is an additional component accompanying the isotropic hardening to strengthen the material further.

### **1.4.5 Masing Model**

When the material is under deformation, the plastic flow and the dislocation motion in each element in the microstructure is initiated by a different CRSS (critical resolved shear stress). The level of deformation of each element is different under applied stress leading to strain partitioning among the whole structure. For the carbide free bainitic steel, each bainitic ferrite lath and austenite thin film may have different yield strength not only due to the different crystallography structure, but also to the difference in carbon content and grain size. In other words, this steel grade is composed of nano-sized elements with a broad range of yield strength. [130] The Masing model describes this behavior that is also known as “composite effect”. [132]

This heterogeneous distribution of flow stress and strain partitioning generates internal

stresses in between elements in short and long range. The short range internal stress is correlated to the pileup of dislocation at the obstacles (such as grain boundaries). Under applied stress in tension, the internal local stress concentration increases with an increase in the dislocation density. This local storage stress is released when the loading system is reversed to compression. The yield strength is lowered under the reversed compression, since the dislocations can move more easily in the reverse direction. [133]

In the multiphase microstructure, some elements with lower yielding stress have been plastically deformed where other harder elements remain under elastic deformation. Thus, the long-term internal stress is due to the difference in the deformation stage of the element under a certain level of stress and strain. The constraining stresses applied by the neighboring elements with different deformation behavior cause directional internal stresses in between. [130]

### **1.4.6 Bauschinger effect**

The Bauschinger effect is usually measured from a set of uniaxial forward and reverse loading tests. The flow stress from the reverse load stress curve at a given strain is less than the stress from the forward stress curve at the same strain. [130] There are several causes of this effect. It is mainly because of the internal stresses induced during deformation in the forward tensile direction. The internal stresses are induced both inside the grains due to dislocations pile-up, in between the grains due to different

orientations, and in different phases with different yield strengths. The deformation in the opposite direction (compression) releases the internal stresses from pre-straining in tension leading to a reduction in the yield stress. Kinematic work hardening can also explain the difference between the yield strength in compression and that in tension, as a shift in the yield locus. Bauschinger test can estimate both the short and long term internal stresses in terms of “back stress”. [89]

### **1.4.7 TRIP effect**

It is challenging to quantify and determine the role of each phase on the work hardening behavior in a complex microstructure. Moreover, the scenario is even more complicated if the second phase is a transformable one. In the case of carbide free bainitic steel, the films of retained austenite, that act as the second dispersed phase, may transform to martensite under temperature cooling, applied stress or strain.

Additionally, austenite may transform to martensite due to its mechanical or thermal instability. Under deformation, unstable austenite may shear to form hard martensite, causing transformation induced plasticity (TRIP effect). Before discussing the possible roles that retained austenite may play on work hardening, it is necessary to provide a brief overview of the thermal and mechanical behavior of the retained austenite in general.

The stability of retained austenite depends on both the carbon content in the austenite and the morphology of this phase in the microstructure. In the case of carbide free bainitic



steel, carbide suppressing alloying elements (silicon and aluminum) are introduced to prohibit carbide formation. Interstitial carbon atoms are dissipated from the bainitic ferrite laths to the adjacent austenite matrix, instead of precipitating to form carbide. As a result, the stability of austenite is enhanced due to its carbon enrichment and a significant amount of austenite remains untransformed at room temperature in carbide free bainitic steel. The martensite transition is suppressed from the carbon-rich retained austenite. The retained austenite can be blocky or granular, and is surrounded by packets of bainite or bainite sheaves with various crystallographic variants. On the other hand, the carbon enriched austenite can be in film shape, dispersed between single bainitic ferrite lathes within each packet as shown in Fig 12. The carbon content of blocky austenite is significantly lower than that of thin austenite films as suggested in the Figure 23 below. [116]

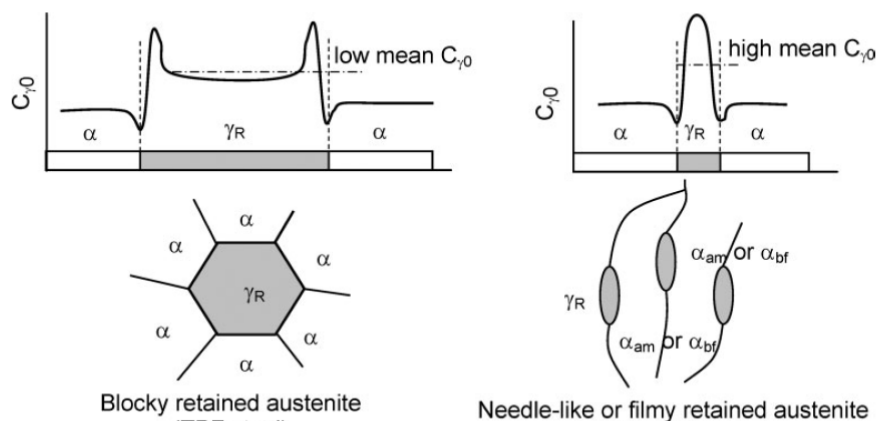


Figure 23 Illustration of concentration distribution in blocky and filmy retained austenite [16]

Due to the carbon content difference in these two forms of retained austenite, the stability

of blocky retained austenite is relatively lower, both thermally and mechanically, than that of the austenite in the thin film shape. Since martensite as the brittle phase is detrimental to ductility and fracture toughness, the presence of martensite instead of retained austenite is not favorable. Thus, the blocky retained austenite is not preferred due to its higher tendency to transfer to martensite during quenching to room temperature or at the initial stage of deformation compared to thin austenite film. [1]

On the contrary, the austenite film with relatively high stability is retained at room temperature and the martensite transition can be induced by applied stress or strain during deformation, causing the TRIP effect. The TRIP effect improves the ductility as well as the fracture toughness of the carbide free bainitic steel. The martensite transformation during work hardening is accompanied by shape changes, causing relaxation of the local stress and strain. Thus, the onset of necking is postponed. The retained austenite (softer phase) that progressively transform to martensite (harder phase) during the deformation (TRIP effect) improves the ductility of the material. [10, 92] The fracture toughness is related to the void initiation and crack propagation. The induction of martensite transition releases concentrated local stress especially at the matrix/inclusion or matrix/second-phase interfaces to prohibit or delay the void initiation. The TRIP effect occurring in front of a crack can release the stress at the tip of the crack to blunt its further propagation. [88] In conclusion, TRIP effect is beneficial to ductility and

toughness by postponing the onset of necking and suppressing the void initiation and the crack growth.

### **1.4.8 Strain aging**

Dislocations and interstitial atoms are attracted to each other. Each interstitial atom, such as carbon, is surrounded by a strain field in the lattice structure due to its size difference from the matrix. Carbon atoms tend to move toward and bind with the strain fields of dislocations to reduce the overall strain energy. [134]

At room temperature or elevated temperature, the carbon atoms diffuse to dislocations and pin the dislocations. Because the carbon atom and the dislocation are mutually attracted to each other, the movement of dislocations tends to be restrained by the much less mobile locking atoms. Thus, the mobility of the dislocations is affected, further strengthening the material. This effect is called “strain aging” and is dependent on temperature and time. Extra stress and energy are required for dislocations to break free from the pinning interstitial carbon atoms, in order to trigger slipping. [108] As a result, the yield strength is improved by the strain aging effect. [82] The stress-strain curve of materials after static strain aging is characterized by the Luder’s band. Under uniaxial tensile deformation, there is a localized transition region from elastic to plastic behavior. The Luder’s band appears when the load of yielding drops from its upper value and starts to fluctuate about an approximately constant value until the whole gauge section is

yielded. [135]

## **1.5 Fracture Behavior**

The toughness of a material is its resistance to crack propagation and its ability to absorb energy during deformation. The fracture toughness of the carbide free bainitic steel is extraordinary and is only comparable to Maraging steel, which is 10-100 times more expensive. [10]

The high fracture strength for a material is not only due to the work hardening to postpone necking, but also due to some factors to delay the void nucleation or blunt the crack propagation during deformation. The retained austenite and the nano-scale of the microstructure may have some contribution to the toughening behavior of the carbide free bainitic steel. The toughness is related to the work accompanying crack propagation. The crack propagation is associated with the stress concentration in the area in front of the crack tips known as the plastic zone as shown in Figure 24. The lower the stress at the plastic zone the more energy is needed for the crack to propagate. [88]

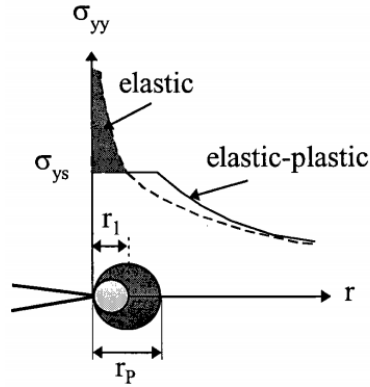


Figure 24 Schematic illustration of the plastic zone in front of the crack tip [136]

The carbide free bainitic steel may have brittle or ductile fracture behavior depending on various microstructural factors. Since the controlling factors to the brittle and ductile fracture are distinct, they will be discussed separately.

### 1.5.1 Brittle Fracture

The brittle fracture may take place by crack propagation within grains (transgranular fracture) or along the grain boundaries (intergranular fracture). Under tensile test, there is subtle or no visible evidence of any necking before the brittle specimen is fractured. The Griffith-Irwin criterion (Equation 5) is an effective way to describe the brittle fracture behavior, where the fracture stress  $\sigma_f$  is controlled by the crack size  $a$ . [126]

$$\sigma_f = \sqrt{\frac{EG}{\pi a}}$$

Equation 5

### 1.5.1.1 Transgranular Fracture

The transgranular fracture is also called cleavage. The crack propagation is dominated by repeated cleavage cracks through the grain in front of the crack tip as illustrated in Figure 25 below. This suggests that the cleavage fracture is related to the yield strength and the size of the grain at the crack tip. The energy associated with intergranular crack propagation is different from that of transgranular crack propagation. For transgranular fracture, the toughness is dominated by the surface energy  $\gamma$  of the crack and the fracture stress is equal to  $2\gamma$ . [88]

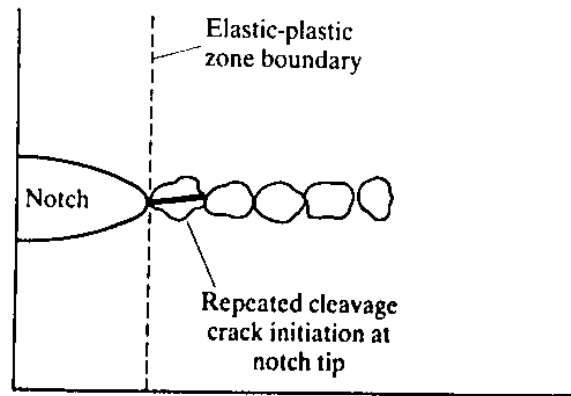
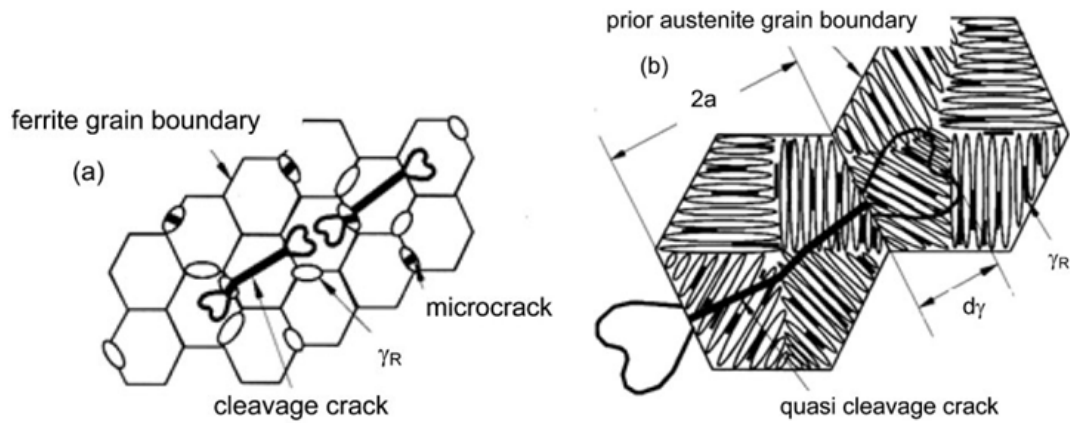


Figure 25 Schematic illustration of the repeated initiation cleavage cracks throughout grains at the crack tip [88]

The nano-sized retained austenite films and bainitic ferrite laths in the carbide free bainitic steel may effectively suppress the crack propagation. Instead of cracking through one big grain size with no interfaces at the plastic zone in the dual phase steel, extra energy is needed to break the atomic bonds near the grain boundaries in the plastic zone. Consequently, grain refinement in the microstructure may lead to the transition of

the fracture mechanism from the cleavage to quasi-cleavage crack. Therefore, carbide free bainitic steel can achieve considerably greater fracture toughness compared to the traditional dual phase or TRIP steel. This is due to the scale difference, as shown in Figure 26. [14]



**Figure 26** Schematic illustration of (a) cleavage crack in traditional dual phase or TRIP steel, (b) quasi-cleavage crack in carbide free bainitic steel [14]

### 1.5.1.2 Intergranular Fracture

For intergranular fracture, crack is propagating along the grain boundaries. Grain boundaries are the regions with many defects and dislocations due to their atomic mismatch and disarray, as compared to the atomic arrangement inside each grain. These boundaries are an easy path for diffusion of impurities, including both interstitial and substitutional atoms. Therefore, they act as a preferred region for segregation of impurities, as well as a preferential site for phase nucleation, and/or absorption of

elements from the environment. This segregation of impurities at grain boundaries is a potential mechanism for weakening or embrittlement of the material. The environmental embrittlement that weakens the grain boundaries includes hydrogen, liquid-metal and solid-metal embrittlement. The embrittling elements are segregated at grain boundaries since their diffusion is relatively rapid there compared to along the interior of each individual grain. Hence, the failure of the material may occur along grain boundaries to cause the intergranular fracture mechanism.

In the case of brittle intergranular fracture, the toughness is not only related to the surface energy but also the grain boundary energy  $\gamma_{gb}$ . The fracture work is equal to  $2\gamma - \gamma_{gb}$  instead. If the grain boundary energy is high enough due to its incompatibility, the crack may preferentially propagate along the grain boundaries. In this case, the crack size  $a$  in the Equation 5 above can be replaced by grain size. Thus, by refining the grain size, the critical stress to cause fracture increases. [88]

The fracture area associated with the intergranular crack propagation is greater than that for transgranular fracture. If the grain boundary energy cannot be high enough to compensate the higher fracture area of the intergranular fracture, the transgranular fracture will be preferred for its lower energy requirement.

### **1.5.2 Ductile Fracture**

A ductile fracture occurs if the microstructure is occupied mainly by ferrite phase with



less yield strength than martensite. Thus, the crack propagation is increasingly blunted. Instead of directly breaking the atomic bond at the plastic zone, void coalescence becomes the dominant factor affecting the ductile fracture. [88]

Voids nucleate at the boundary between the elastic and plastic zones under deformation due to plastic strain incompatibility. Hence, the microcracks or voids are often related to the second phase or particles with different yield strength. Moreover, if the second phase is very brittle, microcracks will form inside the grains. Crack propagation involves link-up of the microcracks at the interphase boundaries or inside the second phase grains. The microcracks or voids subsequently grow and coalesce during plastic deformation. The void link-up causes the failure of the material after necking due to plastic shearing. [88]

#### **1.5.2.1 Retained Austenite Toughening**

The retained austenite with TRIP effect that has been described in the previous section also has impressive fracture resistance behavior. During crack propagation, the retained austenite in the plastic zone near the crack tip can be induced to transform to martensite due to the high concentration of stress. The additional toughness can be attributed to the TRIP effect that requires extra energy to cause material failure associated with the work of martensitic transformation. [88]

### **1.5.3 Microscopic features of fracture**

The examination of the fracture surface on the failed specimens in microscopic scale is crucial to understand the causes of fracture. The appearance of the fracture in micro-scale of each fracture mechanism is distinctive. The SEM fractography provides a reliable and practical means to identify and reveal the causes of fracture by examining the characteristics of those three different fracture paths.

#### **1.5.3.1 Ductile fracture**

The fibrous appearance of the fracture surface is an indication of the microvoid link-up and coalescence. Those small voids nucleate at the necking region under high stress in the tension test. These microvoids form and grow at the stage between necking and fracture in the material, leaving “dimples” represented as concave depressions on the fracture surface (Figure 27). Since the microvoids are oriented and grow along the deformation direction, dimples form in a round shape on the fracture surface after uniaxial tensile deformation. Moreover, the depth of the dimple is correlated with the ductility of the failed material. [137]



**Figure 27** Section through the neck area of a tensile specimen of copper showing cavities and crack formed at the center of the specimen as the result of void coalescence. [138]

### **1.5.3.2 Transgranular brittle fracture (cleavage)**

Cleavage occurs, as a brittle low-energy fracture process, along low-index crystallographic planes with the maximum normal stress of each grain in the polycrystalline material. Thus, the fracture surface of a cleavage is commonly shown in bright color at low magnification by SEM with some features including feather markings (Figure 28) and river patterns (Figure 29). These patterns are due to the imperfections in the microstructure, such as grain boundaries, inclusions and dislocations. [139-141]

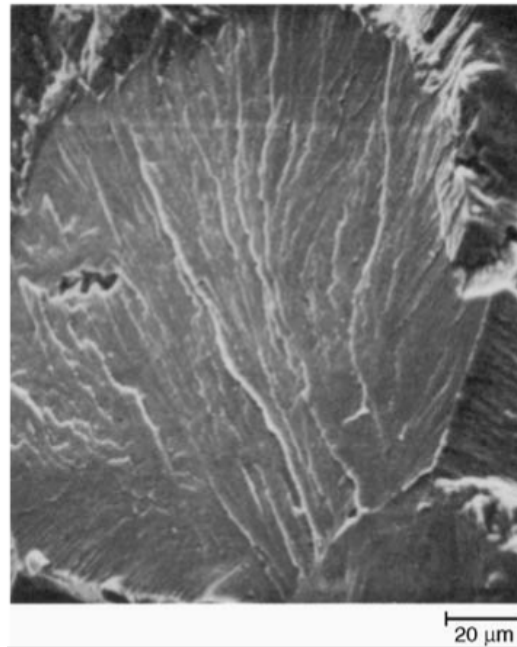


**Figure 28 Feather pattern on a single grain of a chromium steel weld metal that failed by cleavage [135]**

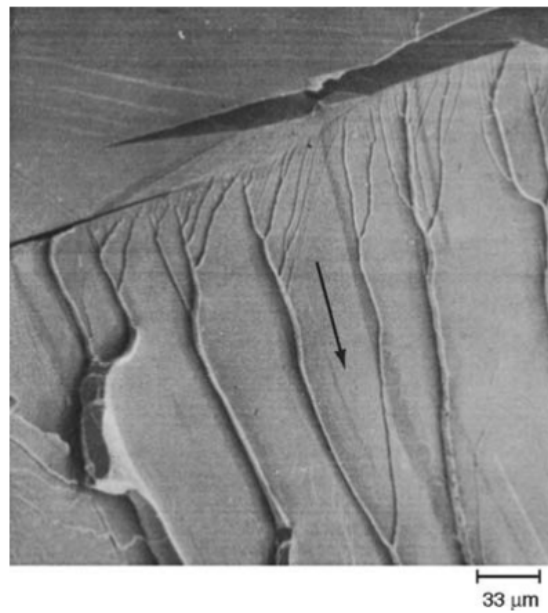


**Figure 29 Fracture surface from a ferritic steel failed by cleavage showing a sharply defined river pattern with arrow indicating the crack propagation direction. [142]**

### **1.5.3.3 Quasi-Cleavage fracture**

The presence of perfect cleavage fracture behavior is rare in metals since it requires some well-defined conditions. Instead, in most cases, the transgranular brittle (cleavage) fracture is accompanied by the microvoid coalescence. This process is called “quasi-cleavage” with the fracture surface of a mixture of cleavage facets and some patches of dimples as the evidence of plastic deformation by slip. [143]

### **1.5.3.4 Intergranular brittle fracture**

The grain boundaries are presented in polycrystalline materials and may be embrittled by fine brittle phases or segregation of impurities at the interface region. The common causes of intergranular failure include precipitation, impurity segregation, and environmental embrittlement at the grain boundary. The SEM fractography identifies the path of the intergranular fracture as facets with relatively visible cracks or a “clean” fracture surface along the grain boundaries (Figure 30). [135]

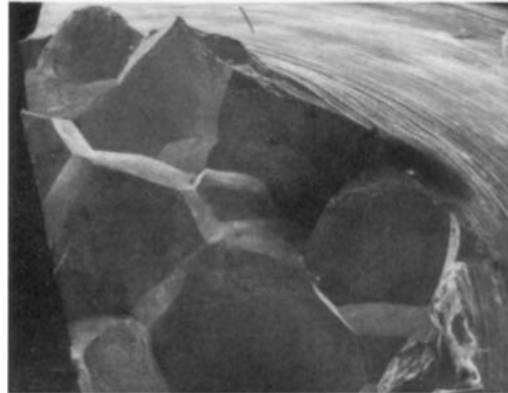


**Figure 30 SEM fractography of the fracture surface of a high-purity, coarse-grained Al-4.2Cu alloy with intergranular facets at low magnification (10x) [144]**

## **1.6 Ausforming**

Numerous studies have examined the effect of alloy composition and heat treatment on bainite precipitation kinetics in the carbide free bainitic steel. Nonetheless, the effect of prior deformation on the kinetics of the bainite transformation and influence on the final microstructure of carbide free baitine has received considerably less attention. One of the main focuses of this project is the impact of ausforming (plastic deformation of austenite) on the microstructure and mechanical properties of CFB steels. Ausforming has been shown to affect the bainite transformation kinetics, as well as the crystallography and the final volume fraction of bainitic ferrite and retained austenite. Hence, ausforming process changes its mechanical behavior from the conventional carbide free bainitic steel.

### **1.6.1 Definition**

The term “ausforming” represents the thermo-mechanical process that involves deformation of austenite before it decomposes to ferrite, pearlite, bainite or martensite at an elevated temperature range. This ausforming treatment was first used to introduce more defects to the parent austenite phase in order to improve the strength of the final steel product. [145] This thermo-mechanical treatment involves application of heat and a deformation process simultaneously. It can be performed on a specimen with systematic control of the temperature gradient and level of deformation by Gleeble or deformational dilatometer laboratory.

### **1.6.2 Bainite transformation kinetics change**

The response of bainite transformation kinetics to the ausforming is a complicated and controversial topic. The transformation kinetics of bainite can either be promoted or retarded by ausforming depending on the deformation temperature and the strain level. Similar to the well-observed fact that deformation of austenite at elevated temperatures accelerates the transformation from austenite to ferrite and pearlite, the reaction kinetics of bainite are found to be promoted by ausforming initially. This acceleration of bainite transformation could be explained by the introduction of more heterogenous nucleation sites of bainite to the microstructure by deformation of the parent phase. [99, 146-149] On

the other hand, investigations by other groups proposed that the bainite growth is hindered by the ausforming due to the presence of dislocation debris. Consequently, the overall bainite transformation kinetics is retarded, and the final bainite volume fraction is reduced. [150-155] Further studies are needed to study this controversial topic by relating the bainite transformation kinetics with the deformation strain and temperature.



## **2 Materials and experimental methods**

### **2.1 Preparation of materials**

All experiments were performed on a high-purity quaternary alloy containing 0.4%C, 2.8%Mn and 1.8%Si (mass%). The alloy was prepared by induction melting (40kg) followed by hot forging in order to break down the as-cast microstructure. In order to facilitate subsequent machining, the material was tempered for 16 hrs at 923K(650° C). Flat tensile specimens with a gauge length of 15 mm and a cross section of 3 mm x 3 mm and round tensile specimens with a gauge length of 15mm and a cross section with 3mm in diameter were machined.

### **2.2 Heat treatment procedure**

#### **2.2.1 Bainite treatment - two step isothermal heat treatment**

The tensile specimens were austenitized for either 10 minutes at 1133K(860°C) or 15 minutes at 1093K(820°C) under Argon atmosphere in order to minimize decarburization. In both cases, the austenite grain size was 30 +/- 5  $\mu\text{m}$ . Following the austenitization treatment, the samples were transferred to a salt bath held at 573K(300°C) for times of 30, 60, 90 and 120 minutes, and oil quenched to room temperature in the end of the heat treatment (Figure 31).

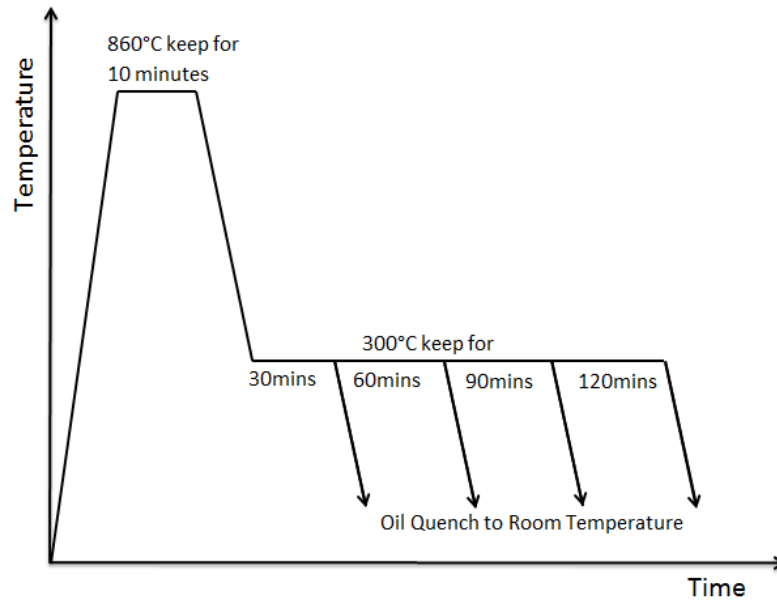


**Figure 31 Heat treatment process**

### **2.2.2 Homogenization heat treatment**

The homogenization procedure is performed to eliminate banding structure due to manganese segregation. Tensile specimens are heated at 1273K (1000°C) for 72 hours at argon atmosphere and then air cooled to room temperature, to evaluate the effect of banding on mechanical properties

### **2.2.3 Prior austenite size modification heat treatment**

Two methods are done to modify the prior austenite grain size: first, the grain size can be refined by a number of thermal cycling processes between the austenitizing temperature and room temperature (Figure 32). Second, the grain size can be increased by prolonged

austenitizing time at 860°C for 90 minutes as shown in Figure 33.

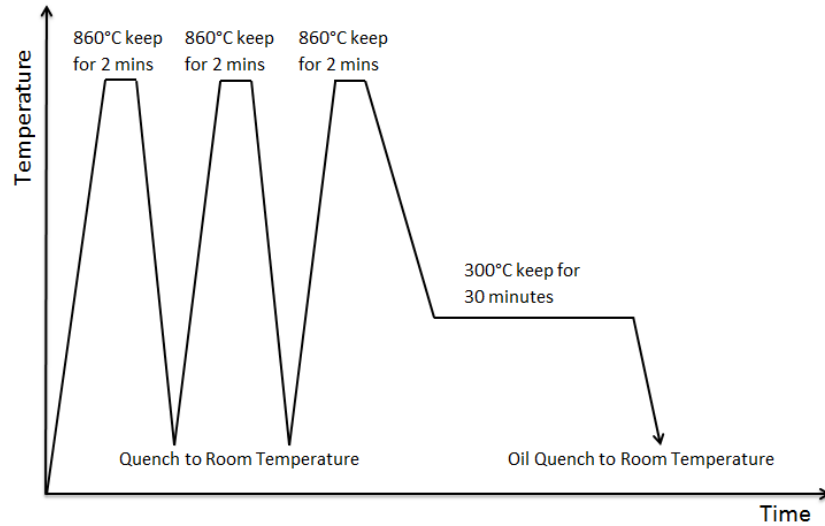


**Figure 32 Prior austenite grain refinement by thermal cycling**

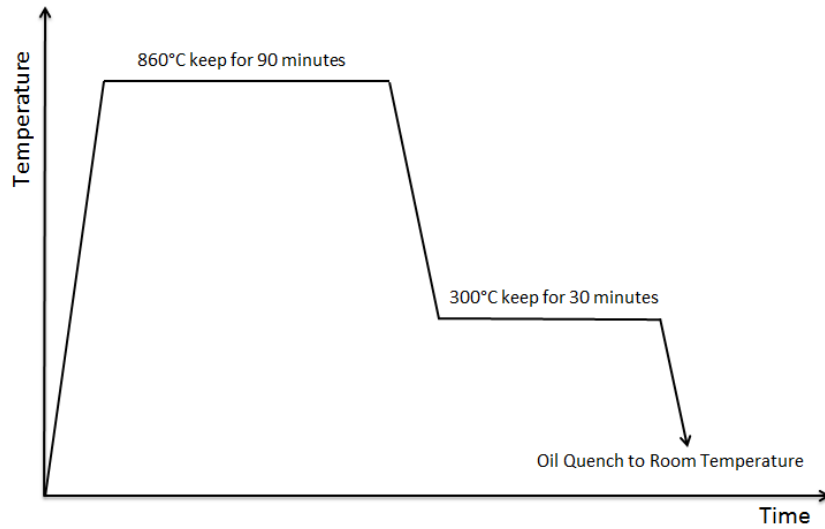


**Figure 33 Prolonged austenitization for higher grain size of prior austenite**

The prior austenite grain size is refined to 12  $\mu\text{m}$  after thermal cycling, and the size is changed to 50  $\mu\text{m}$  after 90 minutes austenitization.

## **2.2.4 Ausforming – thermo-mechanical treatment**

Ausforming is a thermo-mechanical treatment that plastically deforms the austenite phase after austenitization. Two methods are applied to mechanically deform the specimen before the bainite transformation during the incubation period.

### **2.2.4.1 Hot rolling**

Rectangular specimens with a dimension of 10x1x1cm are heated at 1133K(860°C) for 15 minutes, followed by air cooling and rolling to 13% deformation at 623K(350°C). The specimen is then transferred to a 573K(300°C) furnace held for 90mins and water quenched(WQ) to room temperature. A thermometer is attached to the center of the specimen to monitor the temperature change during the thermo-mechanical treatment.

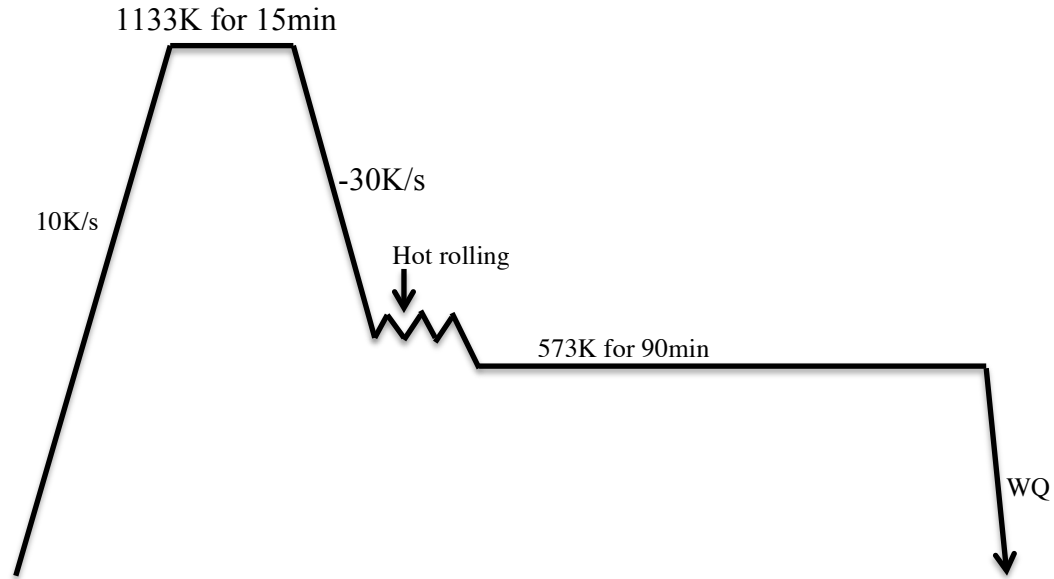


Figure 34 Ausforming experiment procedure with hot rolling

#### 2.2.4.2 Gleeble

The flat tensile sample with gauge length of 15mm and cross-section of 2x2mm is first heated at 1133K(860°C) for 15 min for fully austenitization then cooled to 573K(300°C) at 10 °C s<sup>-1</sup> cooling rate. Deformation (in tension) of 10% and 20% elongation with strain rate of 10mm/min is performed at 573K(300°C) followed by isothermal heat treatment at 573K(300°C) for 2 different holding time (30 and 60 minutes) before oil quench to room temperature. The stress is released after deformation.

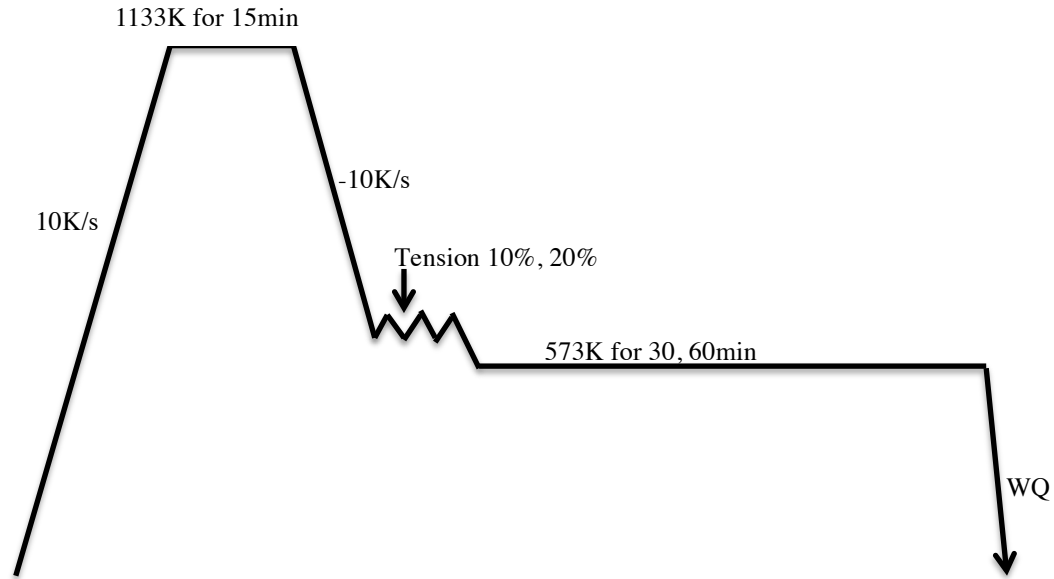


Figure 35 Ausforming experiment procedure with Gleeble

## 2.3 Characterization of Microstructures

In order to obtain a complete description of the microstructure evolution, the material was characterized over a wide range of length scales; the samples were examined using Optical Microscopy, Scanning Electron Microscopy (SEM), Transmission Electron Microscopy (TEM), Electron Backscatter Diffraction (EBSD) and X-ray Diffraction (XRD).

### 2.3.1 Optical Microscopy

The samples for optical metallography were mechanically polished. The Bakelite is

used in a hydropneumatic mounting press. SiC abrasive paper is used for grinding from coarse to fine with the grit sequence 320-500-800-1000-1200. The sample preparation is finalized by polishing with 15, 3 and 1 $\mu$ m diamond plate. There are two etching methods used to distinguish bainitic ferrite from the martensite. The first method is using 2% Nital for 15 seconds. This method darkens the bainitic ferrite laths, and the martensite phase is in lighter grey colour. The second etching method is by a solution of 40g NaOH, 60g H<sub>2</sub>O and 15g NaNO<sub>3</sub>, which is developed by ArcelorMittal. The second etching procedure consisted of immersion in the above solution for 60 seconds at 373K(100°C) and can separate the bainitic ferrite (white) from martensite (darker brown). Optical observations were carried out on the NIS-Elements BR 3.0 Imaging System on a Nikon Eclipse LV100 Microscope.

### **2.3.2 Scanning Electron Microscopy (SEM)**

The fracture surfaces of tensile specimens were examined using Philip 515 SEM operated at 15 keV. For the microstructure analysis, the samples are prepared by mechanical polishing down to 1 $\mu$ m and then slightly etched by Nital 2% solution for 20 seconds. The specimens are observed at the center of the cross-section using the Philip 515 SEM operated at 15 keV with a working distance of 10mm

### **2.3.3 Transmission Electron Microscopy (TEM)**

Thin foils for the transmission electron microscopy (TEM) were prepared by grinding the specimens to a thickness of 0.1 mm and mechanically punching 3 mm discs from the resulting wafers. The discs were electro-polished using a solution of 10% perchloric acid in methanol. The thin foils were examined using a conventional transmission electron microscope, PHILIPS CM-12, operated at 120 keV.

### **2.3.4 Electron Backscatter Diffraction (EBSD)**

The samples for EBSD analysis were prepared using standard metallographic methods followed by polishing with 9 $\mu$ m, 3 $\mu$ m and 1 $\mu$ m diamond suspensions and 0.05 $\mu$ m neutral Alumina suspension (OP-AN). Electron Backscatter Diffraction (EBSD) observations were performed on the as-polished material using JEOL JSM-7000F FEG-SEM equipped with a CCD detector for EBSD analysis. An acceleration voltage of 20 keV and a working distance of 18.4 mm were used for the examination of sample microstructural development. The sample was tilted 70° for the collection of data. Analysis of the EBSD results was performed using the HKL channel 5 software package. The orientation mapping by EBSD was conducted at a step size of 50 or 100 nm.



### **2.3.5 X-ray Diffraction (XRD)**

The effect of deformation on the stability of retained austenite was investigated by X-ray diffraction on a series of cold-rolled specimens with equivalent von Mises strains between 0 and 1.0. The measurements were performed using a Proto LXR D machine equipped with a 512-channel detector spread over an arc of  $2\Theta = 18.7^\circ$ . Chromium  $K_{\alpha 1}$  radiation was used in all cases, and the exposure time was 50 s for each peak analyzed. To calculate the volume fractions of each phase, the intensities of the  $(2\ 0\ 0)_\gamma$ , and  $(1\ 0\ 0)_\alpha$  peaks were integrated and the volume fractions computed via ASTM E975-03 [29].

## **2.4 Characterization of mechanical behavior**

### **2.4.1 Hardness test**

The hardness of specimens are investigated by Vickers microhardness test under a 200g load.

### **2.4.2 Tensile test**

The tensile tests were performed using an Instron 810 testing frame with a maximum tensile load of 100 kN. The specimens were pulled to fracture at a constant cross-head speed of 1 mm/min.

### 2.4.3 Bauschinger test

The Bauschinger tests were also performed by Instron 810 with a maximum tensile load of 100 kN at a constant cross-head speed of 1 mm/min. These tests consisted of pre-staining the specimens in tension to various levels followed by reverse loading in order to compare the yield stress in tension and compression as a function of the pre-strain.

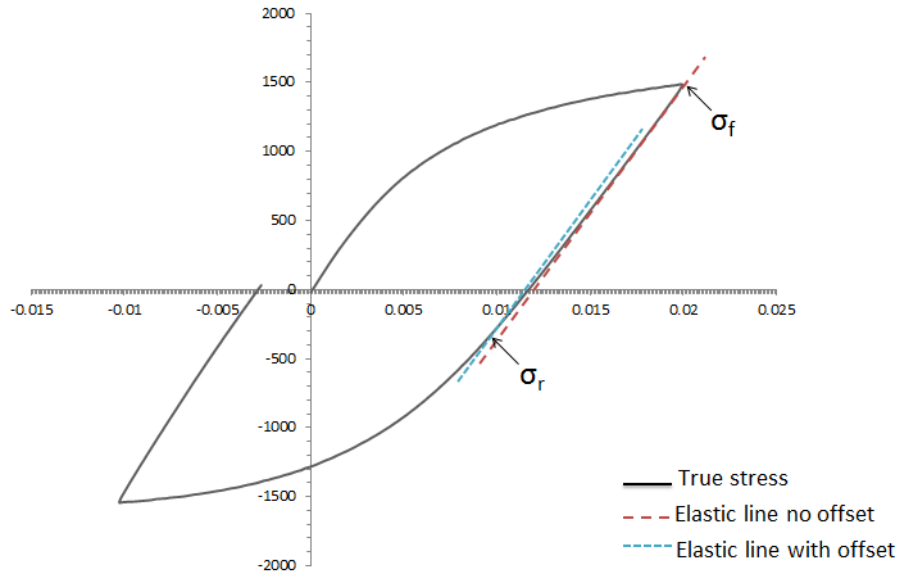


Figure 36 Bauschinger Test and offset method

$$\sigma_B = (\sigma_F - \sigma_R)/2$$

Equation 6

### **3 Bainite treatment at 300°C for different times**

Numerous prior studies on carbide-free bainitic steels have focused on alloy and process design. By varying the chemistry, transformation time and temperature, certain levels of strength and ductility can be achieved. Considerably less attention has been paid to the development of physically-based models that incorporate the mechanisms responsible for the high work-hardening rates and high fracture toughness of these steels. The development of a physically-based model for the deformation behavior of carbide-free bainite is challenging because it involves a number of length-scales. At the macroscopic scale, one is concerned with banding due to Mn segregation during solidifications and its influences on the distribution of bainite and martensite in the final microstructure. At the mesoscopic scale, it is essential to capture effects related to the volume fractions of bainitic ferrite, retained austenite and martensite as a function of the transformation time. In addition, it is necessary to understand the stability of retained austenite at the microscopic scale and the contribution of the TRIP effect to the strengthening of the material.

In this contribution, we have attempted to examine the effect of the various microstructural length scales on the deformation behavior of carbide-free bainitic steels. To that end, the behavior of banded steels was compared to that of steels that have been

homogenized to eliminate the banding structure. The effect of the martensite volume fraction remaining within the microstructure was examined by varying the isothermal bainitic transformation time. In addition, co-deformation of bainitic ferrite and retained austenite was examined using monotonic tensile tests and strain-reversal tests. Particular emphasis was placed on understanding the effect of the various microstructural length-scales on the work-hardening behavior (isotropic and kinematic) and the operating damage and fracture processes. Moreover, the inconsistency of mechanical performance of this steel grade has been studied by considering its strain aging response. Furthermore, the correlation between fracture behavior and the prior austenite grain boundary has been analyzed.

## **3.1 Bainite transformation kinetics**

### **3.1.1 CCT diagram**

The CCT diagram (Figure 37) was measured by our cooperating group from China using a dilatometer. [156] It shows that the bainite transformation will occur approximately between 200°C and 400°C after cooling from the austenitizing temperature with cooling rates ranging from 20°C/s to 0.5°C/s.

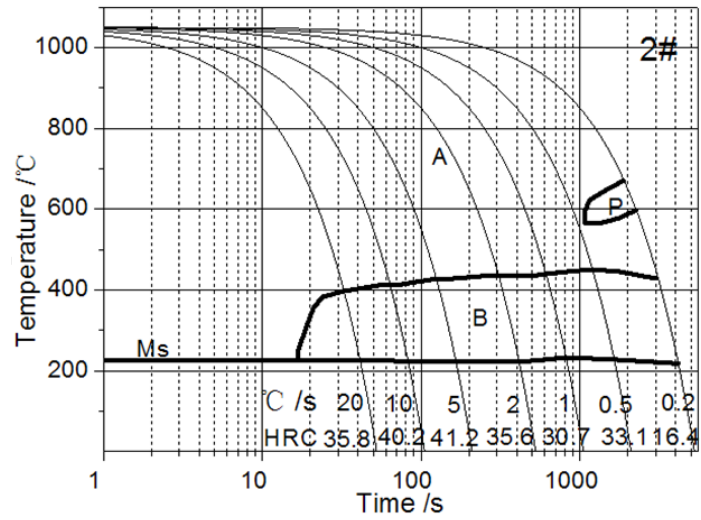


Figure 37 CCT diagram of the steel with 0.4C-2.8Mn-1.8Si (wt%) chemical composition [156]

### 3.1.2 TTT diagram

The volume fraction of bainite increases with the increment of the holding time for isothermal heat treatment at the bainite transformation temperature range, as shown in the TTT diagram below [157].

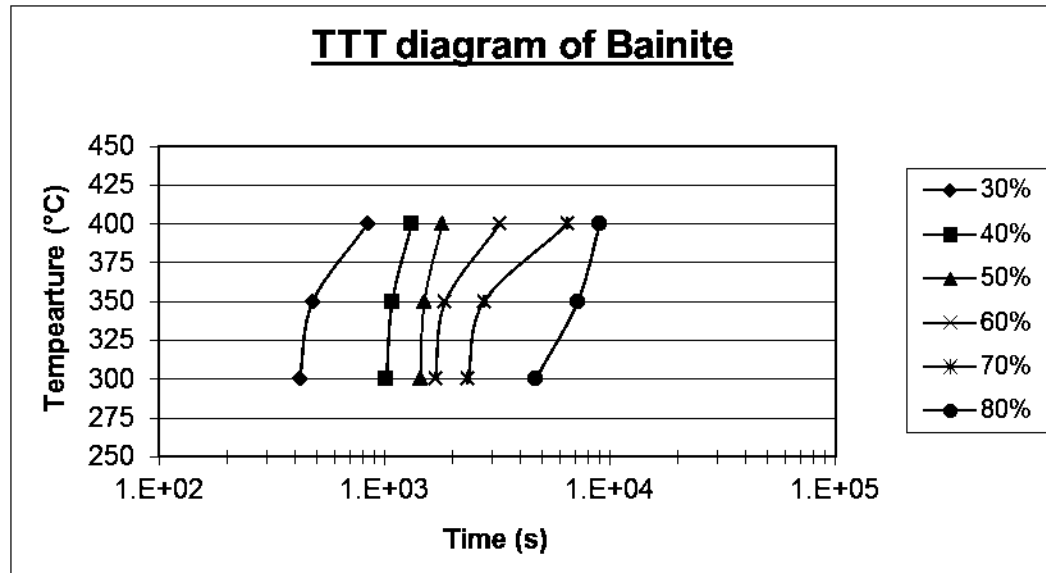
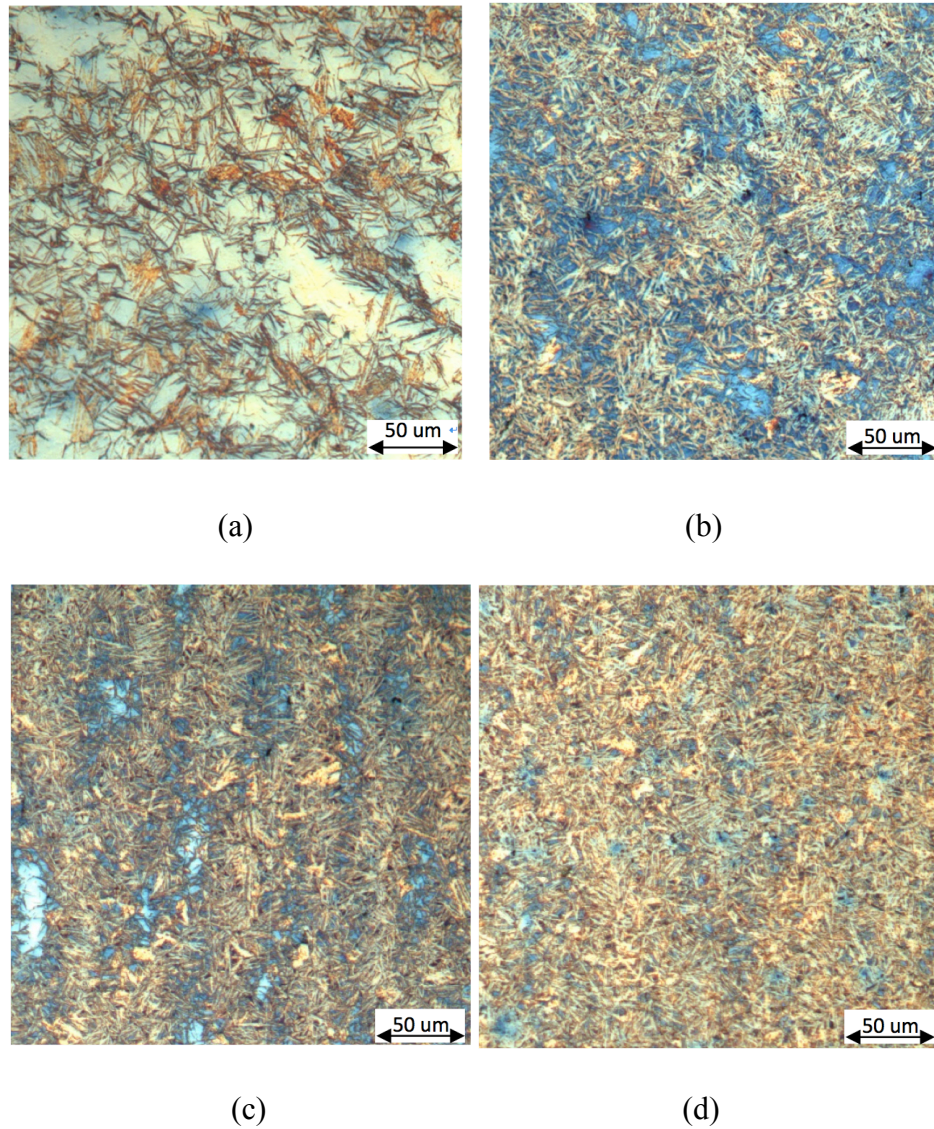


Figure 38 TTT diagram of the steel with 0.4C-2.8Mn-1.8Si (wt%) chemical composition [157]

## 3.2 Microstructures

### 3.2.1 Main phases

The microstructure evolution as a function of the heat treatment time is shown in Figure 39. The needle-like microstructure of bainite (bright phase) is clearly distinguishable from the martensitic matrix (blue phase). As the holding time at 300°C increases, the volume fraction of bainite structure increases, but the grain sizes of bainitic ferrite and retained austenite remain the same.



**Figure 39 Microstructure of the banded specimens isothermally transformed at 573K(300°C) for (a) 30, (b) 60, (c) 90 and (d) 120 minutes.**

Precise quantification of the volume fractions of the various phases by optical metallography was difficult due to the fact that retained austenite films could not be resolved. Instead, quantitative X-ray analysis was conducted to measure the volume

fraction of retained austenite. The error estimated from the standard deviation from the average value of volume fraction of bainite is  $\pm 5$ . The error of the volume fraction of austenite measured by X-ray analysis is  $\pm 3$ . The trend is very clear, however; the bainite fraction increased from about 40% at the shortest transformation time to 90% at the longest time, while the martensite fraction decreased from about 60% to less than 5%, as shown in Table 1. At the longest transformation time, the material consisted almost entirely of bainitic ferrite and retained austenite. The presence of retained austenite was confirmed by examining the microstructure at higher magnifications using TEM as shown in Figure 40. The thickness of the bainite plates was in the range of 200 to 400 nm while the retained austenite films were in the range of 15 to 45 nm thick.

**Table 1 Quantitative data on microstructure for banded (non-homogenized) specimens after isothermal heating at**

**573K(300°C)**

Bainitic transformation time	$V_b$	$V_m$	$V_\gamma$
30 min	40	57	3
60 min	64	28	8
90 min	79	13	8
120 min	86	11	3

$V_b$  is the volume fraction of bainitic ferrite;  $V_m$  is the volume fraction of martensite;  $V_\gamma$  is the volume fraction of

austenite.



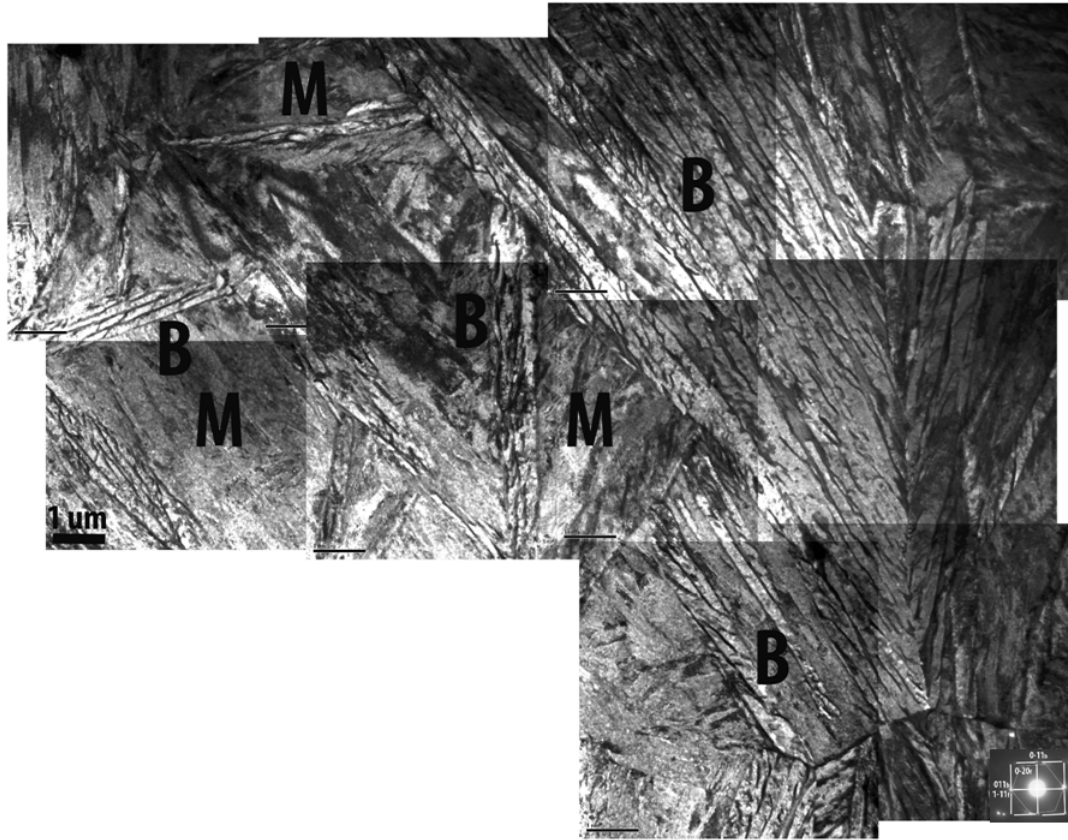
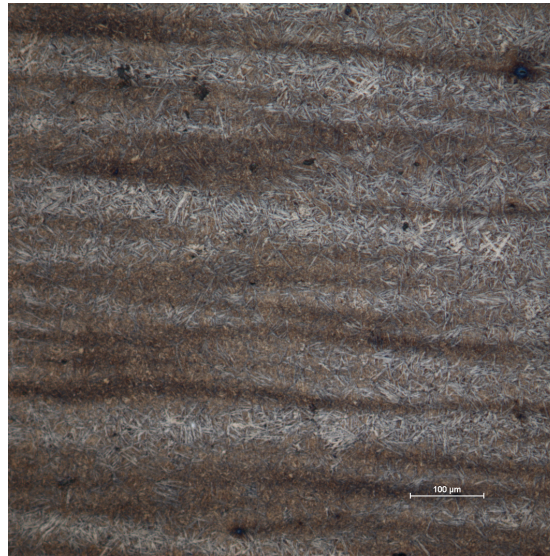


Figure 40 TEM micrograph of a specimen that was austenitized at 1133K(860°C) for 10 min and isothermally transformed at 573K(300°C) for 30 minutes. The microstructure consists of bainite, martensite and retained austenite.

### 3.2.2 Banding Structure

The banding structure at the macroscopic scale is obvious after the two-step isothermal heat treatment; it is primarily due to Mn segregation during casting. Since the equilibrium content of Mn in the liquid is different from that in the solid phase, the regions that solidify earlier have less Mn content than the regions that solidify last. In

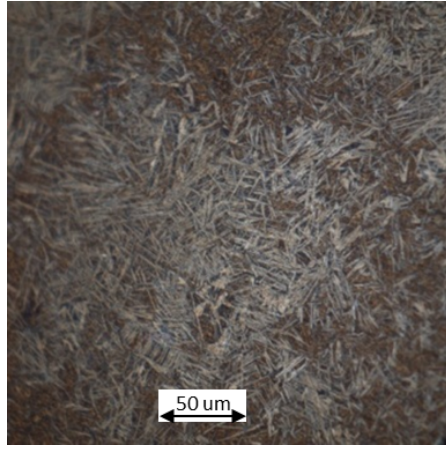
the non-homogenized specimens, bainite appeared to precipitate in bands that presumably coincided with the low Mn regions, Figure 39(a, b, c, d). This is explained by Kirkaldy et al. who noted that the  $A_{r3}$  temperature is influenced by the Mn content [86]. During cooling, ferrite forms first in low-Mn regions with a high  $A_{r3}$  temperature, and austenite remains in high Mn bands with a lower  $A_{r3}$  temperature. Moreover, since ferrite has negligible solubility of carbon, carbon can be partitioned from the first transformed regions to the neighboring austenite phase, which further depresses the  $A_{r3}$  temperature. These latter regions then remain austenitic, or transform to ferrite or martensite, depending on their stability. We conclude that severe banding structure appears in this carbide-free bainitic steel by optical microstructure characterization at low magnification due to the high Mn content which was present to promote hardenability and strength. The bands of martensite were revealed as the darker etched regions in Figure 41.



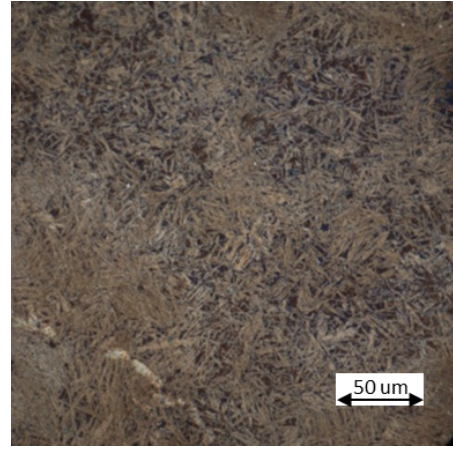
**Figure 41 Severe banding appears in the carbide free bainitic steel due to the high Mn content.**

The difference in microstructure between the low and high Mn regions is greater with the shorter isothermal bainite transformation time. After isothermal heat treatment at 300°C for 30 minutes, the Mn-enriched regions consisted mostly of untransformed austenite which transformed to form fresh martensite during quenching to room temperature. In order to evaluate the effect of banding structure on mechanical properties at the macroscopic scale, the material was homogenized. The material was heated above the austenitization temperature for enough time to let all the chemical elements in the material diffuse to reach a more homogeneous status. In our case, specimens were heated at 1273K (1000°C) for 72 hours in an argon atmosphere and then cooled in air to room temperature. The same bainite heat-treatment procedure was carried out after homogenization. The homogenization treatment was effective at eliminating banding

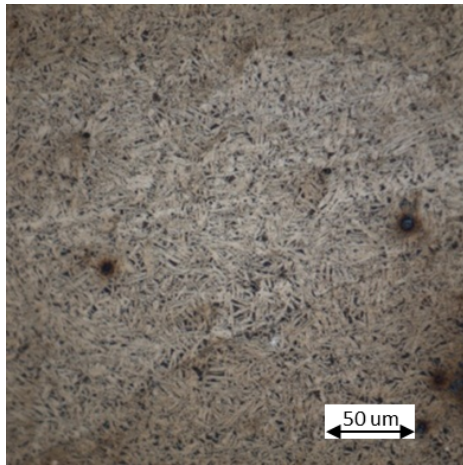
within the microstructure as shown in Figure 42(a, b, c, d).



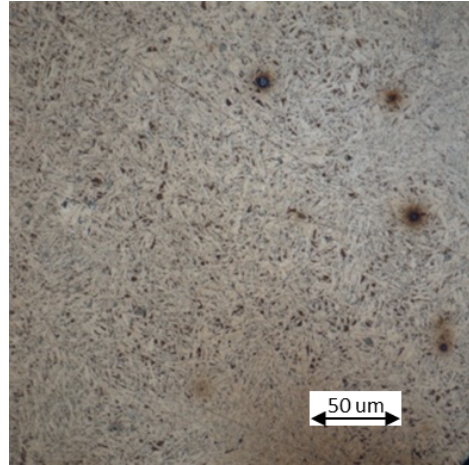
(a)



(b)



(c)



(d)

**Figure 42 Microstructure of the homogenized specimens isothermally transformed at 573K(300°C) for (a) 30, (b) 60, (c) 90 and (d) 120 minutes.**

The volume fractions of bainite were precisely quantified by optical metallography on the homogenized specimens. Quantitative X-ray analysis was conducted to measure the volume fraction of retained austenite due to the fact that retained austenite films could not

be resolved by optical metallography. The error estimated from the standard deviation from the average value of volume fraction of bainite is +/-5. The error of the volume fraction of austenite measured by X-ray diffraction is +/-3.

**Table 2 Quantitative data on microstructure for homogenized specimens after isothermal heating at 573K(300°C)**

Bainitic transformation time	$V_b$	$V_m$	$V_\gamma$
30 min	44	51	5
60 min	67	25	8
90 min	81	9	10
120 min	85	8	7

$V_b$  is the volume fraction of bainitic ferrite;  $V_m$  is the volume fraction of martensite;  $V_\gamma$  is the volume fraction of austenite.

## 3.3 Mechanical Testing Results

### 3.3.1 Tensile test results

#### 3.3.1.1 Comparison among specimens transformed for 30/60/90/120min

The nominal stress-strain curves for the banded and homogenized materials are shown in Figure 43(a) and (b), respectively. For each testing condition, the reproducibility of the data was within +/- 50 MPa at the tensile strength.

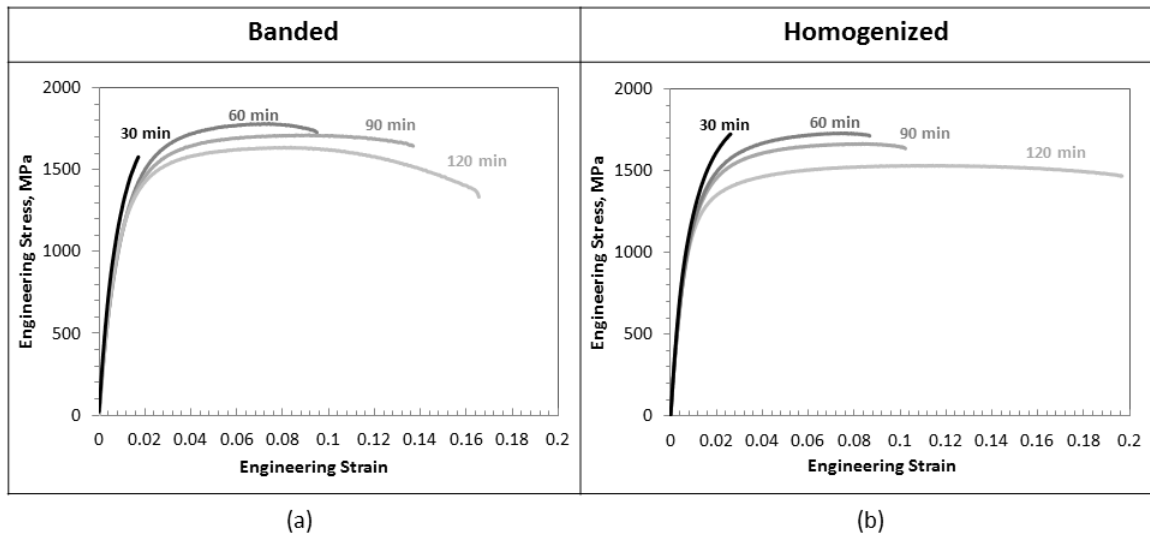


**Figure 43 Effect of the bainitic transformation time on the engineering stress-strain curves of the (a) banded and (b) homogenized steels.**

The measured yield strength, ultimate tensile strength and uniform elongation as a function of the transformation time are summarized in Table 3. The highest tensile strength was achieved at the shortest transformation time (highest martensite fraction). With increasing bainitic transformation time, the strength of the steel decreases and the uniform elongation increases. After 120 minutes at 573K(300°C), the tensile strength is of the order of 1600 MPa and area reduction is in excess of 0.3. These properties are consistent with those obtained by other investigators on similar steels [8-10, 15, 16]. Overall, similar deformation behavior was observed in the banded and homogenized steels, although the strength of the homogenized specimens was slightly lower than the banded ones for transformation times of 60 and 90 minutes.

**Table 3 Tensile properties at room temperature for both the banded and homogenized specimens as a function of the bainitic transformation time.**

	Banded specimen			Homogenized specimen		
Bainitic transformation time	YS (MPa)	UTS (MPa)	EI (%)	YS (MPa)	UTS (MPa)	EI (%)
30 minutes	996	1556	1.7	997	1727	2.6
60 minutes	945	1920	9.8	1012	1731	7.7
90 minutes	953	1894	13.5	1028	1668	8.4
120 minutes	962	1786	15.3	993	1535	11.4

YS is the yield strength; UTS is the ultimate tensile strength; EI is the uniform elongation

Analysis of the fracture surfaces indicated that fracture is intergranular with the cracks propagating along the former austenite grain boundaries. This is very clearly seen in Figure 44. With increasing bainitic transformation time, the fracture becomes more ductile as expected and the former austenite grain-boundaries appear to play a less important role in the fracture process.



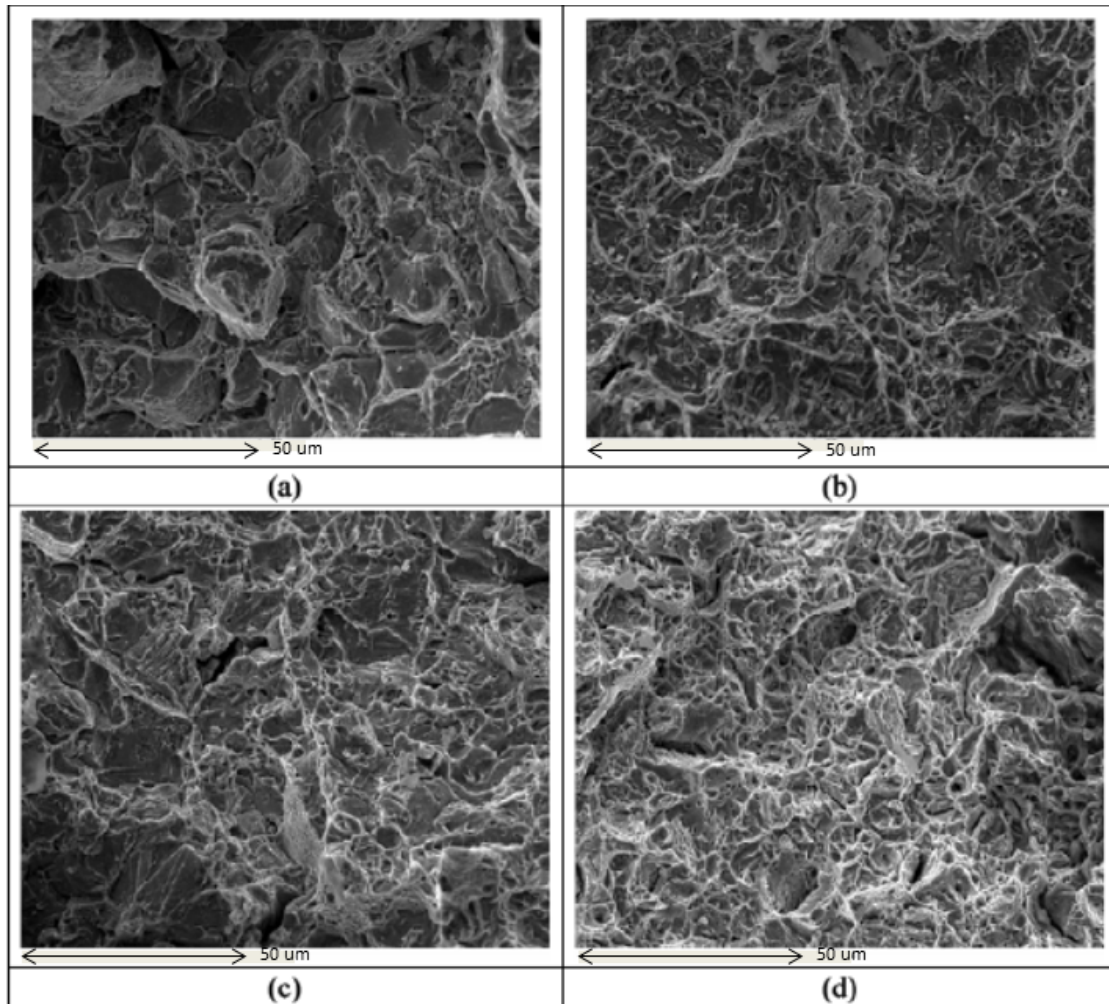


**Figure 44** Fracture surface of the banded specimens transformed at 573K(300°C) for (a) 30, (b) 60, (c) 90 and (d) 120 min.

The measured true fracture strength and area reduction as a function of the transformation time are summarized in Table 4. Within the experimental uncertainty, the steels appear to fail at a constant stress of about 2200 +/- 150 MPa. High true fracture strain could be achieved in the steels that were transformed for the longest times. We have avoided direct comparison between the fracture stresses and reduction area of the banded and



homogenized specimens because of the differences in specimen geometry (flat vs. round specimens). The homogenized samples had a circular cross-section with a diameter of 3mm for tensile testing and 4 mm for Bauschinger testing.

**Table 4 Fracture properties at room temperature for both the banded and homogenized specimens as a function of the bainitic transformation time.**

	Banded specimen		Homogenized specimen	
Bainitic transformation time	FS (MPa)	RA (%)	FS (MPa)	RA (%)
30 minutes	1605	1.7	1826	5.4
60 minutes	2320	24.0	2107	18.6
90 minutes	2100	21.2	2014	18.7
120 minutes	2240	40.2	2139	31.3

FS is the true Fracture stress; RA is the reduction of area

### **3.3.1.2 Inconsistency of specimens transformed for 30min in banded structure**

A notable exception is the reproducibility of the specimens that were transformed for 30 minutes as shown in Figure 45. There are three engineering stress vs. strain curves that

are all measured from the specimens after same bainite heat treatment, which is isothermal bainite heat treatment for 30 minutes.

The large variation in the mechanical properties of these specimens may be due to the large fraction of martensite in these specimens and the sensitivity of martensite to defects. For specimens heated at 300°C after austenitization for 30 minutes, 50 percent volume fraction of the mother phase austenite remained untransformed and sheared to martensite during quenching to room temperature. The fresh martensite as the main component has high strength but is also very sensitive to defects. In most cases, cracks may form and propagate right after yielding in the martensite phase and cause an early fracture of the material (the lower limit in Figure 45). In other instances, the material may survive without crack formation to reach higher deformation strain (the higher limit in Figure 45). As a result, the performance of the specimen after 30 minutes of bainite heat treatment varies by 1000MPa in ultimate tensile strength. The stress-strain curves (Figure 43(a)) reported for specimens transformed for 30 minutes represent the lower limit of the range of observed behavior.

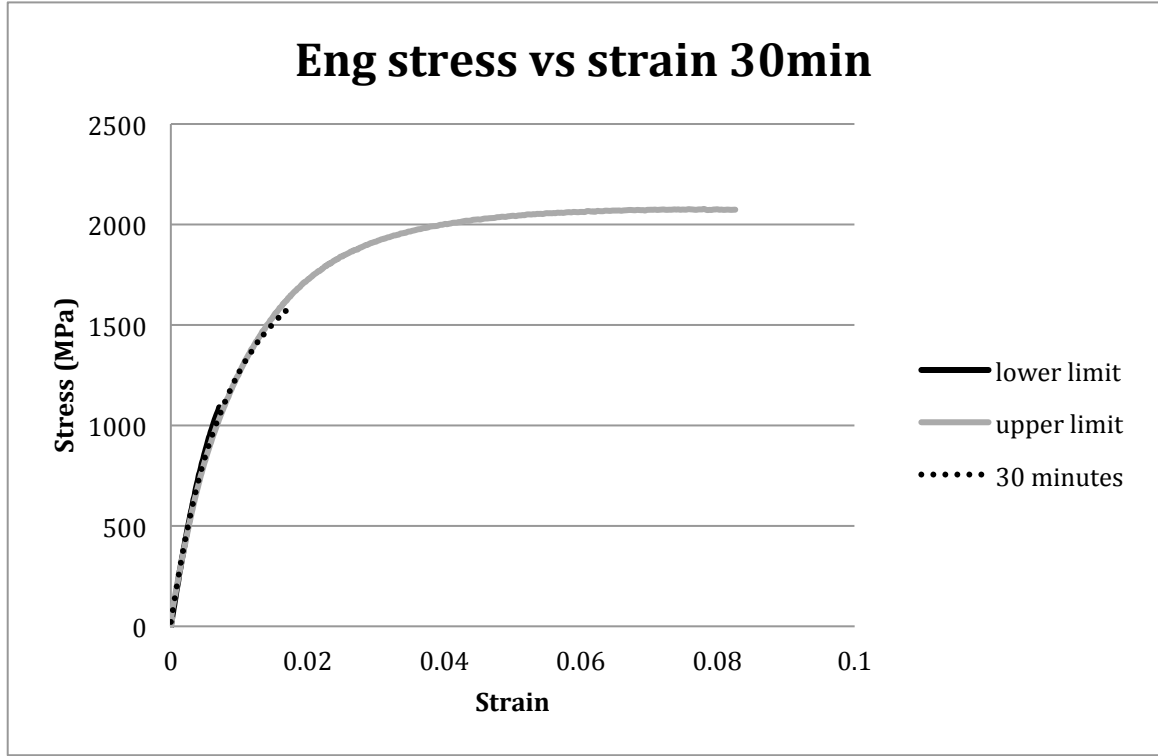


Figure 45 engineering stress-strain curves of the specimens heated at 300°C for 30 minutes

### 3.3.2 Bauschinger tests

The back-stress,  $\sigma_b$ , was estimated from strain-reversal, Bauschinger tests using the 0.01% off-set method [158]:

$$\sigma_b = \frac{\sigma_{.01\%}^F - \sigma_{.01\%}^R}{2} \quad \text{Equation 7}$$

where  $\sigma_{.01\%}^F$  and  $\sigma_{.01\%}^R$  are the 0.01% off-set yield stresses in the forward and reverse loading directions, respectively. Figure 46(a) shows the stress-strain curves obtained from the strain-reversal tests on the homogenized specimens and an example of how the

back-stress was calculated. The evolution of the back stress as a function of the plastic strain in the steel, which was transformed for 120 minutes, is shown for both the banded and homogenized specimens in Figure 46(b). Other transformation times were not investigated because the resulting steels had a limited ductility and a very high strength which could result in buckling during reverse loading. Two features of Figure 46(b) are of special interest; the first is that the back-stress appears to saturate at a strain of 4%. Secondly, the back-stress of the banded material is slightly lower than that of the homogenized material.

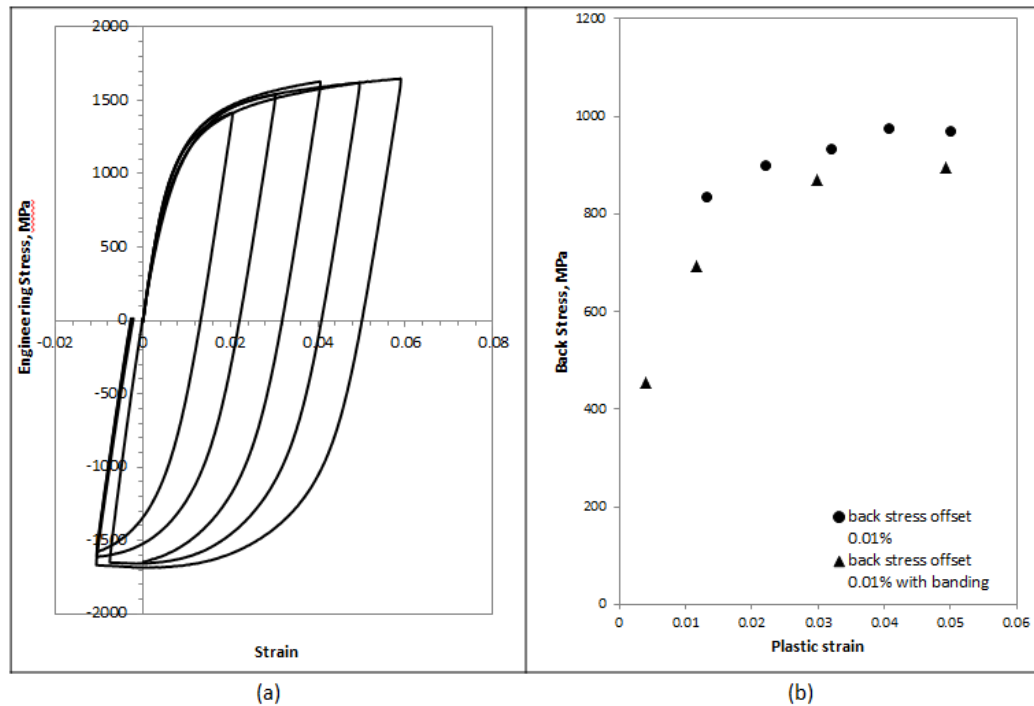


Figure 46 (a) True stress-strain curves obtained from the strain-reversal tests on the homogenized specimens that were transformed at 573K(300°C) for 120 minutes. (b) Back-stress measurements using the 0.01% off-set method

for the same steel for homogenized and banded steel transformed under the same conditions.

### 3.3.3 Strain aging of specimens 90min heat treatment

The reproducibility of the properties of bainite has traditionally been an issue that has hindered its further industrial application. A set of experiments was performed to study whether or not static strain aging was taking place at room temperature in the carbide free bainitic steel. The tensile specimens were heat treated following the regular procedure of isothermal bainite transformation and held at 300°C for 90min before quenching to room temperature. After the bainite heat treatment, each specimen was aged at room temperature for a different period of time (1hour, 1day and 7days) before the uniaxial tensile test. The tensile stress vs. strain curves are shown in Figure 47.

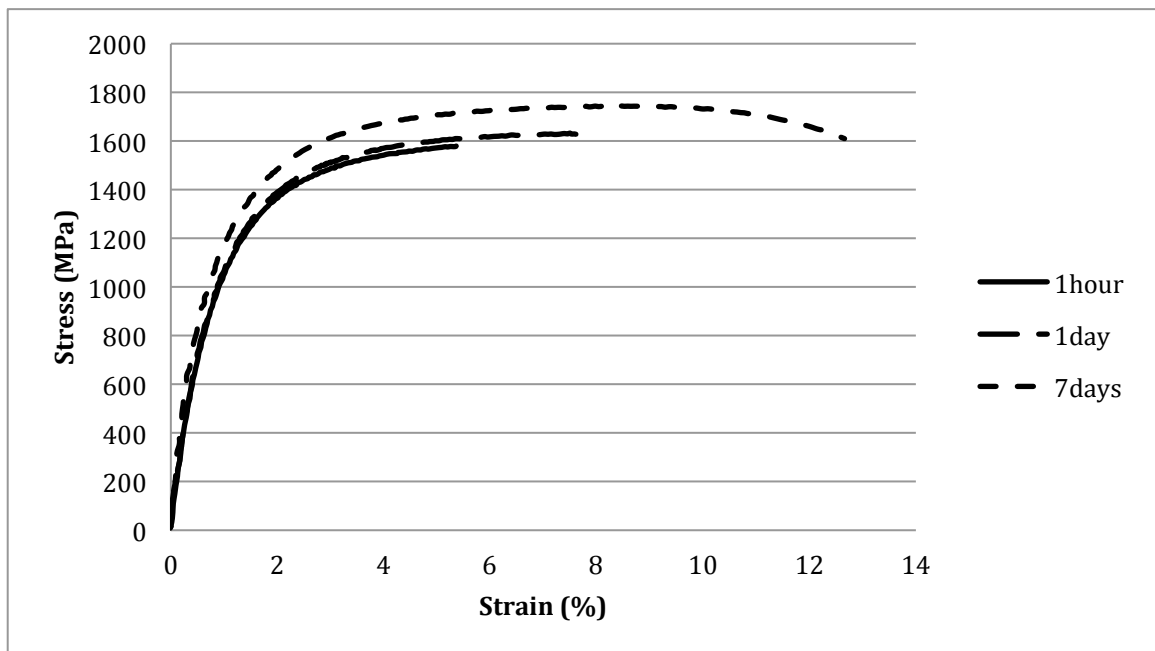


Figure 47 engineering stress-strain curves of the specimens heated at 300°C for 90 minutes and aged at room temperature for different periods of time

The tensile test results are shown in Table 5 below where both the yield strength and the ultimate tensile strength increase while the ductility (uniform elongation) does not change significantly with longer strain aging periods. The yield strength is increased by about 80MPa, and the ultimate tensile strength is improved by more than 100MPa after aging at room temperature for one week.

**Table 5 Tensile and Fracture properties at room temperature as a function of the aging time at room temperature.**

Aging period at room temperature	1hour	1day	7day
YS (MPa)	903	898	983
UTS (MPa)	1619	1654	1740
EI (%)	7.04	8.29	8.77
FS (MPa)	2018	2106	2407
AR (%)	22.42	29.35	41.02

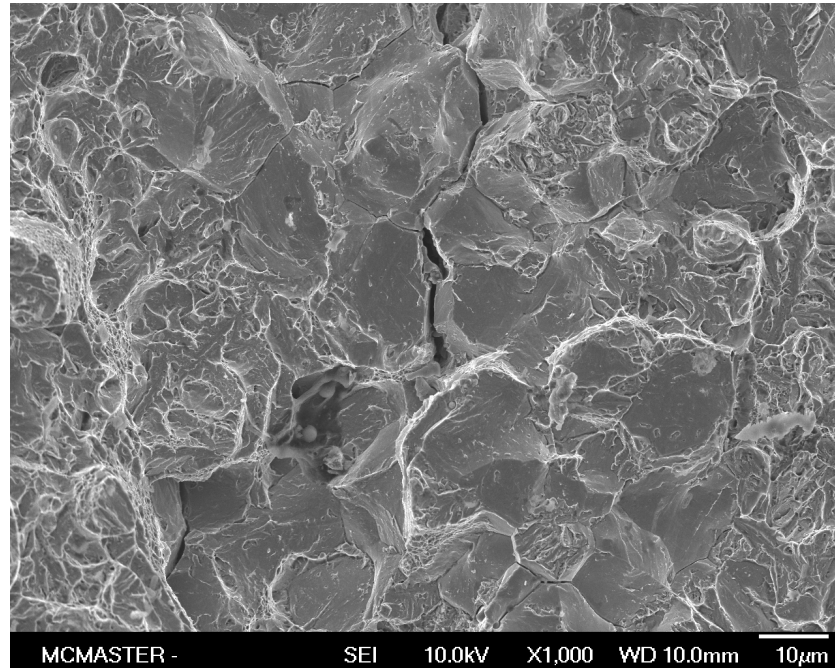
YS is the yield strength; UTS is the ultimate tensile strength; EI is the uniform elongation;

FS is the true Fracture stress; RA is the reduction of area

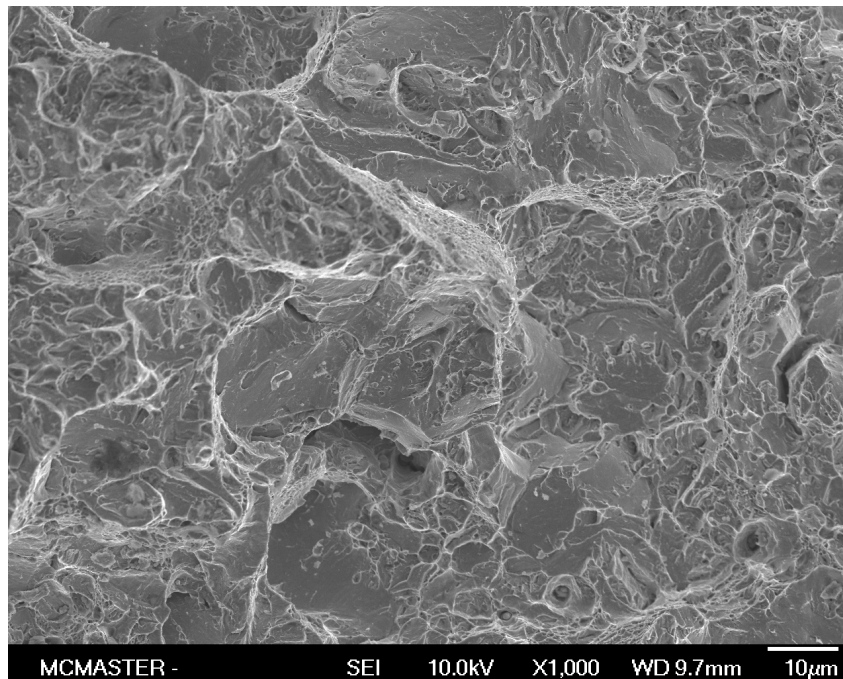
The fracture strength and toughness also follow a clear trend: the longer the aging period, the higher the resistance to fracture. The true fracture strength is increased by 400MPa, and the area reduction undergoes a significant incrementation after aging for seven days.

The fracture surface was observed by SEM microscopy (Figure 48) for tensile specimens

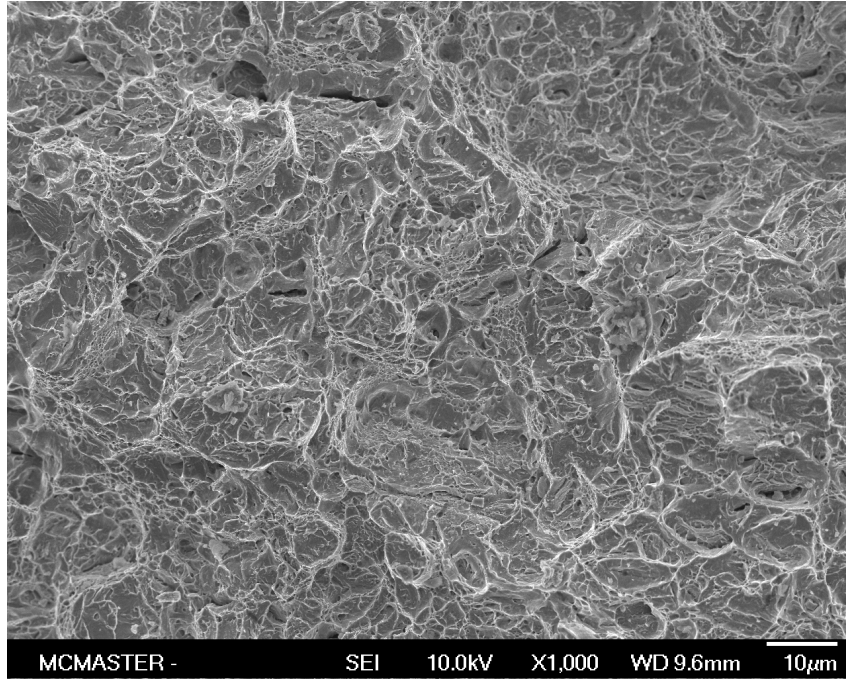
tested after the different periods of aging time.



(a)



(b)



(c)

**Figure 48 Fracture surfaces of the specimens transformed at 573K(300°C) for 90 min and then aged at room temperature for (a) 1 hour, (b) 1day and (c) 7days.**

The crack had propagated along the former austenite grain boundaries showing a typical brittle intergranular fracture surface in Figure 48(a) of the specimen after only 1 hour of aging. Following a longer period of aging, the intergranular features became less obvious. Instead, the fracture mechanism transformed to quasi-cleavage and ductile for the specimen after one day and seven days of aging respectively.



### 3.3.4 Stability of Retained Austenite

The amount of retained austenite after a transformation time of 90 minutes at 573K(300°C) was measured by X-ray diffraction analysis as a function of cold-rolling strain as shown in Table 6. Both the non-deformed specimen and that deformed to a strain of 0.3 had retained austenite fractions in the range of 5 to 9%. The retained austenite fraction dropped to 0-2% after a strain of 1.00.

**Table 6 Volume fraction of retained austenite after a transformation time of 90 minutes at 573K(300°C) after different amount of cold-rolling strain**

Cold rolling strain	Volume fraction of retained austenite (%)
0	5.1 +/- 3
0.3	8.6 +/- 3
1	1.5 +/- 3
2	0.9 +/- 3

This suggests that the retained austenite did not transform during tensile testing, except perhaps during the late stages of deformation, just prior to fracture. The X-ray diffraction results are in agreement with TEM analysis of the deformed material. The TEM results clearly shows that most of the retained austenite films were not transformed in a specimen that was cold-rolled to an equivalent strain of 0.3. This is clearly seen in Figure 49, in which much of the retained austenite is still present between plates of

bainitic ferrite.

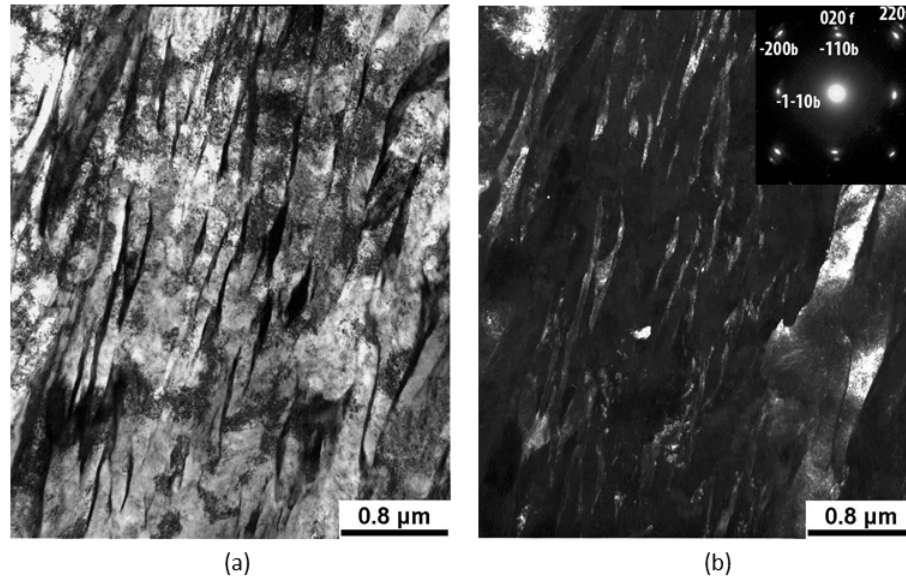


**Figure 49** Retained austenite films are imaged in (a) bright field and (b) dark field in a cold-rolled specimen which was transformed for 90 minutes at 573K(300°C) and cold-rolled to an equivalent strain of 0.3.

### 3.3.5 Prior austenite grain (PAG) refinement

The TEM observation demonstrates the microstructure of the prior austenite grain, as shown in Figure 50. The typical prior austenite grain size after austenitizing at 860°C for 10 minutes was around 28 μm. A set of experiments was conducted to determine how tensile properties and fracture behavior are related to the prior austenite grain size, by changing the latter prior to bainite heat treatment.

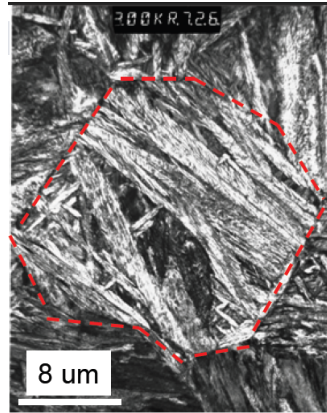


Figure 50 TEM of prior austenite grain [159]

The heat treatment process to modify the size of the prior austenite grain, as described in detail in Chapter 2, was applied as follows: The prior austenite grain size was refined to 12  $\mu\text{m}$  after thermal cycling, and was increased to 50  $\mu\text{m}$  after 90 minutes austenitization. The fracture properties measured from the tensile tests on the specimens with refined, regular and enlarged grain sizes of prior austenite are shown in the table below.

**Table 7 Tensile and fracture properties at room temperature for different prior austenite grain size after 30min of bainitic transformation at 300°C**

	FS	RA
refined PAG	1940.091	0.081048
regular PAG	1831.854	0.081856
enlarged PAG	1663.39	0.016807

FS is the true Fracture stress; RA is the reduction of area

The results confirm that both the fracture strength and toughness increase as the prior

austenite grain size decreases. The fracture surface after thermal cycling and prolonged austenitizing is shown in Figure 51, and is compared to the result of the regular heat treatment. It demonstrates that the prior austenite grain refinement may lead to a transition from the intergranular brittle fracture to the ductile (fibrous) fracture. This transition of fracture mechanism is considered due to the increase of the prior austenite grain boundary area, which requires higher energy for a crack to propagate along the boundaries. Meanwhile, the voids inside the prior austenite grains will initiate and coalesce to cause ductile fracture under plastic deformation.

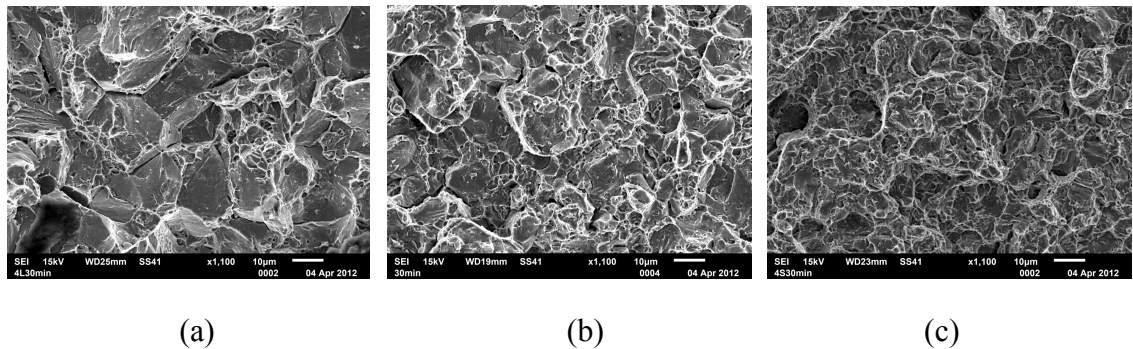


Figure 51 Fracture surface after (a) prolonged austenitizing, (b) regular heat treatment and (c) thermal cycling

## 3.4 Structure-Property Relationships

### 3.4.1 Work hardening behavior

Compared to steels with similar strength, the present steel grade can reach a much higher uniform elongation. In order to help understand this, the true work-hardening rate is plotted as a function of the true stress, Figure 52. This plot reveals that the delayed

onset of necking is due to the high work-hardening rate in the present steels.

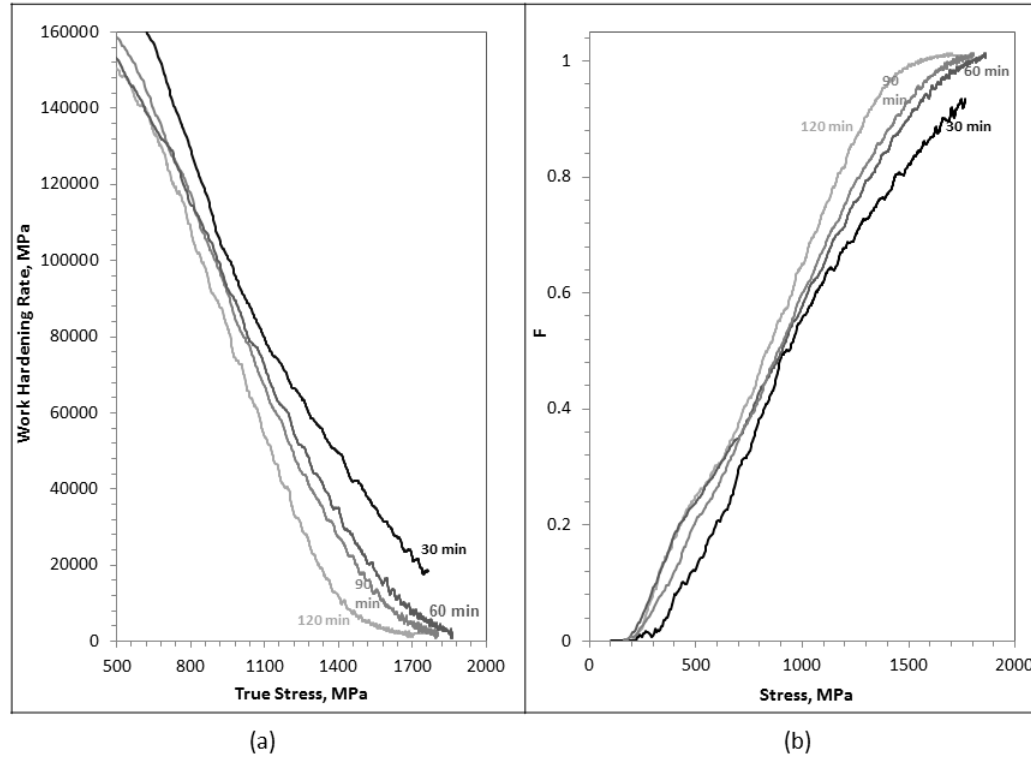


Figure 52 (a) Work-hardening rate as a function of the bainitic transformation time in the homogenized specimens,

(b) the calculated fraction of the material which has yielded ( $f$  in Eq. 2).

Interestingly, the measured work-hardening rates are much larger than the theoretical maximum,  $E/50$  ( $E$  is the elastic modulus), for stage III involving dislocation multiplication and storage [82, 83] in the Kocks-Mecking model. The gradual yielding (i.e. extended elasto-plastic transition) of the material is the main reason of the high apparent work-hardening rate, since the majority of the work hardening is in stage II of the Kocks-Mecking model.

### 3.4.2 Yield Strength

In the gradual yielding or continuous yielding process, the phase with relatively lower strength starts to yield first. As a result, the yield strength of the material is determined by the softest constituent in the matrix. In the case of carbide free bainitic steel, the retained austenite is the softest constituent. [11] It is reasonable to suggest that the yield strength is inversely related to the volume fraction of the soft austenite phase. The yield strength decreases with the increasing amount of the retained austenite in the bainitic steel. [93, 94, 160] However, the volume fraction of retained austenite is below 10 percent for all the specimens after different periods of bainite heat treatment at 300°C, and its thin film morphology is supported by the neighboring bainitic ferrite lath. There are no distinctive changes in volume fraction and morphology of retained austenite in the microstructure while changing the length of isothermal heat treatment time. Thus, the contribution of retained austenite to the reduction of the yield strength level is minor or negligible in this material.

Contrarily, the volume fractions of the bainitic ferrite and martensite changed noticeably as the bainite heating time at 300°C is prolonged from 30min to 120min. As martensite volume fraction in the microstructure decreases from 50% to 10%, the change of yield strength is within the 50MPa margin as shown in Table 3. Accordingly, the martensite as the hardest phase in the carbide free bainitic steel is not the influential factor of the

yield strength.

The yield strength is controlled by the mobility of dislocations to slip in the microstructure under applied deformation stress. The bainitic ferrite grain boundaries can act as a source, sink or barrier to dislocation motion [88, 161], especially with the presence of interlath retained austenite films. The interface surfaces between ferrite and austenite are expected to behave as stronger obstacles to dislocation slip than point defects, such as solute atoms. The boundary surface hinders dislocation movement throughout its entire slip plane length, hence greater resistance to dislocation slip than isolated zero-dimensional obstacles. [88]

The interactions between phase boundaries and dislocations can be described in terms of two effects. The first is the crystallographic misorientation between the two phases near the interface. This misorientation in lattice structure makes it more difficult for the dislocations to pass across the boundaries. Instead of slipping across the phase boundary, a significant amount of the dislocations may accumulate at, or slip along, the boundaries. [162]

Since dislocations themselves are obstacles to dislocation movement, the phase boundary with a relatively high density of dislocations in its neighborhood offers additional resistance to the motion of dislocations. This provides a second interaction between the boundary and dislocations; the dislocation motion is not only hindered by the boundary,

but also by the previously accumulated dislocations. The pile-up of dislocations near phase boundaries strengthens the material. [126]

Among all the possible active slip systems in bainite, 75 percent of them are oriented across the lath axis. Thus the slip band length is strongly controlled by the bainite lath thickness. [79] As a result, the thickness of the bainitic ferrite as the second softest phase in the material is the major factor that controls the yield strength. [91] The smaller the bainitic ferrite lath or plate thickness, the smaller the mean free path of dislocation glide, the greater the yield strength.

The bainite lath or plate thickness decreases with reduced isothermal bainite transformation temperature. In this case, all the specimens were heat-treated at 300°C for bainite formation giving same lath thickness. Thus there was no obvious change in yield strength among all the specimens, even though the volume fraction of the different phases is different due to different heating periods. Other studies on the carbide free bainitic steel under various bainite transformation temperature have shown the trend that the yield strength is improved by reducing the heating temperature for bainite transformation. [18, 159, 163-165] Such an observation proves that there is an inverse relationship between bainitic ferrite platelet thickness and the yield strength. The ferrite lath refinement is the main microstructural contributor to the yield strength.

In conclusion, the yielding behavior of the carbide free bainitic steel is influenced mainly



by the active slip band length of dislocations in the microstructure. This multi-phase material is composed by the bainitic ferrite lath and the inter-lath austenite film in nano-scale, the inter-phase boundary density is relatively high in the microstructure. The phase boundaries act in a number of ways to hinder the dislocation from slipping. Thus, the fineness of bainitic ferrite lath is the determining factor of the yield strength of the carbide free bainite.

### **3.4.3 Masing Model**

The high apparent work-hardening rate in the gradual yielding (stage II) could be rationalized in terms of the Masing model which assumes that the microstructure contains elements with different yield stresses [166]. The application of a Masing-type model seems reasonable in the present case because the microstructure contains several constituents (martensite, bainitic ferrite and retained austenite) and the mechanical contrast between these can account for the range of yield stresses within the material. The different “elements” of the Masing model may also be related to the variety of length scales within each phase as well as the plastic constraints that arise from the way in which the phases are mixed within the microstructure. For example, it is discussed above that the yield strength of each bainitic ferrite lath would depend on the thickness of the lath following the Hall-Petch relationship. Moreover, it is foreseeable that the yield stress of the retained austenite films would depend on the thickness of the films because of the

higher carbon enrichment within thinner films.

The simplest approach for quantifying the elasto-plastic transition or the progressive yielding of the material is to express the measured work-hardening rate,  $d\sigma/d\varepsilon$ , as:

$$\frac{d\sigma}{d\varepsilon} = f\theta_{II} + (1 - f)E \quad \text{Equation 8}$$

where  $f$  is the instantaneous fraction of the microstructure which is deforming plastically under the macroscopic deformation of stress ( $\sigma$ ),  $\theta_{II}$  is the stage II work-hardening rate and  $E$  is the elastic modulus [167, 168]. The first term of Equation 8, represents the contribution of the plastically deforming portion of the microstructure to the global work-hardening rate. The second term represents the contribution to the work-hardening rate from elements that have not yet yielded. During elastic deformation, the strain rate ( $d\sigma/d\varepsilon$ ) is equal to the theoretical Young's modulus ( $E$ ), and the  $f$  is equal to zero. The  $f$  values start to increase from zero as the onset of gradual yielding. It reaches unity when the elasto-plastic transition is complete, and the work hardening rate is equal to the theoretical maximum ( $\theta_{II}$ ). Using the experimentally measured work-hardening rate along with  $E = 200$  GPa and  $\theta_{II} = E/50$ , [169] the value of  $f$  could be calculated as a function of the applied stress as shown in Figure 52(b).

At stresses greater than 1000 MPa, a clear trend emerges; at a given applied stress the specimens with a higher volume fraction of bainite (higher transformation time) have yielded more than those with less bainite. This is expected given the fact that the yield

stress of bainite is lower than that of martensite.

### **3.4.4 Kinematic Hardening**

In addition to the extended elasto-plastic transition described above, the existence of elements with a distribution of yield stresses within the material will lead to the development of back-stresses and associated kinematic hardening in the deformed material. This is consistent with the results of the Bauschinger tests on the samples that were transformed for 120 minutes at 573K(300°C). It is clear from Figure 46 that kinematic hardening makes an important contribution to the total work-hardening rate. The absolute value of this contribution is difficult to estimate; if the 0.01% offset method is used, kinematic hardening would be responsible for almost all of the observed working hardening.

The internal stress increases with the increment of the applied deformation strain. When the material is under deformation, internal stresses are generated in short and long range. The internal stress in short range is mainly due to the dislocation pile-up at obstacles (grain boundaries and inter-phase interfaces). [133] Therefore, the kinematic work hardening is scale dependent; the finer the scale, the higher the internal stresses. In the long range, the internal stress is the constraining stress applied by the neighboring elements with different yield strengths causing directional internal stresses in between them. [130] The Masing model describes this behavior that is also known as the

“composite effect”. [132] The back stress measured from Bauschinger test includes internal stresses in both the short and long range.

The drop in the work-hardening rate with increasing strain corresponds to the saturation of kinematic hardening. In Figure 46, the back-stress saturates at a strain of ~4%. It can be seen, from Figure 52(b), that this strain corresponds to the point at which complete yielding has occurred ( $f=1$ ). It, therefore, appears that the saturation of the back-stress is related to the complete yielding of the material. In other words, the long range internal stress that can be interpreted by Masing model is the main component of the back stress measured from Bauschinger test in this current material.

$f$ , as the fraction of plastically deformed zones can be fit by the Avrami law equation:

$$f = 1 - \exp\left(-\left(\frac{\sigma - \sigma_{\min}}{\sigma_0}\right)^n\right) \quad \text{Equation 9}$$

where  $\sigma$  is the macroscopic stress of the material,  $\sigma_{\min}$  is the minimum stress necessary to start to deform plastically and,  $n$  and  $\sigma_0$  are the parameters that control the shape of  $f(\sigma)$  curve. When the value of  $f$  is zero at the beginning of deformation, the material exhibits completely elastic behavior ( $\sigma < \sigma_{\min}$ ).

The Avrami equation (Equation 9) was fit to all the  $f$ -curves successfully with R-square values above 0.984. The Figure 53 shows the comparison between the original  $f$ -curve and the Avrami fit curve for the specimen after 30 minutes of bainite transformation.

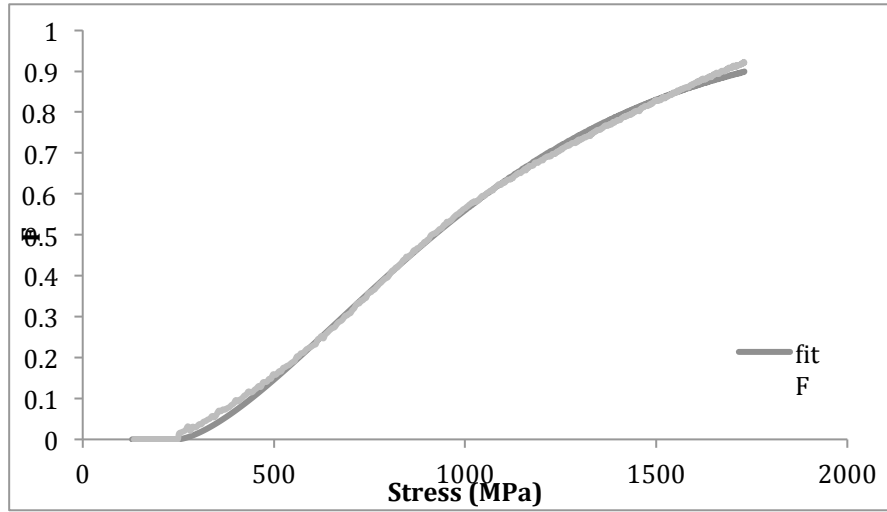


**Figure 53 Comparison between the original F-curve and the Avrami fit curve for the specimen after 30 minutes of bainite transformation**

The values of parameter  $n$  and  $\sigma_0$  for each sample are not fixed, but there is a trend as shown in the Figure 54 and Equation 10: the ratio between  $n$  and  $\sigma_0$  is linearly related to the isothermal bainite heating time.

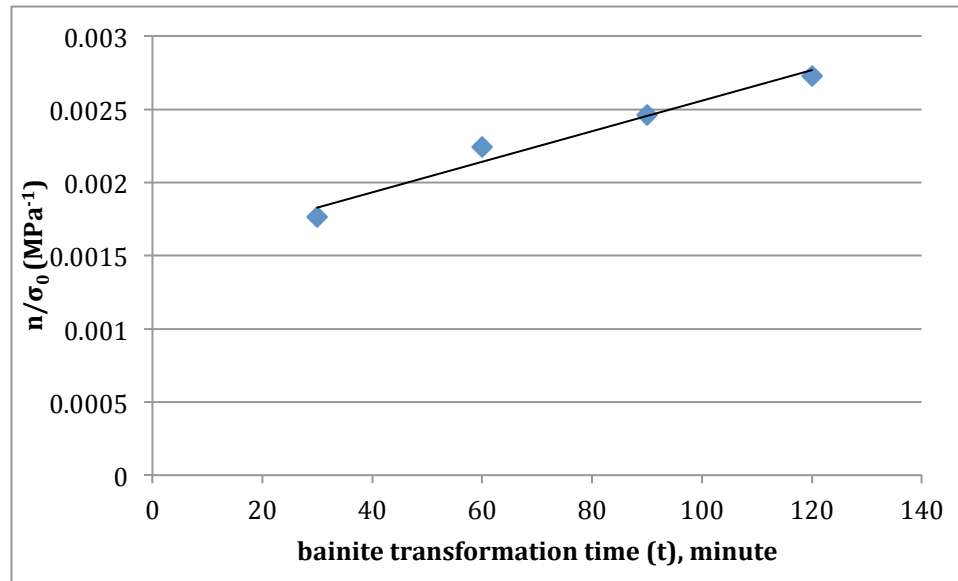


**Figure 54 Linear relationship between bainite transformation time and  $n/\sigma_0$**

$$\frac{n}{\sigma_0} = 0.00001t + 0.0015 \quad \text{Equation 10}$$

All the Avrami fit curve for samples after 30, 60, 90 and 120 minutes are presented in Figure 55 below.

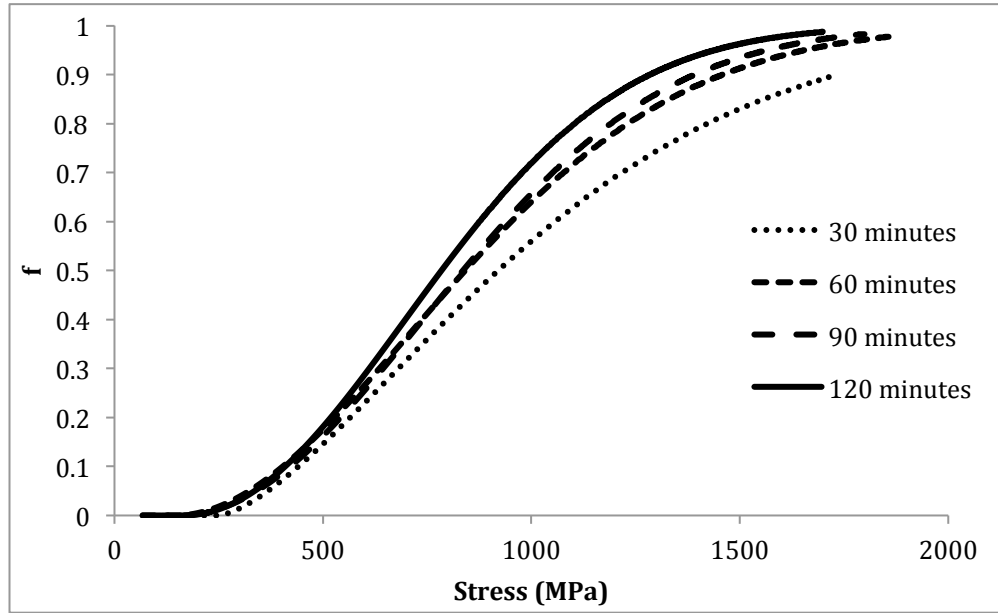
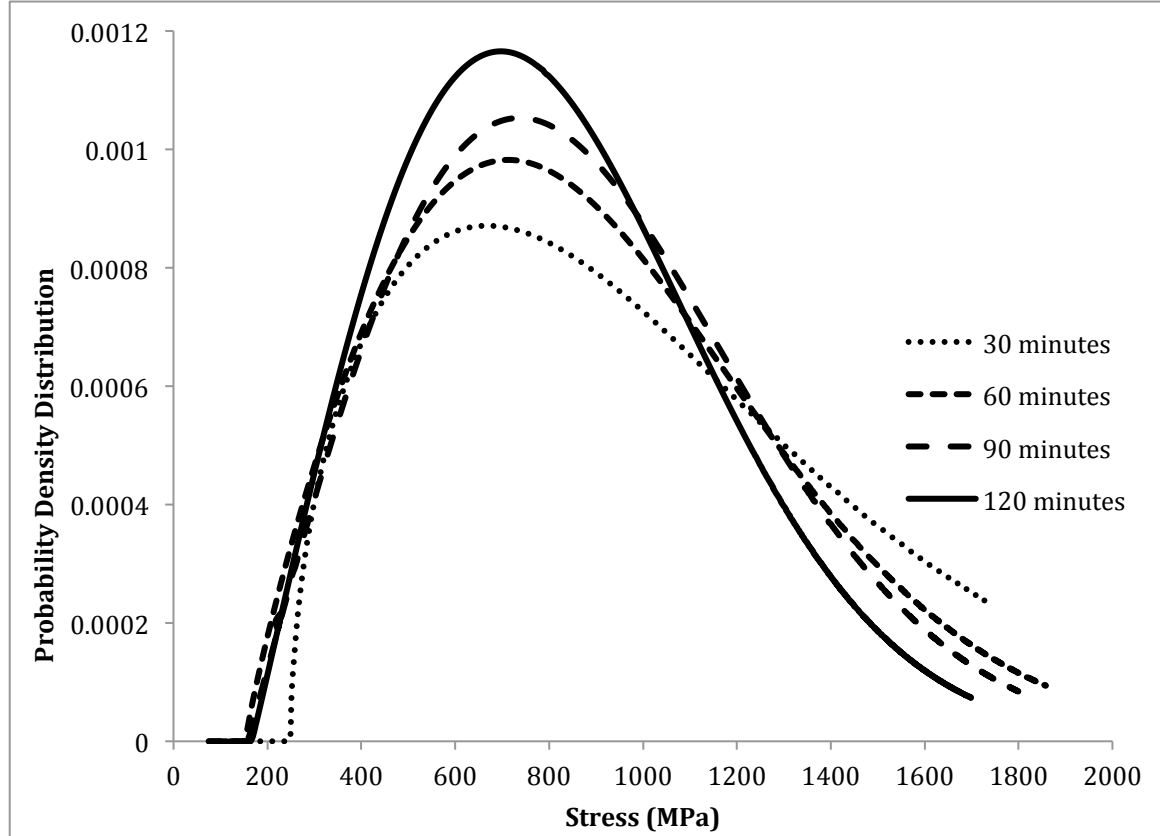


Figure 55 Avrami equation to fit the Volume fraction of elements in the plastic regime of specimens after bainite transformation for 30, 60, 90 and 120 minutes at 300°C

The quantity  $f$  value represents a continuous distribution of yield levels where the element starts to deform plastically. All the  $f$ -curves have the trend of flattening in the beginning and the end of the deformation, when all the elements are deformed elastically and plastically respectively. It shows a normal distribution in the elasto-plastic region with a peak in the middle. By taking the derivative of the  $f$  value, we can get the probability density function of elements in the Masing model with different yield stress levels with a

normal distribution. This is shown in Figure 56.



**Figure 56 Probability density distribution function of elements with different yield stress levels for specimens after bainite transformation for 30, 60, 90 and 120 minutes at 300°C**

As the bainite heating time increases, indicating a higher volume fraction of bainite replacing martensite, the peak of the density distribution functions becomes narrower. In other words, the difference of probability density of the elements with different yield level is more severe for materials with the maximum volume fraction of bainite. The yield stress level of approximately 1000 $\pm$ 40MPa is common for all of the specimens with different bainite transformation times. The longer the bainite transformation time,

the higher the value of maximum probability density that can be achieved. The reverse trend is observed for elements with yield stress higher than 1250 MPa: the longer the bainite transformation time, the lower the probability density, corresponding to a decreasing volume fraction of martensite with increasing bainite heat treatment time. All this evidence suggests that the elasto-plastic transition finishes earlier and faster as the volume fraction of bainite increases. The internal stress (back stress), due to the difference of yield levels between elements in the material, is more important in materials with greater amounts of bainite and martensite. Nevertheless, the back stress cannot be successfully measured on carbide free bainitic steel with 50% of martensite by Bauschinger test because the material is too brittle for cyclic loading.

The results and analyses described above suggest that the back stress of the material after shorter bainite heating time is even higher than that measured from the same bainitic steel after transformation for 120 minutes, resulting in 85% volume fraction of bainite. Accordingly, a 50% volume fraction of martensite and bainite can have higher kinematic work hardening, thus delaying the onset of necking, and resulting in a greater combination of strength and ductility. This is in agreement with the experimental result, shown in Figure 45, demonstrating that some specimens after 30min at 300°C can reach 2070MPa UTS with 8% uniform elongation. Moreover, referring to the Table 2 and Table 3, there is a clear trend that the higher the volume fraction of martensite, the greater



the ultimate tensile strength. This trend suggests that the carbide free bainitic steel with a high volume fraction of martensite can reach greater strength not only because of increased hardness of the martensite phase, but also because of its contribution in kinematic work hardening behavior.

On the other hand, results in Figure 45 also show that, in some cases, these materials (with approximately 50 percent of volume fraction of martensite) cannot survive to the necking point without failure occurring, due to the brittleness of blocky martensite. This constituent can cause transgranular or intergranular fracture, which will be discussed in more detail in the next section. As a result, the martensite phase is not preferable in the microstructure due to its poor reproducibility, despite potentially contributing to greater kinematic work hardening.

### **3.4.5 Kocks-Mecking Model**

Once the gradual yielding is complete, the subsequent work-hardening behavior can be interpreted in terms of the classical Kocks-Mecking analysis [167, 168]. Figure 57, shows the work-hardening rate as a function of (a) the applied stress and (b) the reduced stress,  $\sigma - \sigma_y$ .

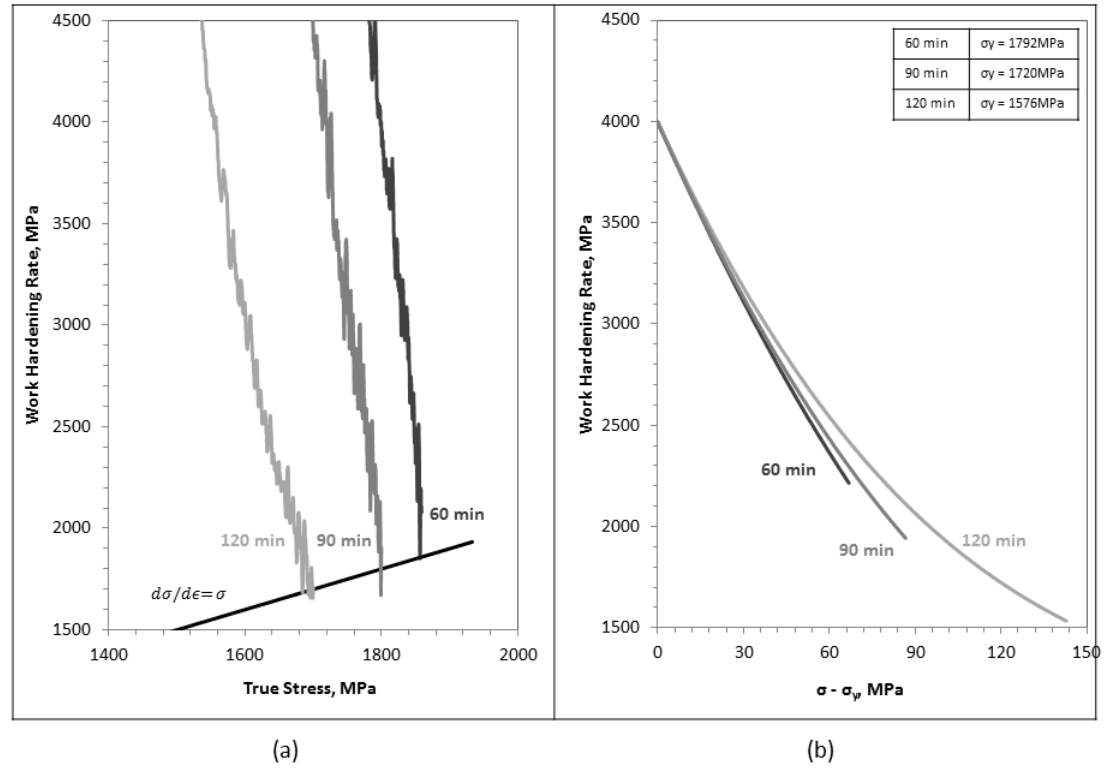


Figure 57 Work-hardening rates of the homogenized specimens as a function of (a) the applied stress and (b) the reduced stress ( $\sigma - \sigma_y$ ).

In order to construct Figure 57(b), the yield stress,  $\sigma_y$ , for each specimen was defined as the stress at which the value of  $f$  in Figure 52(b) has reached unity. Figure 57 contains a number of subtle features that require further discussion:

- The Considère criterion for the onset of necking ( $d\sigma/d\epsilon = \sigma$ ) [170] appears to provide a reasonable prediction for the onset of strain localization as shown in Figure 57(a).
- Figure 57(b) confirms that the bulk of the work-hardening in the present steel is related to the gradual yielding of the material. As soon as this contribution saturates ( $f=1$ ), little additional hardening is observed due to dislocation multiplication and

- storage before the onset of necking. In Figure 57(b), the increase in stress between the point of complete yielding ( $f=1$ ) and the point necking is 60 MPa for the specimen transformed for 60 minutes and 90 MPa for the one transformed for 90 minutes.
- At a given applied stress, the work-hardening rate decreases as the volume fraction of bainite increases as shown in Figure 52(a). This could be taken to suggest that the work-hardening rate of martensite is higher than that of bainite. [171] In contrast, at a given reduced stress, the highest work-hardening rate is that of the specimen with the highest amount of bainite. This is probably due to the fact that the bainite in the various specimens underwent different amounts of plastic deformation prior to the complete yielding of the specimen. The bainite in the specimen with the lowest amount of martensite has undergone the lowest amount of deformation prior to the complete yielding of the specimen and as such has the highest work-hardening rate at a given reduced stress.

The great work hardening rate of this carbide free bainitic steel is mainly due to the mixture of phases or elements with a variety of yield strengths in the microstructure. It causes elasto-plastic transition (or gradual yielding) and kinematic work hardening, as a result of an excellent combination of strength and ductility. Additionally, it gives a low yield/ultimate tensile strength ratio (YS/UTS), which can be beneficial to the drawability in the industrial application. In order to avoid early failure and get reproducible and

consistent mechanical behavior, it is suggested to maximize the volume fraction of bainitic ferrite to replace most of isolated brittle martensite.

### **3.4.6 Banded structure**

The general appearances of the stress-strain curves of the banded and homogenized materials are similar. Detailed examination, however, reveals two subtle differences. The first is the difference in back-stress; it is slightly lower in the banded material than in the homogenous specimens. The second is the divergence in strength: the strength of the banded materials is somewhat higher than that of the homogenous material for transformation times of 60 and 90 minutes. The first difference is qualitatively explained in terms of the effect of Mn on austenite decomposition. It is expected that the low Mn regions transform into bands of bainite at the transformation temperature, while the high Mn regions remain largely austenitic. Upon quenching, the austenite regions will transform to martensite. Since the austenite is constrained by the bainite bands, the martensite that forms will be under compression while the bainite bands will be under tension. Because bainite is the softer constituent, the presence of tension in the bainite bands will result in earlier yielding in the tensile direction and this will lead to a lower back stress as per Eq. (1). The higher tensile strength of the banded material transformed for 60 and 90 minutes compared to the homogenous material transformed for the same times may be related to the same transformation stresses described above. It is

likely that the compressive stresses on the martensite component increase the ultimate tensile strength of the banded samples.

### **3.4.7 Strain Aging**

#### **3.4.7.1 Interaction between carbon and dislocations**

The high dislocation density in bainitic ferrite has been observed experimentally by the use of hot-stage TEM. It shows that the growth of bainite is accompanied by dislocation formation in and around each bainitic ferrite lath. [96] Studies using internal friction techniques and atom-probe field-ion microscope techniques confirm the supersaturation of carbon in bainitic ferrite, which means that the carbon content in the bainitic ferrite is higher than its paraequilibrium value. [102-107]

It is originally suggested by Kalish and Cohen in 1970 that dislocations in bainitic ferrite only trap the interstitial carbon atoms, since the substitutional elements require much longer time to partition at the bainite reaction temperature. [172] This is recently confirmed by the atom-probe tomography experimental result. [173] Based on observation from the atom-probe tomography, carbon atoms are segregated on defects. The carbon content in bainitic ferrite is found to be increased with decreasing transformation temperature, suggesting it is correlated with the rise of dislocation density. [173] Dislocation tangles are also observed inside the bainitic ferrite lath by the atom-probe

tomography. These dislocation substructures might trap a greater amount of carbon atoms compared to the single defects or dislocations. [97]

### **3.4.7.2 Strain aging**

Due to the combination of high dislocation density and supersaturated carbon content in the carbide free bainite microstructure, the strain ageing effect should play an important role in the mechanical performance. After aging at certain temperature for a period of time, the carbon atoms may migrate to and pin the nearby dislocations. Consequently, the yield strength of the material may be improved due to the fact that the mobility of dislocations is restrained by the bounded carbon atoms.

Experimental results are shown in Figure 47 and Table 5 for specimens after aging at room temperature for different periods of time. After one week of aging at room temperature, the yield strength is increased by approximately 80MPa. The improvement in strength after aging at room temperature is mainly due to the high amount of solute carbon and dislocation density in the bainite microstructure. It suggests that with sufficient time, the carbon can diffuse to dislocations and prevent them from slipping at room temperature. The attraction and bonding between the diffusive carbon atom and the adjacent dislocation are the cause of the aging effect. There is no yield point elongation (Luder's band formation) in the stress-strain curve in Figure 47, because of the continuous yielding behavior in this material.

The work hardening rate of the specimens after aging for one hour, one day or one week is calculated and presented in Figure 58

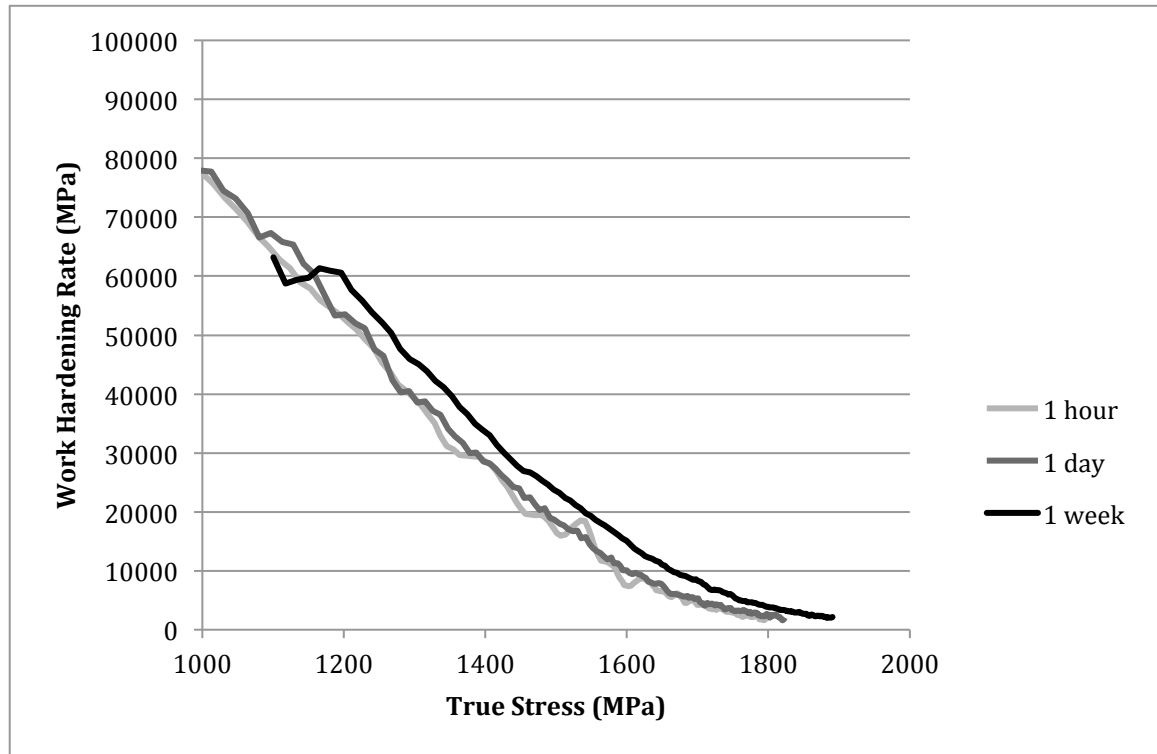


**Figure 58 Work-hardening rate as a function of the aging time at room temperature for specimens after bainite treatment for 90 minutes**

There is an obvious increase in the work hardening rate at the stage II of the Kocks-Mecking model for the specimen after aging for one week. As a result, the ultimate tensile strength is increased by more than 100MPa after aging at room temperature for 7 days, compared to that after aging for one hour. One possible cause of this change in work hardening behaviour lies in the residual stresses within the specimen induced during bainite transformation and quenching to room temperature.

All phase transformations are accompanied by shape change. For ferrite and pearlite, the shape change is reflected as simply change in density and uniaxial volume expansion. On the other hand, bainitic ferrite, Widmanstätten ferrite and martensite grow in the form of thin-plates or lath with a dilatational shape change. Thus, residual stresses are induced microscopically within the microstructure due to the bainite transformation. Moreover, after bainite transformation is complete at 300°C, the specimen is quenched to room temperature. It causes great amount of residual stress caused by the difference in thermal contraction between the center and the surface of the specimen during fast cooling. [174] For the specimen transformed for 90 minutes at 300°C, the thermal contraction strain cannot be cancelled during cooling since the majority of the austenite has decomposed. As a result, a high residual stress is stored in the specimen at ambient temperature after the heat treatment.

The generation of residual stress in the microstructure is therefore due to heat treatment and the bainite phase transformation. The existence of the residual stress may be beneficial or detrimental to the work hardening depending on the stress state of each constituent in the structure. The specimens transformed for 30 and 120 minutes at 300°C were tested by uniaxial compression. The comparison between the stress vs. strain curves in tension and in compression is shown in the Figure 59 below. The specimens after bainite heat treatments behave higher strength in compression than in



tension. The results prove that there are residual stresses in the specimen in tension and that they are detrimental to the mechanical performance under applied stress in tension.

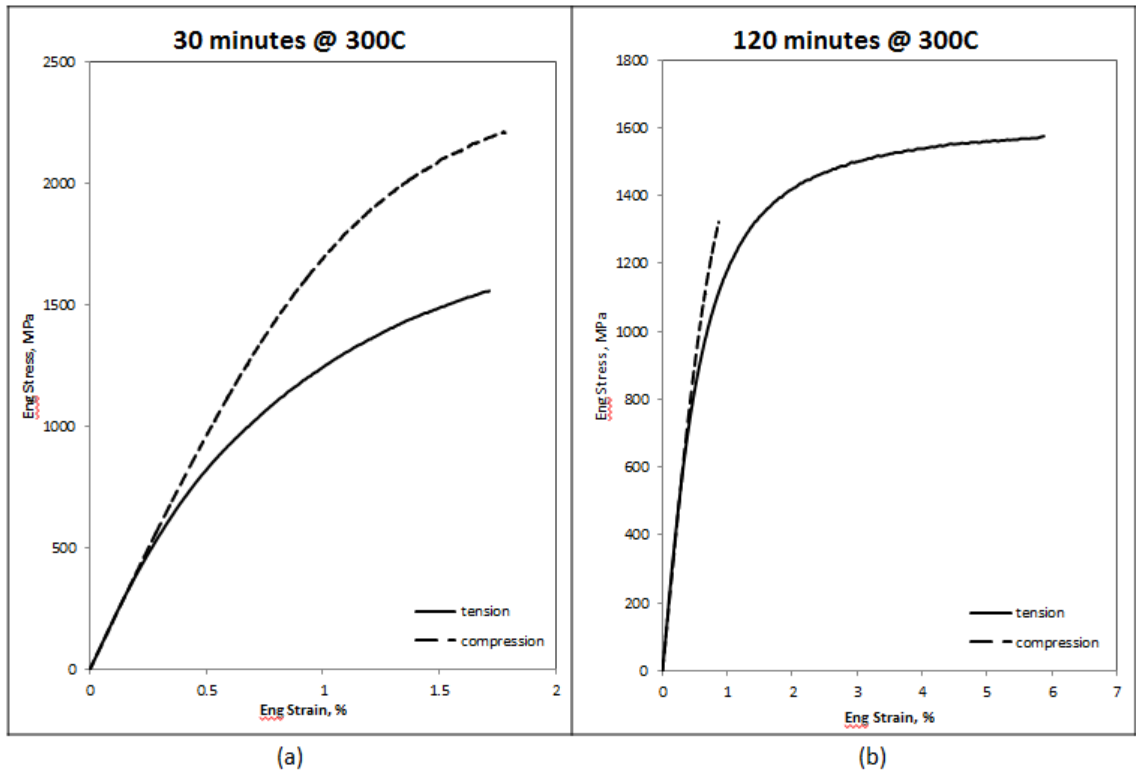


Figure 59 The comparison of the stress vs. strain curves in tension and in compression of the specimen after the same heat treatment (a) isothermal at 300°C for 30 minutes, (b) isothermal at 300°C for 120 minutes

Similar to the interaction between interstitial carbon atoms to dislocations, the interstitial atom also may interact with residual stresses in the microstructure. Under the influence of stress distribution in the material, the carbon atoms are also redistributed. The internal stresses may be reduced or even eliminated by the carbon diffusion.

This relaxation mechanism (due to the diffusion of interstitial solute atoms) is called Gorsky effect. [175] The solubility of the interstitial atoms increases with the rise in the

amount of residual stresses in tension. [174]

The carbon concentration and stress field in the microstructure is derived as follows:

$$C = C_0 \cdot \exp(-U/kT)$$

where  $C$  is a concentration of carbon in a certain point of the field,  $C_0$  is the average concentration,  $k$  is the Boltzmann constant,  $T$  is the Kelvin temperature, and  $U$  is the interaction energy of the interstitial atom with the strain field in the place of a defined concentration,  $C$ .

$$U = \frac{1}{3}(\sigma_{xx} + \sigma_{yy} + \sigma_{zz}) \cdot dV$$

The first term represents the average hydrostatic pressure, where  $dV$  is the change in lattice volume due to the interstitial impurity atom

$$C = C_0 \exp\left(\frac{kT}{dV}\sigma\right)$$

The concentration  $C$  increases under residual stress  $\sigma$ . As a result, the residual stresses attract interstitial impurities. In other words, the residual stress gradient is a driving force for interstitial atom diffusion. The specimen may be strengthened by the reduction in residual stress. Since the carbon atoms are attracted to the residual stress in tension, more stresses in tension are relaxed due to the carbon diffusion. As the residual stresses within the elements in the structure is relaxed, these elements may yield at a higher stress level under the external applied stress in tension. Consequently, the initial work hardening rate is improved. The relaxation of residual stress in tension is time

dependent, since it is correlated to the carbon diffusion. It explains the improvement in work hardening and the ultimate tensile strength as the aging time increases.

Since the dislocations introduced in the austenite phase could be inherited by the bainitic ferrite lath, the dislocation density could be further increased by the thermo-mechanical processing: ausforming. This topic will be presented and discussed in the following chapter.

### **3.4.8 Retained austenite and TRIP effect**

One of the most beneficial factors in the carbide-free bainitic steel is the replacement of the untempered brittle martensite and undesirable coarse carbides by retained austenite in the microstructure. The existence of retained austenite is one of the main reasons that the innovative carbide-free bainitic steel possesses superior mechanical properties when compared to the conventional bainitic steel. The FCC phase austenite is much softer than the other constituent: martensite, ferrite and carbide. Thus, the improvement of ductility can be achieved.

Moreover, the interlath retained austenite films prevent the coarsening of the bainitic ferrite subunits inside each sheaf, during bainite formation. Carbon is trapped inside the austenite films, and stabilizes these austenite films from further decomposition to bainite during the isothermal bainite heat treatment. The thickness of carbide free bainitic ferrite laths is kept at a fine scale even after hours of bainite heat treatment at 300°C.

The mixture of bainitic ferrite lath and nano scale retained austenite films provides a relatively high phase boundary density in the carbide free bainite microstructure. The phase boundaries can promote the strengthening behavior of this multi-phase material in various ways. The ferrite/austenite phase boundaries provide greater resistance to dislocation slip than isolated zero-dimensional point defects (such as solute atoms) and one-dimensional line defects (such as dislocations). As follows, it acts as strong obstacles to the dislocation slip and cause shortening of the mean free path of dislocation glide. [88] The significant strength of carbide free bainite is indirectly attributed to the existence of these nano-sized austenite films between bainitic ferrite laths.

If the TRIP effect were to take place during work hardening stage of the deformation process, it could further improve both the strength and ductility of the material. Since the transformation to martensite involves shape and volume changes, it relaxes the localized concentrated stress at the interphase interfaces and act to suppress void formation. [116] Moreover, the deformation-induced martensite generates dislocations in the surrounding constituents, making it an additional source of dislocations for higher work hardening. [176]

If the TRIP effect takes place at the beginning of elongation of the tensile specimen, it will cause brittle fracture at an early stage of deformation. The austenite would then be so unstable that it transforms into fresh martensite, which may be detrimental to fracture

toughness due to its brittleness. If the retained austenite at room temperature is too stable, then the TRIP effect may not occur before the onset of necking. Then, no TRIP effect will contribute to the delay of necking and the work hardening of the material.

The stability of retained austenite is therefore one of the key contributors to the TRIP effect and needs to be studied in much more detail. The optimum goal is to control and modify the stability of austenite in order to arrange the occurrence of the TRIP effect at the best stage of deformation. The mechanical stability of retained austenite depends strongly on its morphology and its carbon content. In the carbide-free bainitic steel, the retained austenite could either be blocky, surrounded by bainite sheaves, or in the form of film dispersed in between individual ferrite subunits. The stability of these two forms of retained austenite differs due to their different carbon contents.

The carbon content of blocky austenite is significantly lower than that of thin austenite films. [116] Compared to the austenite in thin film, the stability of blocky retained austenite is lowered both thermally and mechanically, due to its relatively low carbon content. As a consequence, the blocky austenite may easily transform to martensite during quenching to room temperature or early stage of deformation. [1] The thin film retained austenite dispersed in between the bainitic ferrite lath is more stable under cooling or deformation than the isolated blocky austenite in the same material.

In this study on the carbide free bainitic steel with 0.4C-2.8Mn-2Si (wt%) after

isothermal heat treatment at 300°C, retained austenite is only observed in the form of thin films. Therefore, the possible contribution of the TRIP effect to the high work-hardening rate is excluded in the present case. According to the X-ray studies of retained austenite before and after deformation by cold rolling, the volume fraction of retained austenite is not decreased after an equivalent strain of 0.3 (Table 6). The high stability of retained austenite is also confirmed by the bright field image obtained from TEM analysis (Figure 49). It suggests that the retained austenite is too stable to transform to martensite during deformation before the onset of necking. Thus, the high work-hardening rates observed in this material is not related to the TRIP effect. This ultra-stable retained austenite results from the fact that the isolated austenite thin films between the bainite plates can accumulate a significant amount of carbon due to the depression of carbide formation. [177]

In order to promote the TRIP effect to further improve the mechanical behavior of this steel grade, different approaches can be used in the future. The carbon content of the retained austenite in the present material needs to be reduced to make the retained austenite less stable under deformation. First, the overall carbon content of the steel grade can be lessened in order to reduce the carbon content in the retained austenite after bainite transformation. Secondly, the deformation of the parent austenite phase (ausforming) before the beginning of bainite transition could mechanically further

promote its stability. Thus, it may increase the final volume fraction of the retained austenite in the material with a lower carbon content in the remaining austenite.

## **3.5 Fracture behavior**

Another interesting feature of the mechanical behavior of the present steels is the high fracture strain (reduction of area); these values are comparable to those reported by Sugimoto from 2000-2002 [115, 116] and Hell from 2011 [178]. This is attributed to the absence of carbides (or cementite) which are known to be detrimental for toughness in these steels. Examination of the fracture surfaces, Figure 44, suggests a transition from brittle, intergranular fracture at short transformation times to more ductile, transgranular fracture at long transformation times.

### **3.5.1 Brittle Intergranular Fracture**

The shiny facets shown on the fractograph of the specimen after 30 minutes at 300°C (Figure 44(a)) is an evidence of brittle intergranular fracture. The brittle fracture surface suggests that crack propagates intergranularly along the prior austenite grain boundaries for the material after 30 minutes bainite heat treatment. This relatively short period of bainite heat treatment does not provide sufficient time for bainite transformation to be completed. Instead, almost 50 percent of untransformed austenite is quenched to form martensite. It has been well reported that martensite as the hardest phase in bainite

microstructure is detrimental to the fracture toughness. The fracture toughness decreases with increasing volume fraction of the brittle martensite in the carbide free bainite microstructure. [7, 80] The fresh martensite, formed displacively during quenching to room temperature, has high strength and hardness but is also very sensitive to defects. Under deformation, the load is transferred to the hard martensite and micro-cracks initiate and nucleate at the martensite where the local stress is concentrated. Crack propagation along the former austenite grain boundaries for the 30 min. specimen may be due to the embrittlement of these boundaries due to solute segregation. A second possibility is that these boundaries are under large stresses due to the lack of plastic accommodation of the phase transformation strains during bainite and martensite formation at low temperatures. The intergranular fracture as shown in Figure 44(a) occurs during the later stages of the extended elasto-plastic transition. It suggests that the fracture is due to plastic incompatibility stresses that could not be accommodated within the microstructure. As the amount of martensite decreases and as the amount of bainite increases during the isothermal transformation, the microstructure can more readily accommodate the incompatibility stresses.

### **3.5.1.1 Inconsistent mechanical behavior**

The engineering stress-strain curves plotted for specimens transformed for 30 minutes (Figure 45) represent the upper and lower bounds of the mechanical properties observed.



The large variation in the mechanical performance of the specimens heated at 300°C for 30mins is due to its sensitivity to defects and the heterogeneous banding structure. Cracks may form right after yielding at locations near the prior austenite grain boundaries and propagate rapidly, causing early fracture with weak ductility and toughness. On the other hand, martensite as the high strength component contributes to the greater strength of the steel. For some specimens where the brittle martensite survives to the later stages of deformation, the carbide free bainitic steel reaches both high strength and ductility, which is the upper bound shown in Figure 45.

In the material with manganese segregation, the bainite and martensite grains are not formed homogeneously. The bainitic ferrite tends to form in the regions with less manganese concentration. The untransformed austenite in the manganese-rich region will shear to form martensite during quenching after 30 minutes of bainite heat treatment. This steel with bands of brittle martensite and ductile bainitic ferrite acts as a composite material. Its mechanical behavior under deformation in tension is a combination of these two components. The carbide free bainitic steel may be reinforced or embrittled by this banding structure depends on its spacing and arrangement. Since these factors are difficult to be controlled or monitored, the banding structure should be reduced or minimized.

The large variation of fracture stress in the specimen transformed for 30 minutes deserves

particular attention. The poor reproducibility and inconsistency of the strength and ductility mechanical properties of the 30 minutes specimens are due to the high volume fraction of martensite and the heterogeneous banding structure due to manganese segregation. In order to avoid early failure and attain reproducible and consistent mechanical behavior, maximizing the volume fraction of bainitic ferrite to replace most of the isolated brittle martensite is suggested.

### **3.5.2 Quasi-cleavage fracture**

The fractographs of specimens after 60 and 90 minutes of isothermal heat treatment (Figure 44(b, c)) reveals some transgranular facets accompanied by significant amount of dimple ruptures. It suggests that both transgranular brittle fracture (cleavage) and ductile fracture processes are operating together, also called “quasi-cleavage fracture”. The size of the cleavage facet characterized by its feather pattern in Figure 44(c) is comparable to the grain size of the blocky martensite shown in the optical micrographs (Figure 39(c)). It indicates that the brittle granular martensite is fractured along its low-index crystallographic plane under tensile stress. The fracture surfaces also exhibit ductile behavior with the characteristic dimples representing the microvoids link-up and coalescence in the bainitic ferrite matrix with relatively greater ductility. The cleavage facets on the fracture surface are surrounded by dimples. It suggests that some ductile constituents in the microstructure can arrest the crack propagation formed in the brittle

martensite grains. Both bainitic ferrite and retained austenite, which are more ductile compared to the martensite, are in fine-scale and could blunt the crack propagation under applied stress. The blocky martensite grains observed in optical micrographs are bounded by sheaves of bainite, corresponding to the cleavage facets bordered with dimples on the fracture surface. Meanwhile, the microvoids are nucleated and begin to grow and link-up during plastic deformation. Thus, the final fracture is caused by the combination of brittle crack propagation and voids coalescence in the ductile phase. Either the brittle cleavage or the ductile void coalescence could be the dominating factor to the fracture behavior.

Moreover, the increment of the volume fraction of bainite in the microstructure reduces or eliminates the broad and continuous martensite bands. The banding structure with regions occupied by mainly martensite provide easy passages for crack propagation. Furthermore, the martensite bands are the preferential sites for the large void formation.

[179] As the bainite transformation time is increased from 30 minutes to 90 minutes at 300°C, the martensite volume fraction is reduced from 50% to 10%. As a result, the martensite connectivity is reduced, resulting in improved damage resistance of the steel.

[180] Due to the contribution from the ductile component in the material, the carbide free bainitic steel reaches higher ductility with longer bainite transformation time.

### 3.5.3 Ductile fracture

As the isothermal heating time increases to 120 minutes (Figure 44(d)), the fracture surface is fibrous and dimpled indicating the ductile fracture mechanism. [88] Dimples are dominating the fracture surface. The brittle martensite phase is reduced to be 5-10% in volume fraction with much finer grain size in the microstructure. Thus, the initial crack size is reduced.

The nano-scaled composite microstructure of bainitic ferrite laths and retained austenite films should be considered to effectively suppress the crack propagation. Since the potential cracks have to overcome not only the interphase interfaces but also different phases with different crystalline structures, between the body-centered cubic ferrite and the face-centered cubic austenite. The retained austenite as the softest phase in the microstructure is a good candidate to impede the crack propagation. It is easier for dislocations to slip in the soft austenite phase, which is beneficial to stress relaxation at the tip of the crack. The presence of the ultrafine films of austenite in between the slender bainitic ferrite laths effectively refines the fracture crack size and dampens the crack propagation.

Ductile fracture takes place when the voids are linked up instead of crack propagation throughout the cross section of a specimen. Micro-voids are initiated not only along the prior austenite grain boundaries but also at the ferrite lath/austenite film interfaces.

Decohesion between the constituents with different strength in the carbide free bainitic steel plays a main role during void growth due to the occurrence of localized shear stress at the inter-phase boundaries. Owing to the presence of a high volume fraction of carbide free bainite in the microstructure, both the initial crack size and the speed of crack propagation are reduced. The fracture mechanism transitions from brittle to ductile fracture, as the isothermal heat treatment time increases, with the increasing bainite volume fraction replacing martensite.

Another important feature of the fracture behavior of the present steels is that failure appears to occur at constant stress of about 2200 +/-150 MPa for specimens transformed for 60, 90 and 120 min. This is consistent with the absence of the classical void growth and coalescence mechanism in these carbide-free steels. Compared to the dual phase steel, the microstructure of the carbide free bainitic steel is much more complex. The fracture may be controlled or triggered by decohesion of certain features of the microstructures such as the former austenite grain-boundaries or the interfaces between austenite and bainitic ferrite due to solute segregation [181].

### **3.5.4 Retained austenite**

The TRIP effect may also occur at the tip of the crack to further promote the fracture resistance. During crack propagation, the retained austenite in the plastic zone near the crack tip can be induced to transform to martensite due to the high concentration of local

stress. The additional toughness can be attributed to the TRIP effect that requires extra energy associated with the work of martensitic transformation. [88] The TRIP effect is beneficial to toughness due to its local stress relaxation and energy absorption.

On the contrary, deformation stress has strong potential to concentrate on martensite phase and isolated unstable blocky retained austenite. Thus, the amount of these constituents should be reduced since they are detrimental to both ductility and fracture toughness. [94] The substitution of inter-lath dispersed retained austenite for carbide as the potential source of crack initiation, and the maximization of the film/blocky austenite ratio is the main criterion for optimum fracture toughness.

### **3.5.5 Prior austenite grain boundary**

The brittle fracture surface shown in Figure 44(a) suggests that crack propagates intergranularly along the prior austenite grain boundaries for specimens after 30min isothermal heat treatment. This may be due to the embrittlement of these boundaries due to solute segregation. Compared to the grain interiors, the grain boundary region has greater absorption potential of environmental impurities such as hydrogen. Besides, the diffusion rate of these impurities is more rapid along the grain boundaries.

A second possibility is that these boundaries are under large stresses due to the lack of plastic accommodation of the phase transformation strains during bainite and martensite formation at low temperatures. The second explanation is consistent with the transition

from intergranular to transgranular fracture with increasing transformation times because it is expected that incompatibility stresses at the boundaries would relax during extended holding at the transformation temperature. In addition, as the bainitic transformation time increases, the amount of martensite formed on quenching is reduced resulting in smaller phase-transformation-induced residual stresses.

#### **3.5.5.1 Aging effect**

Aging at room temperature for different period of times after same bainite heat treatment as shown in section 3.3.3. The fractographs presented in Figure 48 shows the changes the fracture mechanism from intergranular fracture along prior austenite grain boundary to ductile fracture. The fracture surface of the specimen after 1 hour of aging (Figure 48 (a)) shows some facets with a clear crack surface along the prior austenite grain boundaries, representing an intergranular brittle fracture process. As the aging period is extended from 1 hour to 1 day (Figure 48 (b)), there are more patches of dimples as denotation of microvoid coalescence on the fracture surface. The cracks are less noticeable, and the brittle facets are bounded by dimpled areas. For the specimen tested after aging for seven days (Figure 48(c)), the fracture surface becomes fully fibrous with deeper dimples, representing higher ductility and toughness of the specimen.

Carbon dissolved at the prior austenite grain boundaries strengthens the steel. Previous research on carbon steel shows that a small amount of carbon dissipated at the grain

boundaries suppresses the crack initiation at boundaries. The reason behind this is that, unlike embrittling impurities such as hydrogen and sulphur, the interstitial carbon atoms segregate at the grain boundaries increase the cohesive strength of the boundaries. Other than carbon, nitrogen and boron could also act as “grain boundary strengtheners” for the same reason. [182]

### **3.5.5.2 Hydrogen Embrittlement**

Hydrogen is generally associated with corrosion, porosity and crack initiation in metals. [174] Thus, it is considered to be an undesirable element in alloys. Hydrogen at grain boundaries initiates and develops micro-cracks due to internal stresses. Hydrogen embrittlement is one of the factors that may cause early brittle fracture of metals. Hydrogen is an inevitable impurity in the industry environment during steel casting and welding process. [174] The diffusivity and solubility of interstitial hydrogen atoms in alloys are not consistent at room temperature, due to crystal defects and impurities. Since hydrogen atoms can be trapped by defects in the microstructure reducing its mobility tremendously. Thus, the dislocation density not only affects the diffusivity but also the solubility of hydrogen in the metallic material. With an increase in dislocation density, the diffusion coefficient of hydrogen decreases, and the hydrogen solubility increases. As a result, the diffusion coefficient of hydrogen at room temperature ranges from  $10^{-9}$  to  $10^{-5}$  cm<sup>2</sup>/s.



High angle grain boundaries in the microstructure such as the prior austenite grain boundaries in the carbide free bainitic steel is unfavorable for high hydrogen-resistance in steel. On the other hand, the low angle grain boundaries such as inter-lath grain boundaries within each bainitic ferrite packet has high hydrogen resistance, thus a greater resistance to brittle fracture and development of an origin of crack.

### **3.5.5.3 Prior austenite grain refinement effect**

By changing the prior austenite grain size as presented in section 3.3.5, the fracture strength and mechanism can be modified. The brittle fracture behavior is described by the Griffith-Irwin criterion (Equation 11), where the fracture stress  $\sigma_f$  is controlled by the crack size  $a$ . [126]

$$\sigma_f = \sqrt{\frac{EG}{\pi a}} \quad \text{Equation 11}$$

For intergranular fracture, the grain size can replace the crack size  $a$  in Equation 11. Based on the Griffith-Irwin criterion, the critical fracture stress increases if the prior austenite grain size is refined. This is consistent with the improvement of fracture strength and area reduction by refining the prior austenite grain size as shown in Table 7. The fractographs presented in Figure 51 demonstrate a trend that the prior austenite grain refinement may lead to a transition from intergranular brittle fracture to ductile (fibrous) fracture.

By reducing the size of the prior austenite grains by half, the fracture strength is improved by more than 100MPa. This is due to the increment of the prior austenite grain boundary area, requiring higher energy for cracks to propagate along the boundaries. Meanwhile, the voids inside the prior austenite grains nucleate and coalesce to cause ductile fracture under deformation, illustrated by the fibrous fracture surface as shown in Figure 51(c). As a result, it leads to a transition of fracture mechanism from brittle to ductile.

On the contrary, by enlarging the prior austenite grains from 25 $\mu$ m to 50 $\mu$ m, the material is embrittled with a dramatic drop in area reduction from 8% to 1% and in fracture strength by 170MPa. The increase in prior austenite grain causes coarser martensite grains. The larger grain size of the brittle martensite is equivalent to an increase of the initial crack size for brittle failure. In the adjacent bainite areas, the large initial crack causes high stress intensity at the crack tip, and increases the tendency for cleavage. This coarser microstructure is corresponding to the fracture surface with larger clear and flat fracture facets shown in Figure 51(a).

## 4 Ausforming

The mechanical performance of the carbide free bainitic steel been analyzed in Chapter 3 is excellent, but the transformation time are too long for industrial production. Some previous studies suggested that ausforming may accelerate the bainite transformation kinetics. In this chapter, we started by reviewing recent literature on the effect of ausforming on the bainite transformation kinetics and bainite volume fraction (4.1 and 4.2). Two experimental approaches were employed in this study and the results followed by detailed discussions are presented on section 4.3 and 4.4 respectively.

### 4.1 Influence on Bainite Transformation Kinetics

The fact that deformation of austenite at elevated temperatures accelerates the transformation from austenite to ferrite and pearlite was observed and well-established, especially in the initial stage of the reaction. [183] On the other hand, the martensite transformation from austenite is retarded by plastic deformation prior to the phase transformation. As a consequence, the  $M_s$  temperature is lower due to the mechanical stabilization of martensite. [184, 185]

Conversely, the response of bainite transformation kinetics to ausforming is complex and has not been met with a general agreement yet. The reaction kinetics of bainite can either be promoted or retarded by ausforming depending on the deformation temperature.

Among others, Bhadeshia and Shipway investigated the effect of ausforming on bainite transformation kinetics. [150, 151] They proposed that the accumulated dislocation substructures formed in the deformed austenite stifle the bainite growth. Chiou *et al.* and Larn *et al.* later studied the bainite transformation after compressive deformation on the parent austenite phase. They claimed that compressive deformation hinders the formation of sheaf-like parallel plates of bainitic ferrite, and slows down the overall bainite transformation. [152, 153] Their observation is in agreement with research by other groups that the deformation of austenite strongly retards the whole bainite transformation kinetics. [154, 155]

Divergently, Singh *et al.* found that more heterogeneous nucleation sites of bainite are introduced by ausforming, while the growth of bainite plates is reduced by the deformation [146]. Numerous groups of researchers confirmed that there is an initial acceleration of bainite transformation. The incubation period for bainite transformation is shortened after deformation of austenite, even though the bainite transformation kinetics as a whole is dramatically reduced by the deformation [99, 147-149].

On the contrary, some researchers contended that ausforming promotes both the initial nucleation rate and the overall transformation process of bainite. Gong *et al.* recently studied the effect of ausforming on the kinetics of carbide free bainitic steel. They determined using in-situ neutron diffraction that the whole transformation process is

promoted by a small amount of ausforming at the bainite isothermal transformation temperature. In the temperature range between 523K and 673K, it was found that the lower the ausforming temperature, the faster is the bainite transformation kinetics during isothermal holding. The rate of bainite transformation also increases with greater deformation strain during ausforming at 573K. [186]

Further studies are needed to shed light on this controversial topic by relating the bainite transformation kinetics to deformation strain and temperature. A recent study by Xu *et al.* on the ausformed carbide free bainitic steel has shown that the bainite transformation can either be accelerated or retarded by the ausforming, depending on the ausforming temperature. In their study, ausforming at high temperature (860°C) retards the bainite transition kinetics, while ausforming at low temperature (300°C) could promote the bainite transformation. [187]

Finally, Gong *et al.* further suggested that there is a minimal change in bainite transformation kinetics change under a constant applied stress during isothermal heat treatment. The change of bainite transformation kinetics after ausforming is mainly due to the introduced dislocation structure instead of the external stress applied. Since the transformation is accelerated when the strain of ausforming is increased from 15% to 25% at 300°C. [186]

## 4.2 Influence on the volume fraction of bainite

Ausforming not only influences the bainite transformation kinetics, but also determines the maximum volume fraction of bainite. A study by Larn and Lee looked at the effect of deformation of austenite on bainite formation and finds that austenite deformation reduced the maximum volume fraction of bainite. [153, 155] Other groups reported similar results: the final amount of bainite after ausforming is reduced when compared to that produced from un-deformed austenite. [99, 147-149] An explanation for the reduction of the bainite volume fraction after ausforming is the mechanical stabilization effect on austenite due to the dislocation debris introduced to the microstructure. The growth of bainite could be hindered by the mechanical stabilization, similar to what is found in martensite. [21, 150] This statement is in agreement with the evidence that ausforming decreases the bainite start temperature ( $B_s$ ). The  $B_s$  temperature is decreased by the increment of the ausforming strain. [21, 150, 188]

However, Umemoto *et al.* report a result that contradicts the aforementioned, in that the maximum volume fraction of bainite is found to be increased after ausforming at the lower bainite transformation temperature. [189] This is in agreement with Gong and Xu's latest study results indicating that both the final bainite volume fraction and the transformation kinetics are related to ausforming temperature and the deformation level of the parent austenite phase. [186, 187] Ausforming at relatively low temperature has

more influence on the bainite transformation and the final bainite volume fraction, since the dislocation substructure induced by ausforming at high temperature is presumably recovered before the onset of bainite transformation. [186] According to both Guang and He's research results, there is a critical deformation strain level, under which the bainite volume fraction is maximized. [187, 190] The correlation between the maximum bainite ratio and the deformation strain is unclear at the moment; further studies are needed to come to a universal conclusion.

The motivation to study the ausformed carbide free bainitic steel is the possibility that the bainite transformation can be accelerated for industrial applications in the future. Previous studies on the effect of the ausforming process of the carbide free bainitic steel were focused on the bainite transformation kinetics. The mechanical behavior of the ausformed carbide free bainitic steel has not been analyzed due to the limitation in size of the processed specimen.

A set of dilatometric studies on the steel with 0.4C-2.8Mn-2Si (wt%) chemical composition were conducted by our colleagues in China focusing on the bainite transformation kinetics after ausformation. [187] The dilatometer result as shown in Figure 60 suggested that the bainite transformation is promoted initially after ausforming at 300°C. Furthermore, it also demonstrates that with a strain level lower than 25%, the whole bainite transformation is accelerated by ausforming. The dilatation value is

normalized by the instantaneous dilation just before the bainite transformation begins.

[187]

Based on the results of Xu et al [187], a set of experiments was designed with ausforming temperature of 300°C and strain levels of 10% and 20%, followed by isothermal bainite heat treatment for 30 and 60 minutes at the same temperature. In this work, a quantitative microstructure characterization and analysis of the ausformed carbide free bainitic steel have been conducted by EBSD and TEM. The thermo-mechanical process was performed by two methods. The first approach was by the Gleeble thermomechanical simulator, where the pre-machined flat tensile samples were deformed in tension after cooling to 300°C. The second ausforming approach was by rolling the specimen before the onset of bainite transformation at 300°C. The ausformed carbide free bainitic steel was studied by uniaxial tensile test after ausforming by Gleeble in tension or rolling in compression to build the microstructure-mechanical behavior correlations.



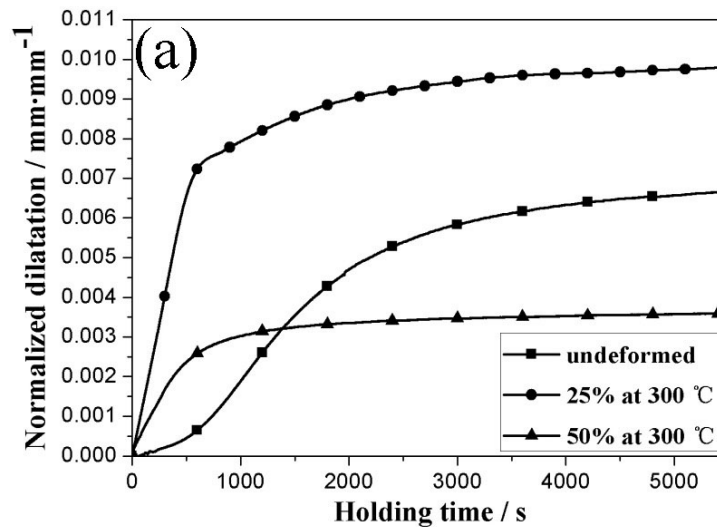
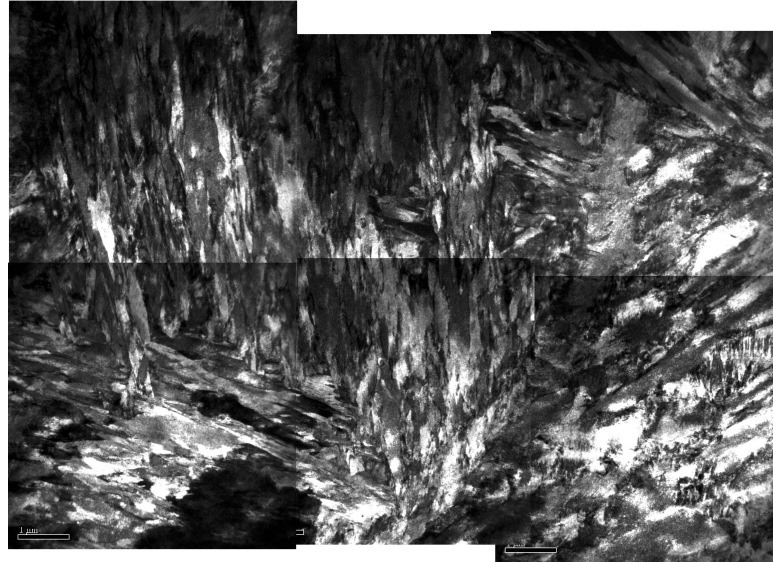


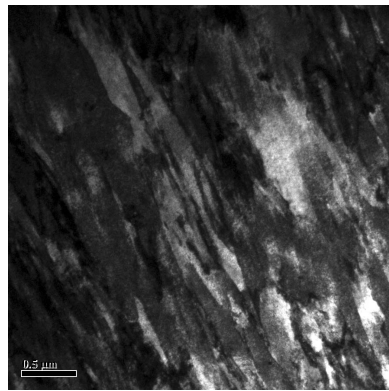
Figure 60 Dilation curves showing the effect of ausforming at low temperature on bainitic transformation. [187]

It should be noted that it is necessary to verify that austenite decomposition does not take place during cooling from the austenitizing temperature down to the isothermal transformation temperature. It is also important to confirm that martensite does not form during ausforming. Thus, a specimen was quenched to room temperature right after ausformation with 25% plastic strain in compression and its microstructure is analysed by TEM. Both the typical plate-shaped martensite with fine twins within plate and the lath-shaped martensite with high density of dislocations were observed in the overview at low magnification as shown in Figure 61(a). The lath martensite with high dislocation density and the fine scale twins in plate martensite are presented in Figure 61(b) and Figure 61(c) respectively in higher magnification. It confirms that the chosen cooling rate and the deformation rate controlled by the Gleeble is fast enough that neither proeutectoid ferrite nor bainitic ferrite phase is precipitating from the supercooled

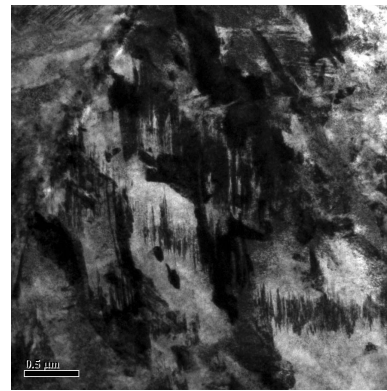
austenite phase right after the ausformation procedure.



(a)



(b)

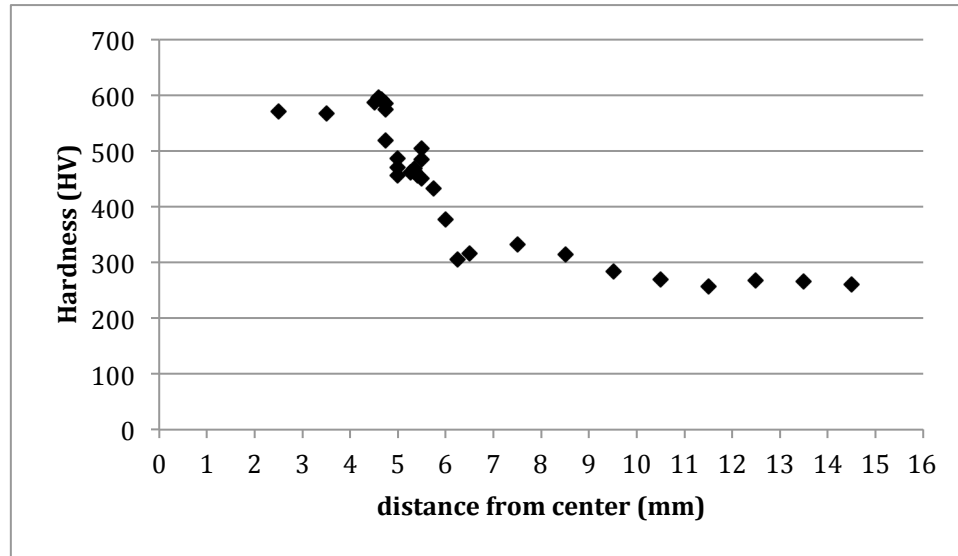


(c)

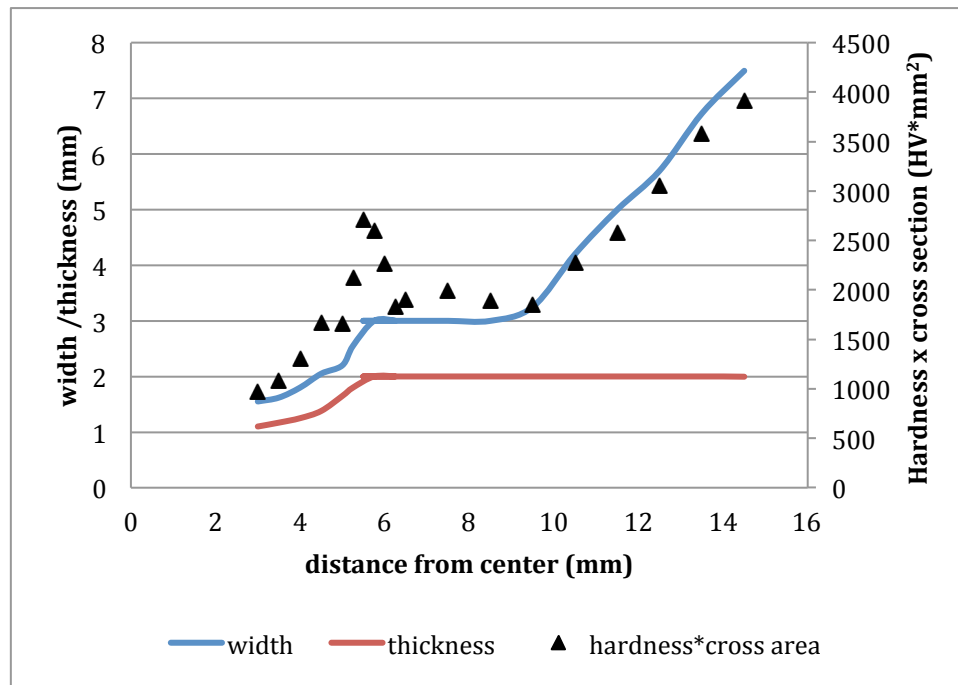
**Figure 61 Full martensite structure in the sample after 25% plastic strain of ausforming in compression at isothermal transformation temperature of 300°C and directly quenched to room temperature. (a) an overview in low magnification, (b) lath martensite with high dislocation density and (c) fine scale twins in plate martensite [191]**

### 4.3 Ausforming by Gleeble

The Gleeble thermo-mechanical simulator was used to pre-deform the austenite at 300°C before the onset of bainite transition. The thermo-mechanical process involved full austenitization at 860°C followed by cooling to 300°C. The flat tensile sample was deformed in tension to strain of 10 or 20%, and held at 300°C of 30 or 60 minutes before quenching to room temperature. The ausforming stress was released right after the required strain was reached. A thermocouple was attached to the center of the specimen to monitor and control the thermo-mechanical process. The microstructure was characterized by optical microscopy and EBSD after ausforming by Gleeble. The hardness was measured throughout the heating zone and the hardness profile is shown in the Figure 62(a). The specimens are later machined into tensile samples with specific gauge length, as well as the thickness and width gradients according to the measured hardness profile. The gauge length was designed to be 5mm according to the measured hardness from the center of the specimen. The thickness and width profiles are designed as shown in Figure 62(b) to make sure the uniaxial loading is concentrated at the gauge of the tensile samples. The specimens were tested in tension and the fracture surfaces were analyzed by SEM.



(a)

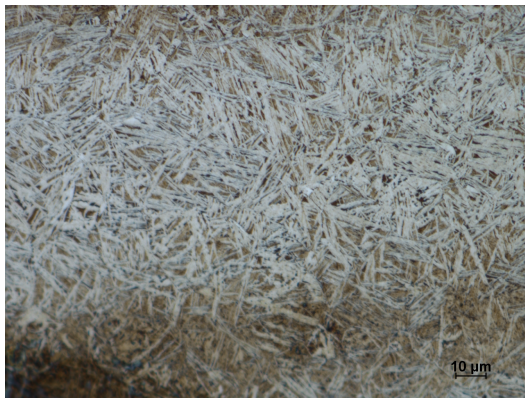


(b)

Figure 62 (a) The hardness profile throughout the heating zone and (b) the width and thickness of the designed tensile samples with the calculated hardness x cross section area

### 4.3.1 Microstructure

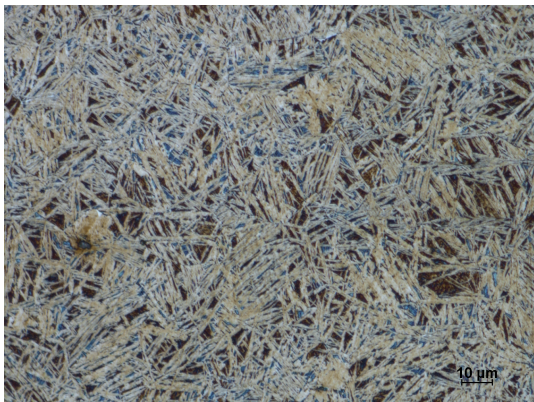
The final carbide free bainite microstructure was influenced by the ausforming strain. The ausforming by Gleeble was done at different strain level: 10% and 20%. The microstructure is analysed by optical microscopy to see the change in morphology, grain size and volume fraction of each phase.



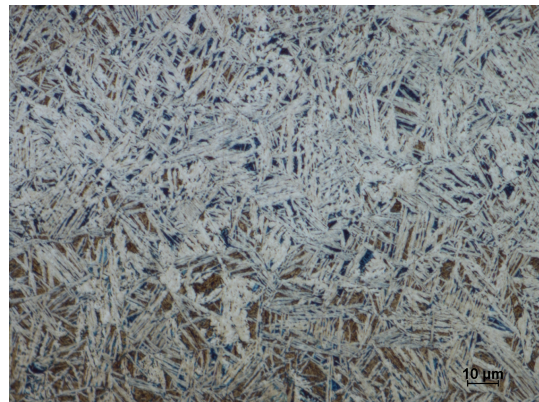
(a)



(b)



(c)



(d)

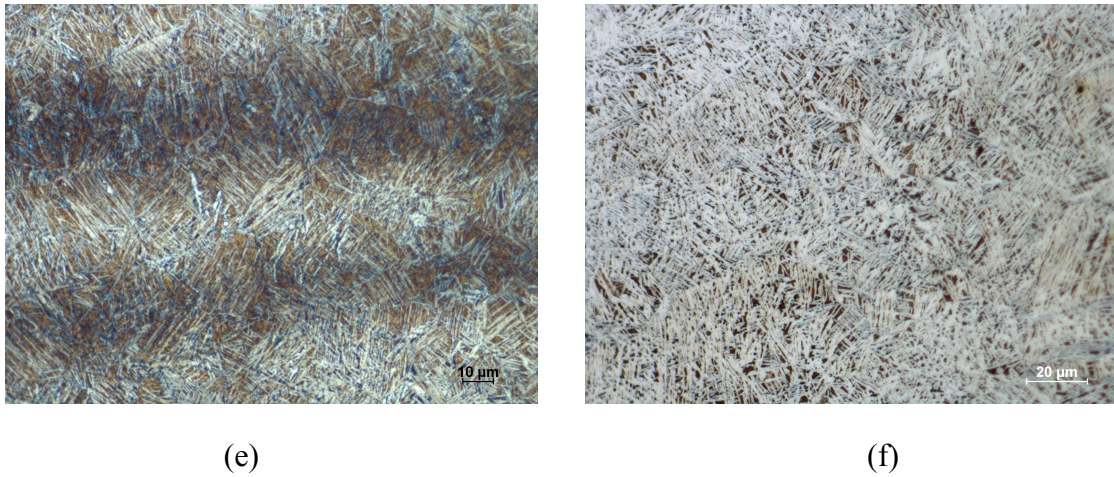


**Figure 63 Optical micrographic images for carbide free bainitic steel after ausforming in tension with strain of 0% followed by (a) 30 minutes and (b) 60 minutes holding; with strain of 10% followed by (c) 30 minutes and (d) 60minutes; with strain of 20% followed by (e) 30 minutes and (f) 60 minutes at 300°C. Bainite: bright phase; martensite/austenite: dark phase.**

The samples were etched using a solution of 40g NaOH, 60g H<sub>2</sub>O and 15g NaNO<sub>3</sub> which can distinguish the bainitic ferrite (white phase) from the martensite/austenite (dark phase). The measurement of the volume fraction of bainitic ferrite was performed manually using the line intercept method. (Figure 64)



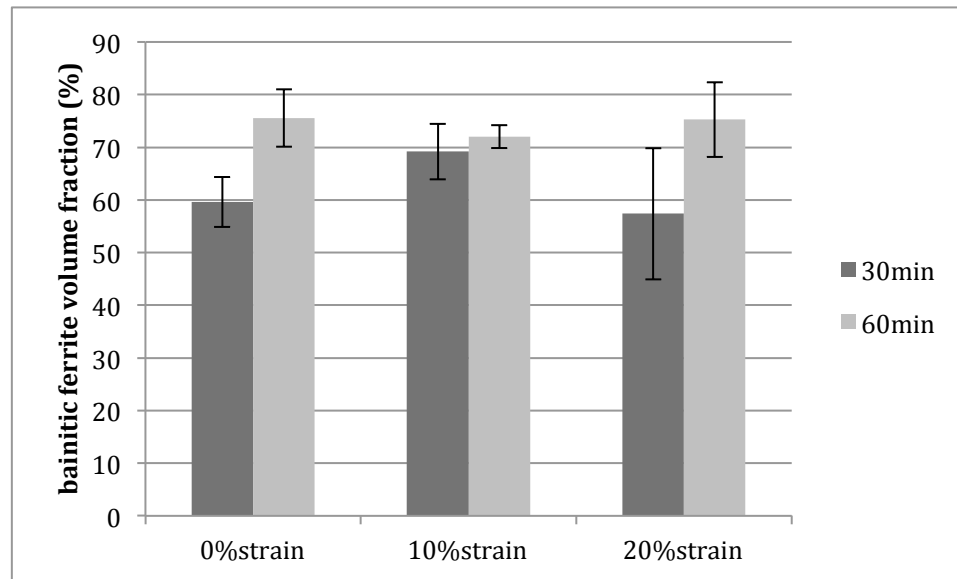
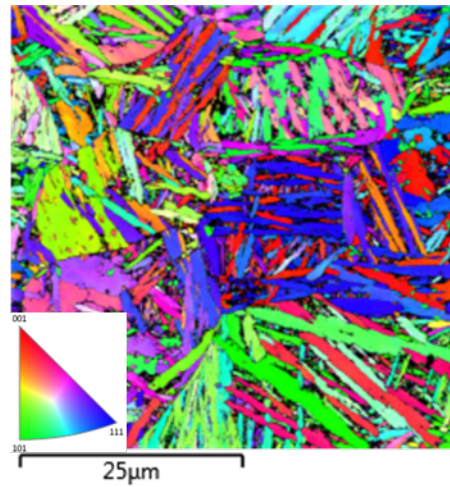


**Figure 64 Volume fraction of bainitic ferrite measured by manual line intercept method**

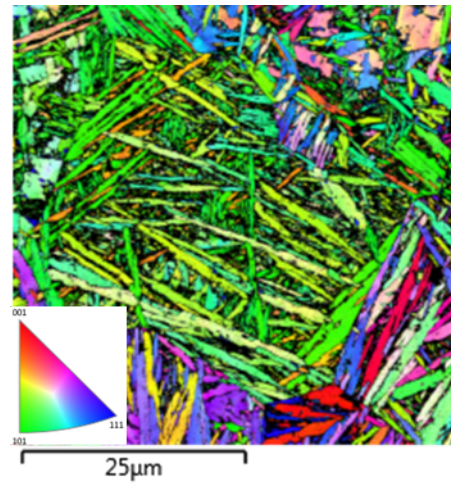
The optical micrographs show that after bainite heat treatment for 30 minutes, there is a subtle reduction in the volume fraction of the bainite after ausforming by 20% of strain (Figure 63 (e)) in comparison with the unausformed material (Figure 63 (a)). On the other hand, the initial bainite transformation is accelerated after ausforming by 10% of strain (Figure 63 (c)). After ausformation followed by bainite isothermal heat treatment at 300°C for 60 minutes, there is no obvious difference in the bainitic ferrite volume fraction between the material under 10% and 20% of pre-strain. Thus, the change in the final volume fraction of bainitic ferrite due to the difference in austenite pre-deformation strain level is negligible.

Due to the complexity of the carbide free bainitic steel structure, the presence of the fine-scaled retained austenite can not be distinguished from martensite by optical

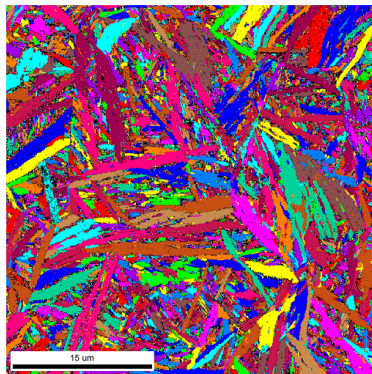
microscopy. It is necessary to use EBSD to scan the ausformed material in much higher magnification with the step size of 50nm. The change in morphology and the volume fraction of the retained austenite were observed by EBSD on the ausformed specimens and discussed in detail in Section 4.3.1.1.



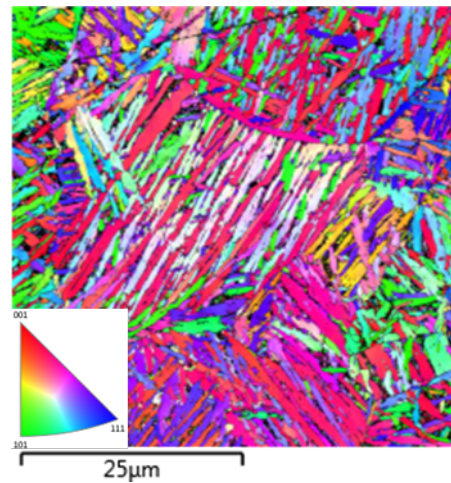
(a)



(b)



(c)



(d)



**Figure 65** The orientation maps of (a) the non-ausformed specimen under bainite transformation for 60 minutes; (b) the specimen ausformed (10% strain) in tension before bainite transformation for 30 minutes; (c) the specimen ausformed (10% strain) in tension before bainite transformation for 60 minutes; (d) the specimen ausformed (20% strain) in tension before bainite transformation for 60 minutes.

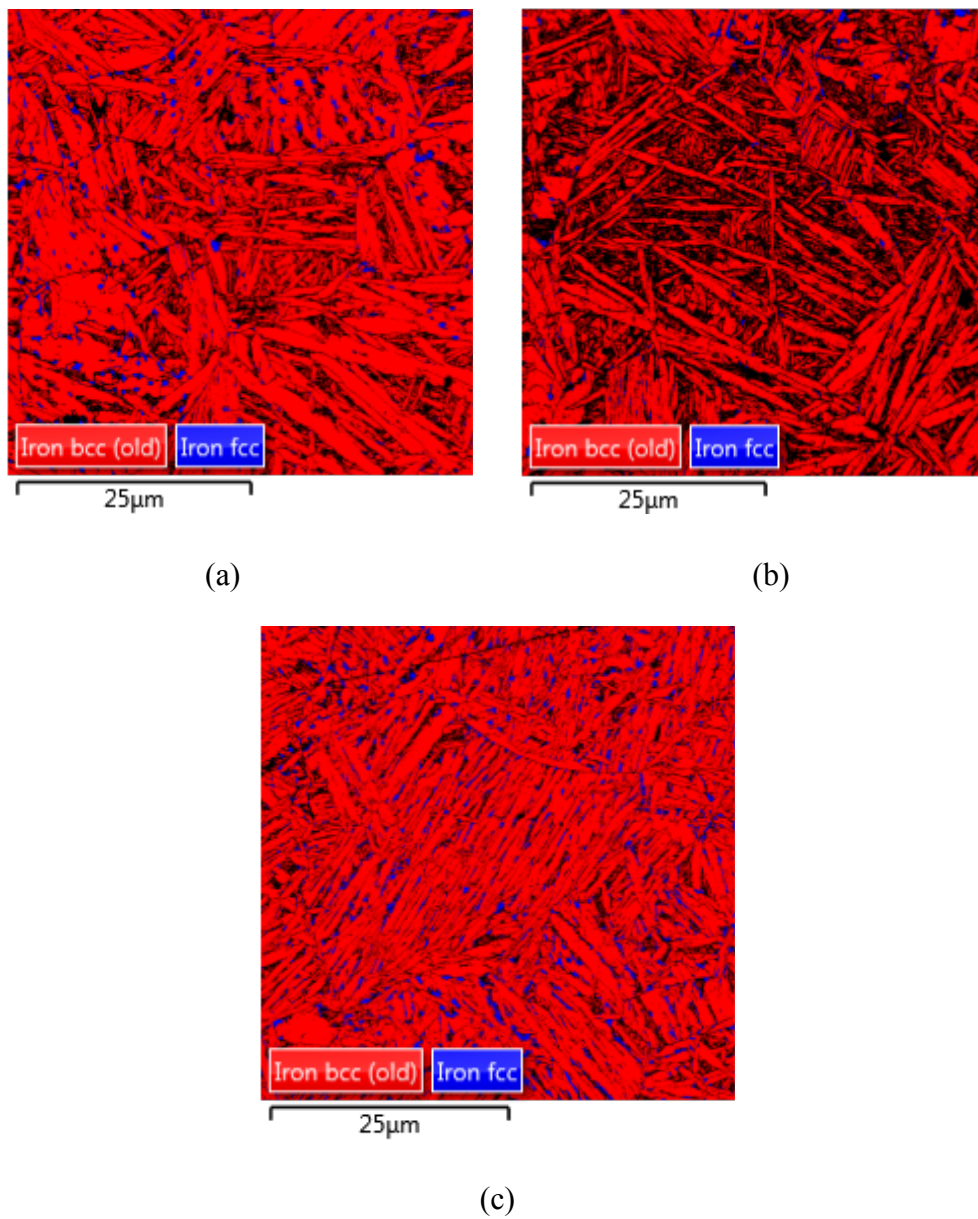


Figure 66 Phase map of the carbide free bainite (red, bainitic ferrite; blue, austenite) on (a) the non-ausformed specimen under bainite transformation for 60 minutes; (b) the specimen ausformed (10% strain) in tension before bainite transformation for 30 minutes; (c) the specimen ausformed (20% strain) in tension before bainite transformation for 60 minutes at 300°C.

#### 4.3.1.1 Morphology of ausformed carbide-free bainitic steel

The lath thickness of the bainitic ferrite was measured manually using line intercept method from the micrographs taken by EBSD on specimens shown in Figure 65 and Figure 66. The measured results are shown in the graph below (Figure 67) with the error bar representing the standard deviation from the mean value.

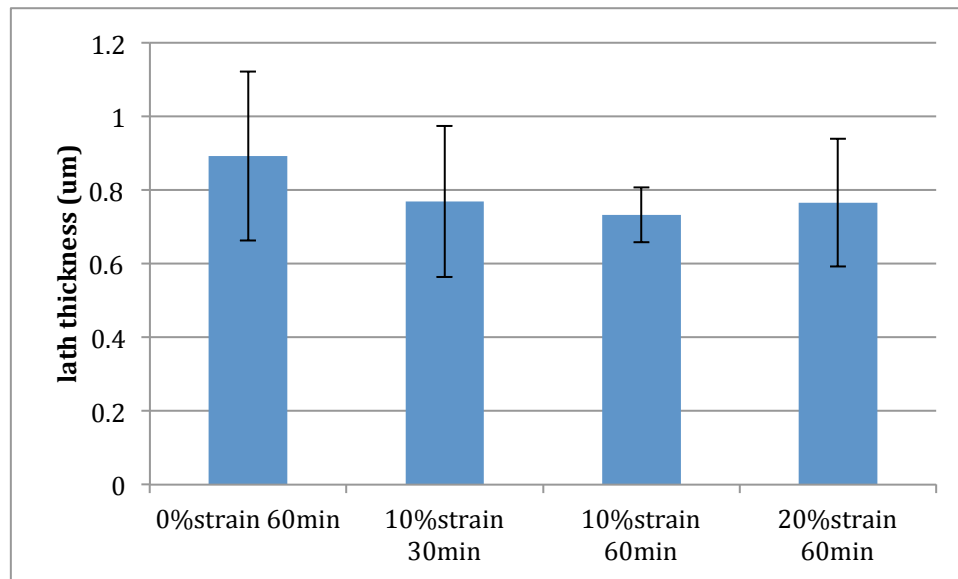
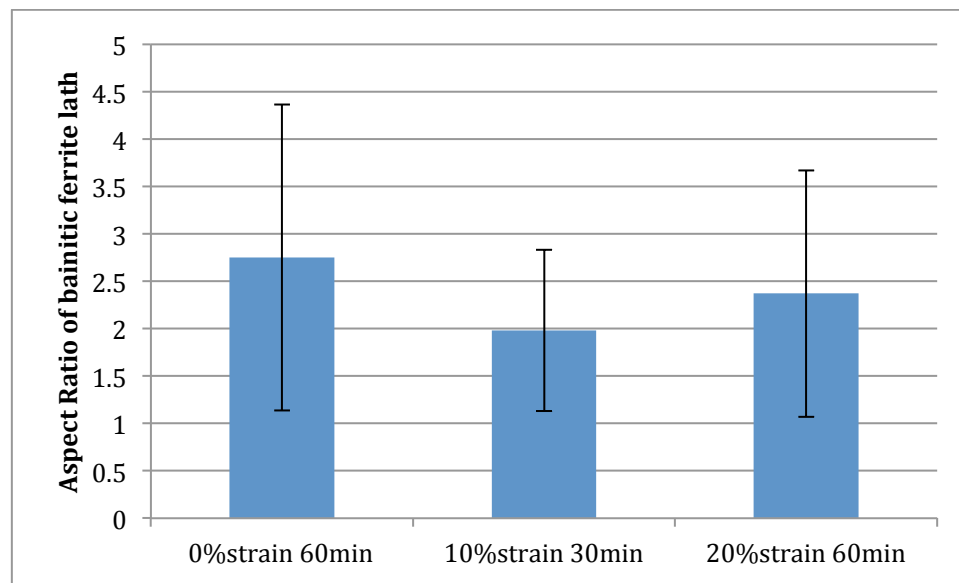


Figure 67 bainitic ferrite lath thickness for specimens after ausforming by 10% and 20% pre-strain followed by isothermal bainite heat treatment at 300°C for 30 or 60 minutes compared to the non-ausformed specimen with same bainite heat treatment

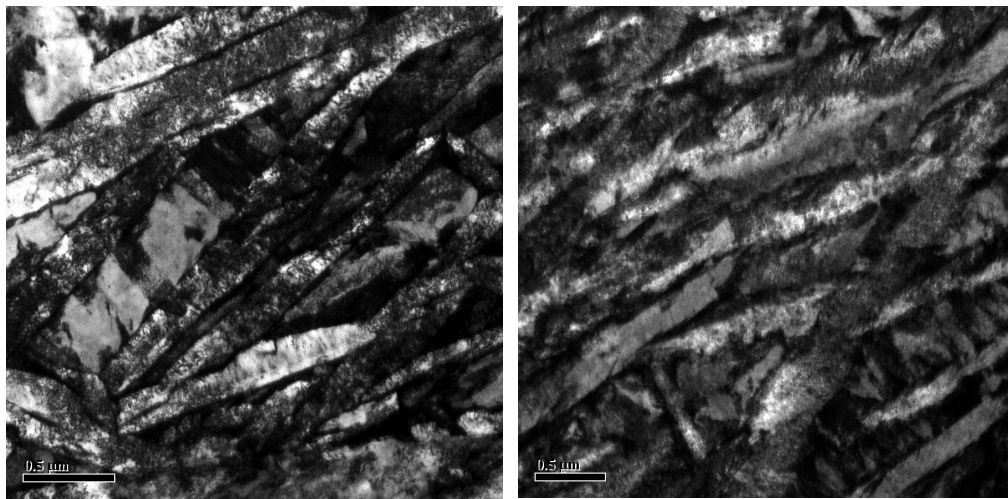
Moreover, the value of aspect ratio of the bainitic ferrite was measured by the line intercept method using Chanel 5 HKL software and reported in Figure 68. The lath grain is determined by the low-angle boundaries with a misorientation of 1 to 2 degree and the error bars represent the standard deviations from the average values. The aspect ratio of the detected bainitic ferrite grains after ausformation is slightly lower than that of the non-ausformed ones. Both the thickness and length of the bainitic ferrite laths are not affected significantly by plastic deformation of the austenite.



**Figure 68 Aspect ratio (length/thickness) of bainitic ferrite of the ausformed carbide free bainitic steel**

The dislocation substructure introduced to the microstructure during plastic deformation of the parent austenite phase can be detected by TEM. Figure 69 presents the TEM micrographs with high magnifications on specimens after plastic compression by 10% or 25% strain followed by isothermal bainite heat treatments. The dark tangled dislocation

lines are observed both in retained austenite and in bainitic ferrite/martensite. The TEM micrographs with higher magnifications have detected these dislocation structures (dark tangled lines) shown in Figure 70. The bright regions in the TEM micrographs are bainitic ferrite/martensite and the dark ones are austenite confirmed by the SAD patterns scanned on those corresponding regions. (Figure 71)



(a)

(b)

**Figure 69 TEM micrographs of specimens after ausformation (a) 10% prior compression followed by isothermal heat treatment at 300°C for 30 minutes and (b) 25% prior compression followed by isothermal treated at 300°C for 1 hour [191]**

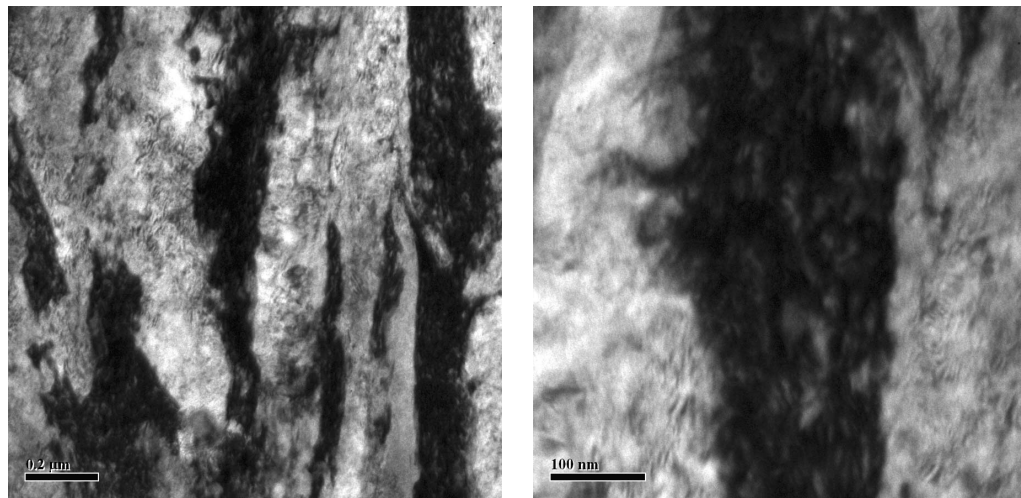
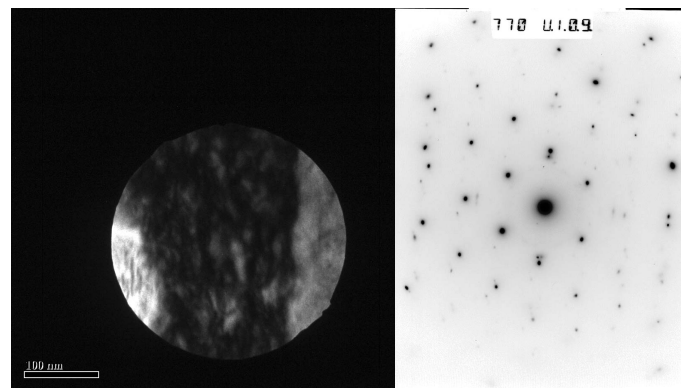
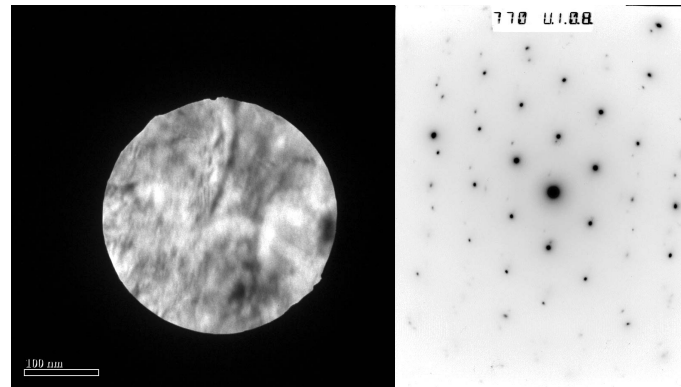


**Figure 70 TEM micrographs in high magnifications showing great dislocation density in the ausformed specimen (25% prior compression followed by isothermal treated at 300°C for 1 hour) [191]**



(a)



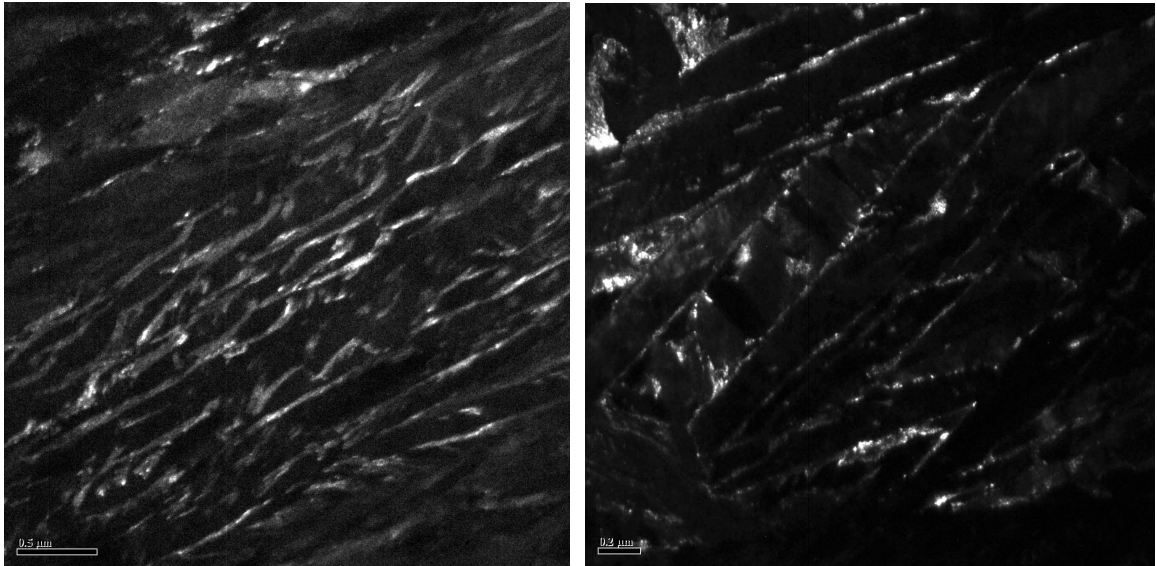
(b)

**Figure 71 TEM images (left image) and corresponding SAD patterns (right image) for (a) dark area with SAD pattern showing fcc lattice structure (austenite) and (b) bright area with SAD pattern showing bcc lattice structure (bainitic ferrite or martensite) [191]**

The dislocation substructures or debris are introduced during the ausforming process. Dislocations introduce more potential nucleation sites for bainitic ferrite. After ausformation, the nucleation sites of bainitic ferrite lath are not only at the prior austenite grain boundaries, but also at the inside of parent grains. Those additional nucleation sites within grain are induced by dislocations formed by the plastic deformation of the austenite. Even though the number of nucleation is improved by ausformation, the final volume fraction of bainitic ferrite is not increased. The growth of each nucleus may stop in an earlier stage due to the interactions of neighbouring platelets. The growth of the bainitic ferrite lath may also be hindered by the accumulated dislocation debris in the parent austenite to cause the early cessation of the bainite transformation. This is also

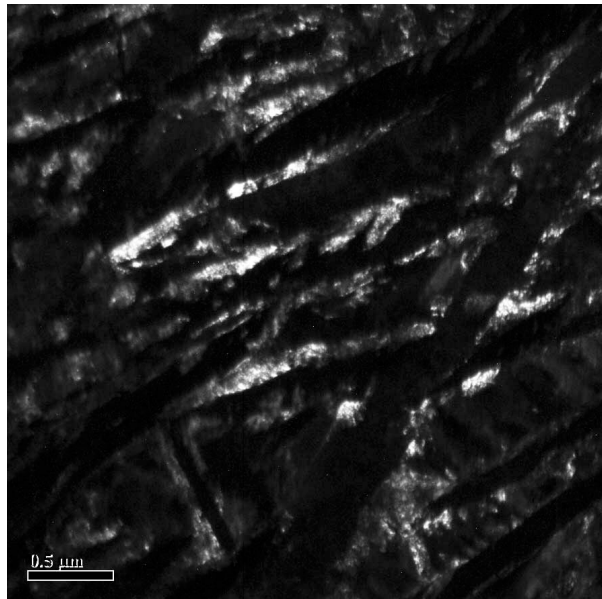
referred as mechanical stabilization of austenite. [151] Each ausformed bainitic lath is taking a smaller volume when the transformation is finished. The change in nucleation and growth kinetics by ausforming agrees with the dilatation measurements by Xu et al [187]. The initial transformation may speed up by ausforming due to more nucleation introduced into the microstructure. On the other hand, the bainite transformation may finished at shorter period, because the growth of bainite lath is hindered by dislocations debris or neighbouring laths growing from the inside of the austenite grain.

Meanwhile, greater amount of blocky residual austenite is maintained at room temperature in the final product. According to the EBSD analysis, the morphology of the retained austenite indicates that more blocky austenite is stabilized at room temperature by ausforming of 20% of strain than that in the unausformed material as illustrated in Figure 66 (a) and (c). The retained austenite in thin film has a thickness of 20-40nm, which is smaller than the step size of the EBSD scan. Thus the retained austenite film could not be detected by EBSD. TEM, on the other hand, were used to observe the distribution and size changes of the retained austenite in thin film after the specimen were ausformed. The Figure 72 presents the dark field (DF) images taken from an austenite reflection to highlight the retained austenite films (bright regions) inside the bainitic ferrite sheaves. The TEM images in Figure 72 were taken on the specimens after ausforming in different strain levels in compression in same magnification.



(a)

(b)



(c)

Figure 72 DF images taken from an austenite reflection of specimen with or without ausformation followed by isothermal bainite treatment at 300°C for 30 minutes (a) without ausforming, (b) ausformed in compression by 10%, (c) ausformed in compression by 25% [191]



There is a clear trend that the retained austenite films become coarser with the increment in plastic ausformation strain. The increase amount of blocky austenite and coarser austenite films are all consistent with the argument that the austenite is mechanical stabilized by plastic deformation. As discussed previously, the blocky retained austenite has a greater tendency to transform to martensite during deformation due to its lower carbon content compared to the retained austenite in thin films. The volume fraction and morphology change of the retained austenite after ausforming could influence the mechanical properties, especially the work hardening behavior of the carbide free bainitic steel.

Moreover, variant selection is found in the ausformed carbide free bainitic steel. Previous research on the carbide free bainitic steel shows that the orientation relationship between bainitic ferrite and austenite closely follows the classical Kurdjumov-Sachs (K-S) relationship and the Nishiyama-Wasserman (N-W) relationship. [73, 74] This may not be the case for the ausformed bainitic steel. The orientation map of the ausformed specimen (20% of strain followed by 60 minutes at 300°C) is shown in Figure 73, in which each orientation of the bainitic ferrite lath is represented by a different color. There are two types of bainitic lath structures noted in the EBSD micrograph. The type A bainitic laths are long and aligned along one direction in the austenite grain. The type B laths are shorter and oriented in multiple directions. The type A bainitic laths mostly

nucleated from the austenite grain boundaries, while the type B laths also nucleate inside the austenite grain. Unlike type A ferrite lath, which is comparable to the morphology of non-ausformed bainite, the packet structure of parallel bainitic ferrite laths is not observed in the type B. Instead, the bainitic laths in type B are oriented in high angles (45-90 degree) with the adjacent laths. This is in agreement with Chiou *et al.* and Larn *et al* studied claiming that plastic deformation of the parent austenite phase hinders the formation of sheaf-like parallel plates of bainitic ferrite. [152, 153] The bainite sheave structure that is dominant in the specimens without ausforming (shown in the TEM micrographs in Figure 72(a)) is much less observed on the specimens with 10% and 25% of ausforming strain (Figure 72(b) and (c)). The interlocking structure of the type B of bainite lath agrees with the observation by the TEM image of the ausformed specimen in Figure 74 at higher magnifications.

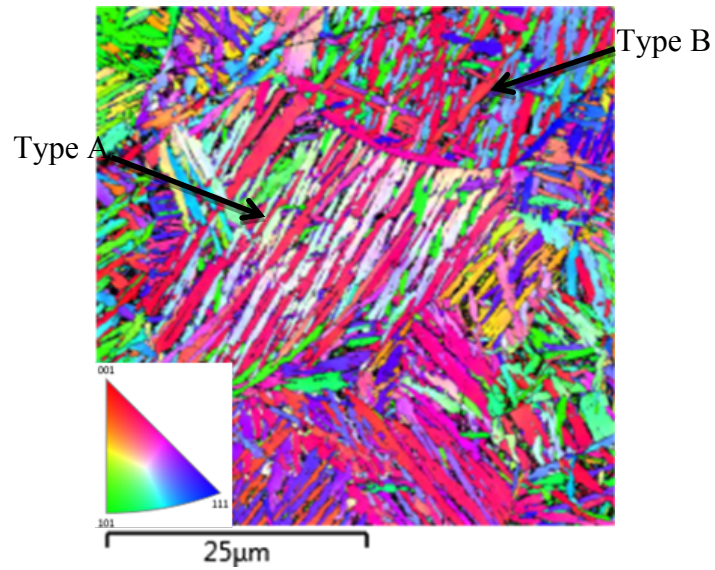


Figure 73 EBSD orientation map of the specimen (20% of strain followed by 60 minutes at 300°C)

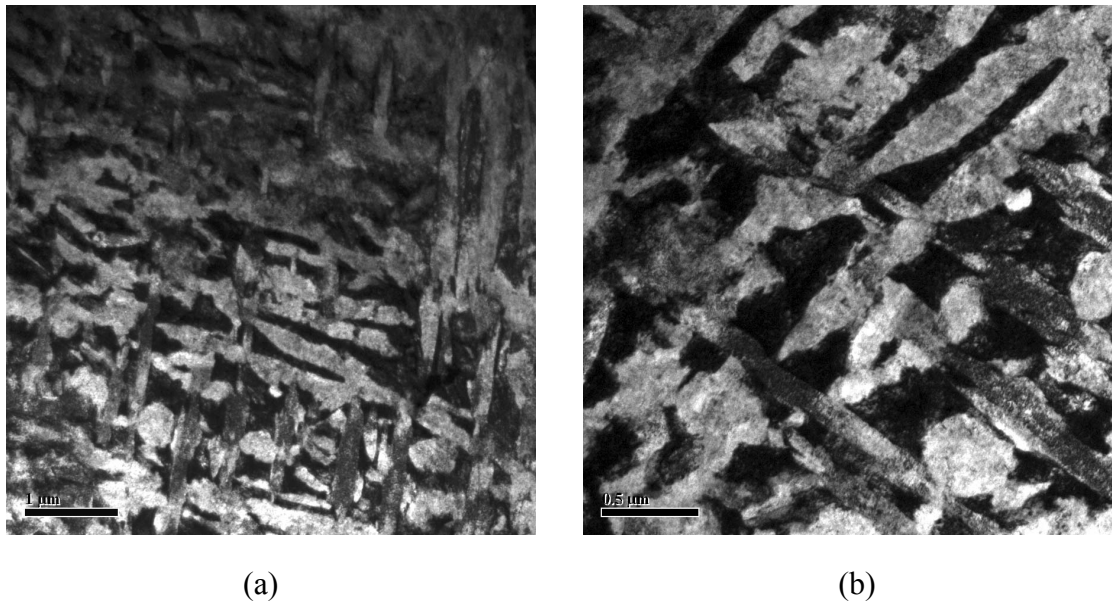
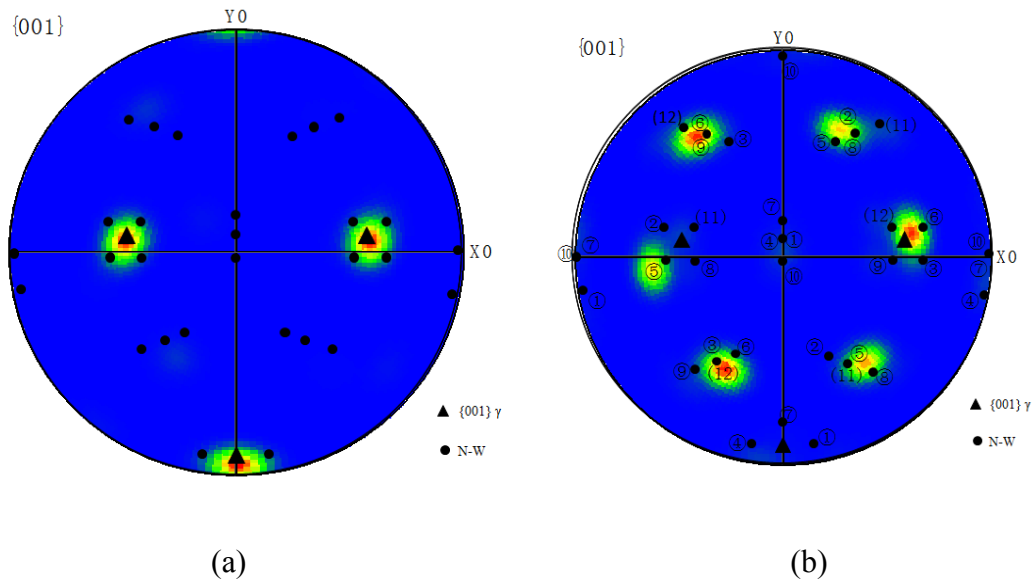
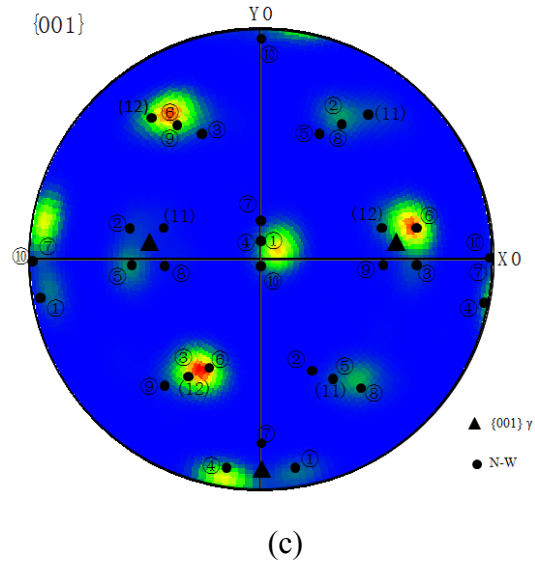


Figure 74 The interlocking structure of austenite (dark region) and ferrite (bright region) mixture in specimen with prior compression by 25% at 300°C and then isothermal transformation at 300°C for 1 hour [191]

Strong variant selection of bainitic ferrite is observed in the specimen after ausformed by

20% of strain, both in type A and type B (Figure 75). Even though, the ferrite and martensite could not be separated by EBSD, the volume fraction of martensite is negligible compared to that of bainitic ferrite. The pole figures are obtained mainly from the bainitic ferrite taken from the subsets within single prior austenite grains. 12 variants of the N-W relationship are plotted as well in the pole figure. The only variants appearing in the N-W relationship were V5, V6, V9 and V12 in type A, and the variants observed in type B were V4, V6, V10 and V12.





**Figure 75 Pole figures obtained from single austenite grain in ausformed specimen (20% pre-strain followed by 60 minutes at 300°C) of (a) austenite, (b) bainitic ferrite type A and (c) bainitic ferrite type B**

In contrast, variant selection hardly occurs for bainite transformation in the specimen ausformed by 10% of strain at 300°C. Figure 76 shows the  $\{001\}$  pole figure of retained austenite and the mixture of the bainitic ferrite and martensite taken from the carbide free bainite specimens under ausforming strain of 10% followed by 30 minutes of bainite transformation. Compared to the N-W variants, almost all the variants of bainitic ferrite are presented in the ausformed bainite under a pre-strain of 10% in the  $\{001\}$  bainitic ferrite pole figure (Figure 76(b)).

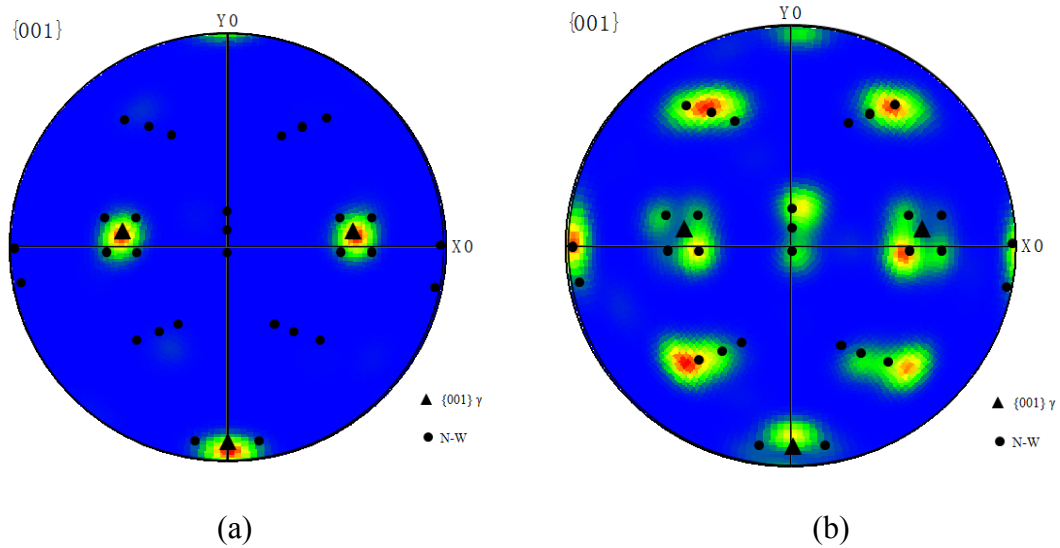


**Figure 76 Pole figures obtained from single austenite grain in ausformed bainite (pre-strain of 10% followed by isothermal heat treatment at 300°C for 30 minutes): (a) retained austenite and (b) bainitic ferrite**

Previously, researches noted that a deformation of the parent phase causes the change in orientation relationship of some product phases including Widmanstätten ferrite, bainite and martensite. [174] The variant selection of the ausformed bainite depends on the level of the strain during ausforming. Strong variant selection is observed on the specimen after ausforming by 20% of strain in tension, while the variant selection is weaker or negligible on the specimen after 10% of ausformation strain.

According to the optical micrographs in Figure 63, the orientation of the aligned ferrite laths is not directly related to the external applied stress direction during ausformation. Instead, the structure of the ausformed bainitic ferrite is very different among the individual austenite grains (type A and type B presented in Figure 73). The

heterogeneous residual stress distribution in deformed austenite parent phase may cause the change in structure of the ausformed bainitic ferrite.

The interaction between deformation and microstructure causes residual stresses. [174]

The slip systems and the corresponding Schmid factors are different from one grain to another in austenite. Each component yields under different levels of stress. The plastic strain distribution among each individual austenite grain is due to the different response to the applied deformation stress. The ausforming strain of 20% in tension may result in inhomogeneous plastic flow among the austenite grains. The microscopic residual stresses are induced in each austenite grain due to the plasticity incompatibility under ausforming procedure.

The residual stresses within microstructure also arise from phase transformation which involves shape change. Bainitic ferrite grows in the form of thin-plates or lath with a dilatational shape change and there is a shear process involved in bainite transformation. Consequently, if the parent phase is deformed plastically, the residual stresses as a consequence of the plastic strain distribution can be compensated by the shape change involved due to the product phase transformation. The residual stress in the parent phase modifies the crystallographic orientation of the product bainite phase. The change in orientations of bainite compensates the residual stresses caused by austenite deformation by minimizing the strain caused by plastic deformation of austenite. The

selection of certain variants during the bainite formation corresponds to the residual stresses within the individual austenite grains after ausforming. [192-194] Since the residual stress within one parent austenite grain favours certain variants relative to the others during bainite formation. A deformation of the parent phase may cause the change in orientation of bainite laths due to the induced residual stresses within each austenite grains.

### **4.3.2 Mechanical behavior and discussion**

The flat tensile specimens are re-machined after the Gleeble thermo-mechanical process to make sure the final microstructure is uniform along the gauge length (with the thickness of 1mm and width of 2mm) before testing in tension. The true stress vs. strain curves are plotted for specimens with 0% and 20% of ausforming strain followed by bainite isothermal heat treatment at 300°C for 60 minutes (Figure 77). The mechanical properties measured by the tensile tests are shown in the Table 8.

Both the ductility and fracture toughness of the carbide free bainitic steel are improved by the plastic deformation of the parent austenite phase. The uniform elongation (EI) is tripled and the true fracture strain (area reduction (RA)) is doubled by ausforming of 20% strain. Meanwhile, the ultimate tensile strength (UTS) is reduced by around 200MPa due to the ausformation.



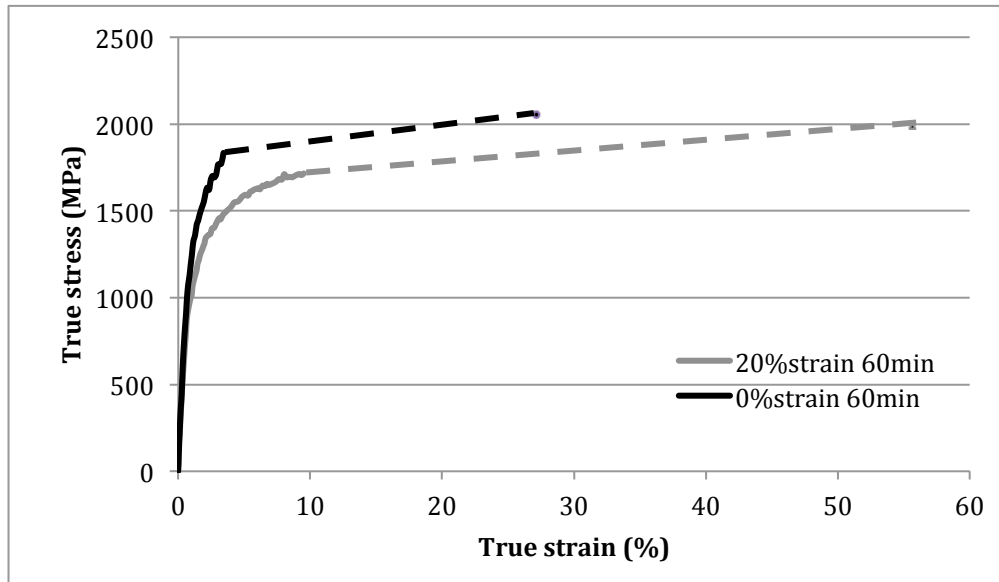


**Figure 77** The true stress vs. strain curves are plotted for specimens with 0% and 20% of ausforming strain followed by bainite isothermal heat treatment at 300°C for 60 minutes

**Table 8** Tensile and Fracture properties of CFB steel after 60min of bainite heat treatment with or without ausforming in tension by 20% in Gleeble

	YS (MPa)	UTS (MPa)	EI (%)	FS (MPa)	RA (%)
With ausforming	1051	1562	10.0	1993	55.7
Without ausforming	1014	1772	3.5	2054	27.15

For the bainitic steel after ausforming, the ultimate tensile strength decreases with a rise in uniform elongation. The reduction in the strength (UTS) and the improvement in ductility (EI) may be influenced by the change in the volume fraction of the bainitic

ferrite and the retained austenite after ausforming by 20% of strain. More blocky austenite grains with less strength than bainite and martensite are presented in the microstructure revealed by EBSD analysis. The change in strength and ductility may be due to the replacement of martensite by softer retained austenite in the ausformed carbide free bainitic steel.

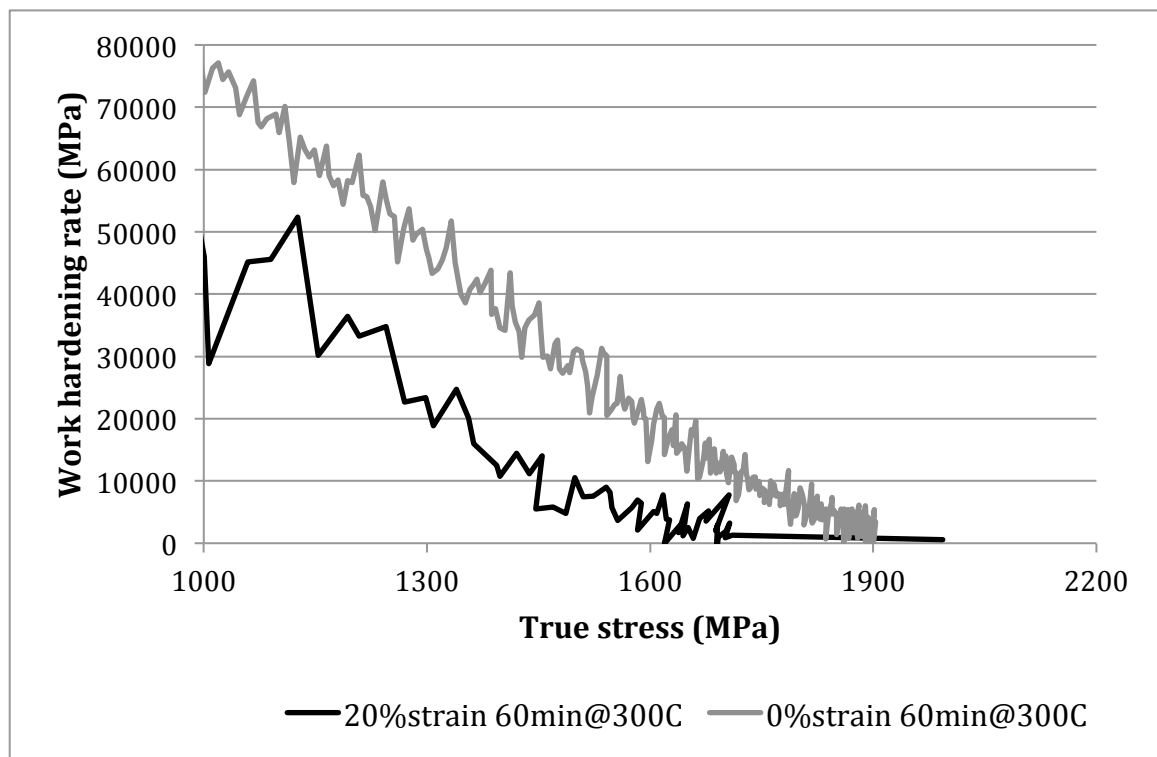


**Figure 78 Work-hardening rate of the specimen after 60 minutes of isothermal heat treatment with 0 and 20% strain of ausforming by Gleeble**

The work hardening rate curve of the specimen with ausforming by 20% of strain in Figure 78 flattens at stress level higher than 1400MPa before it meets the Considere criterion to cause necking. The existence of retained austenite revealed by EBSD may

cause the TRIP effect accompanying the elasto-plastic transition of the ausformed carbide free bainitic steel. Since these granular austenite grains are less stable compared to the austenite in the form of thin film, TRIP effect may occur during the plastic deformation stage of the material before the onset of necking. The TRIP effect that may occur during work hardening contributes further to the ductility and toughness of the ausformed material.

To summarize, the factors that may impact the work hardening behaviour of the ausformed bainitic steel include the volume fraction change in main phases and the TRIP effect.

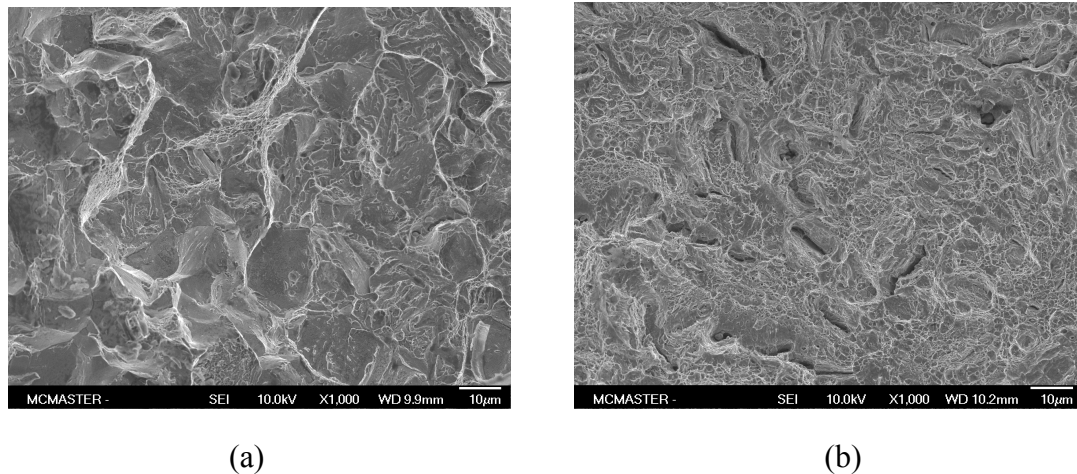


**Figure 79 Fracture surface of the specimens transformed at 573K(300°C) for 60 minutes by Gleeble with deformation of (a) 0% strain and (b) 20% strain in tension**

The fracture surface is examined by SEM on the specimens with 0% and 20% strain of ausforming after tensile test, as shown in Figure 79. The martensite and bainitic ferrite

is replaced partially by the softer retained austenite in the final microstructure of the ausformed material. The fracture surface of the specimen after 20% of pre-strain during ausforming (Figure 79(b)) is mainly covered by dimples. It is dominated by a ductile mechanism caused by void link-up and coalescence after ausforming by the Gleeble process. Moreover, the retained austenite at the tip of a crack where the local stress is concentrated may be induced to shear to form martensite. This TRIP effect that costs extra energy during fracture is beneficial in postponing the crack propagation. It results in higher fracture resistance. As a result, the area reduction as the true fracture strain is doubled from 27% to 55.7% by austenite deformation in tension by a strain of 20%.

## **4.4 Ausforming by rolling**

Another set of experiments were conducted to ausform the material by rolling at 300°C. This thermo-mechanical procedure was designed to simulate the rolling procedure in steel production in order to make ausformed carbide free bainitic steel in the industrial scale. Rectangular specimens with a dimension of 10x1x1cm were heated at 1133K(860°C) for 15 minutes, followed by air cooling and rolling to the equivalent strain of 0.13 at 623K(350°C). The specimen was then transferred to a 573K(300°C) furnace, held for 90mins, and water quenched to room temperature as described in Chapter 2. This thermo-mechanical procedure reproduced a similar result to the ausforming by Gleeble thermo-mechanical simulator. Flat samples were machined from the center of the

thermo-mechanically treated block to avoid thermal variation between the surface and the center of the block and possible oxidation during the heat treatment.

#### **4.4.1 Microstructure**

The microstructure of the carbide free bainitic steel after the thermo-mechanical process by rolling at 300°C is observed by optical microscope after etching (solution of 40g NaOH, 60g H<sub>2</sub>O and 15g NaNO at 100°C for 1 minute). The optical micrographs of the material under the same bainite heat treatment with or without ausforming is presented in Figure 80. The bainite volume fraction is decreased tremendously after rolling by equivalent strain of 0.13. The effect in maximum bainite volume fraction agrees with previous research results after ausforming in compression. Moreover, the bainitic ferrite laths are shortened after compressive deformation of the parent austenite, and the thickness of each ferrite lath is reduced as well. Further characterization of the microstructure in higher magnification by SEM and EBSD are performed to resolve more details of each phase.

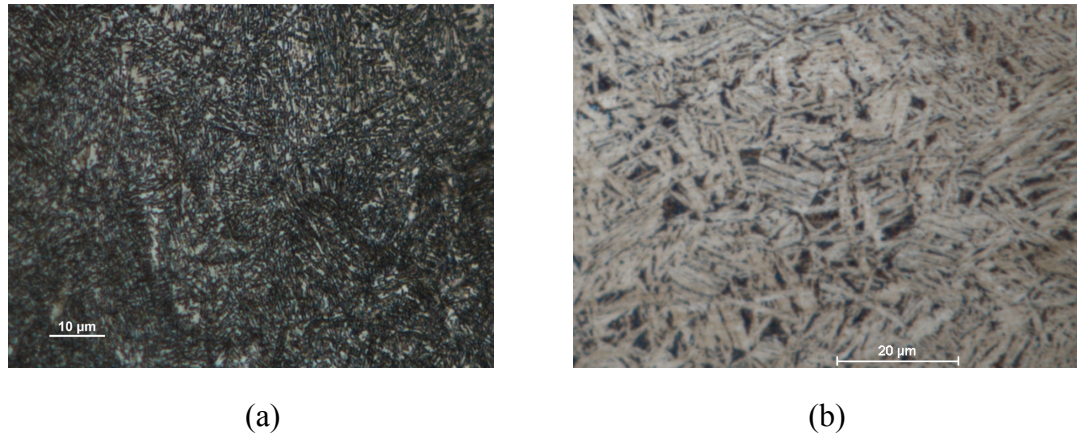


**Figure 80 Optical micrographic images for carbide free bainitic steel after bainite transformation at 300°C for 90 minutes (a) after ausforming by rolling at 350°C and (b) without ausforming. Bainite: bright phase; martensite/austenite: dark phase.**

The microstructure of the specimen after rolling is characterized by SEM after etching by Nital 2% solution and the results are shown in the Figure 81 below. The darker region is the bainitic ferrite and the brighter region is either martensite or austenite in the SEM micrographs.

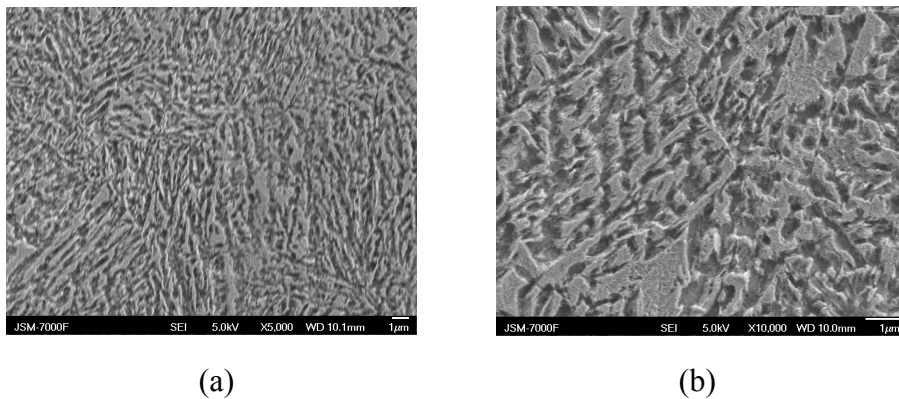
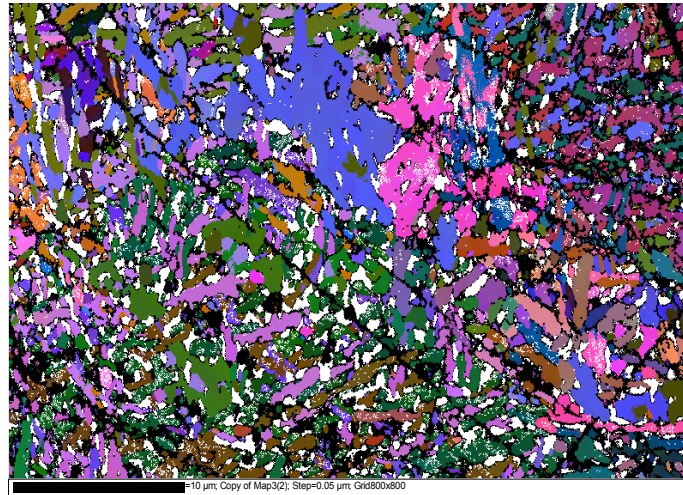


**Figure 81 SEM images for transformed product after ausforming by rolling at 350°C in (a) lower and (b) higher magnifications. Darker region: bainitic ferrite; Brighter region: martensite/austenite.**

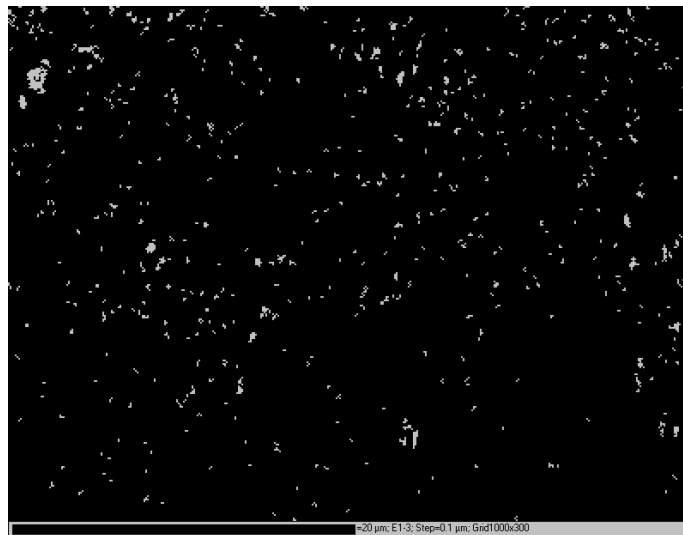
In order to distinguish the retained austenite from the martensite phase, the EBSD analysis is carried out as well (Figure 82(a)). Based on the EBSD microstructure characterization, there is a relatively high amount of retained austenite in granular or blocky shape. The blocky retained austenite is less stable under deformation than the austenite in thin film between bainitic ferrite lathes. As a result, the rolled specimen may show TRIP effect during plastic deformation under tensile test to improve the work hardening of the carbide free bainitic steel.

As shown in the EBSD analysis result (Figure 82(a)), a large amount of blocky austenite (15-20% volume fraction) is retained at room temperature after the rolling and isothermal heating process. The volume fraction of retained austenite is doubled after ausforming compared to that in the same material after 90mins without ausforming. The increased amount of blocky retained austenite can be explained by the mechanical stabilization of the austenite by ausforming. Since it has been proven that both the bainite start temperature ( $B_s$ ) and martensite start temperature ( $M_s$ ) are reduced after ausforming, there is a justified greater amount of austenite stabilized at room temperature. [21, 150, 188] The change in volume fraction of austenite is accompanied by the change of carbon content of the residual austenite phase. The increase of volume fraction of austenite is correlated with the decreasing carbon content of the retained austenite. Due to the negligible carbon solubility in ferrite, the majority of the carbon in the material has been

diffused into austenite in the carbide free bainite. As a result, the carbon content of austenite in the rolled material is lower than the non-ausformed one.



(a)



(b)

**Figure 82 EBSD micrographs of the carbide free bainite microstructure with ausforming by rolling at 350°C with austenite in white. (a) before the tensile test and (b) after the tensile test.**

The stability of retained austenite is greatly influenced by its carbon content; austenite is



less stable under deformation in the ausformed steel. The EBSD analysis on the same specimen after uniaxial tensile test shown in Figure 82(b) confirms that the volume fraction of retained austenite is decreased from 15-20% to ~2.5% after the specimen is pulled to fracture.

#### **4.4.2 Mechanical behavior and discussion**

The machined flat tensile specimen after rolling followed by bainite isothermal heat treatment are tested in tension with a cross-head speed of 1 mm/min. The engineering stress vs. strain curve is plotted in Figure 83 below, and the mechanical properties are measured and reported in the Table 9 in comparison to the specimen under the same bainite heat treatment without ausforming.

After rolling at 350°C by the equivalent strain of 0.13, the yield strength is increased by approximately 90MPa. The yield strength is improved since the bainite grain size is refined by rolling, as shown in the optical micrographs. The ultimate tensile strength (UTS) is lowered after rolling since the volume fraction of retained austenite as the softest phase is doubled, compared to the carbide free bainite without austenite deformation. The stress vs. strain curve of the ausformed steel is deviated from the one of the material without ausforming at stress higher than 1200MPa. The ausformed specimen reaches to greater uniform elongation due to the induced transformation of martensite from austenite (TRIP effect) under stresses greater than 1200MPa.

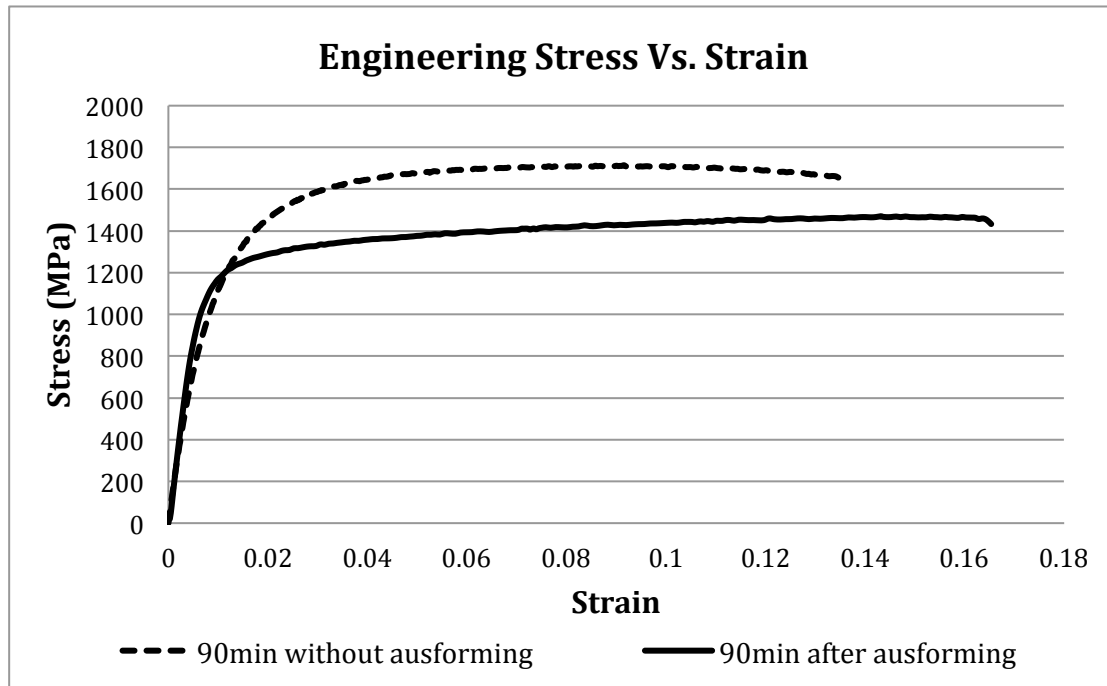


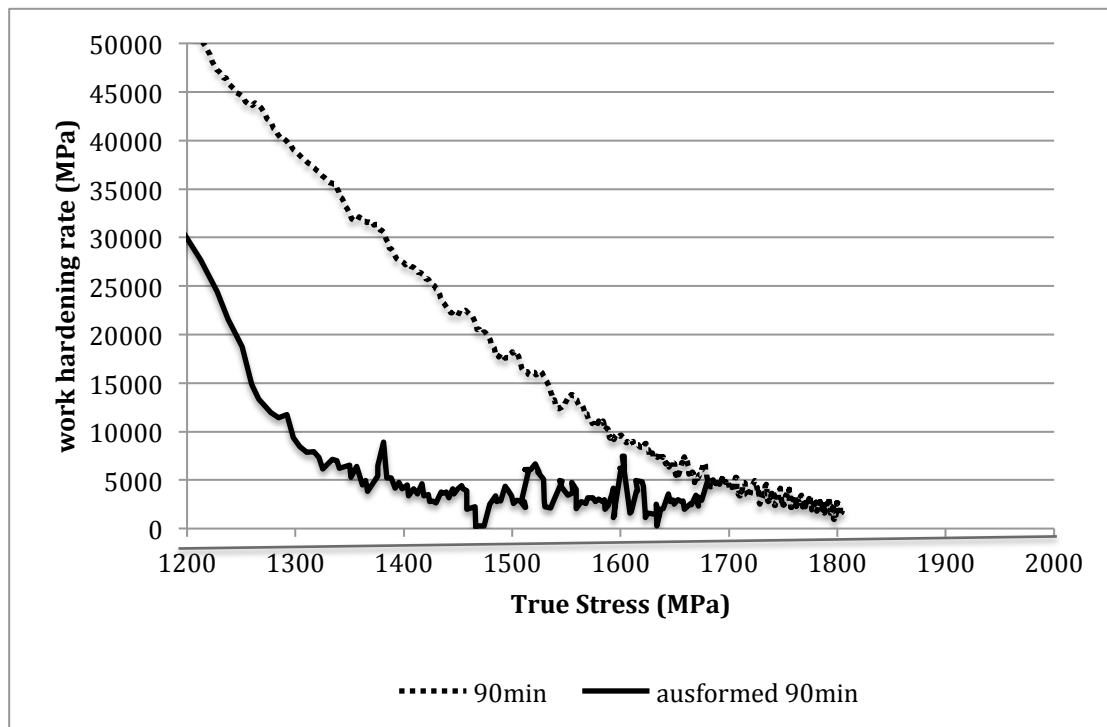
Figure 83 engineering stress-strain curves of the specimens heated at 300°C for 90 minutes with and without ausforming by rolling

Table 9 Tensile and Fracture properties of CFB steel after 90min of bainite heat treatment with or without rolling

	YS (MPa)	UTS (MPa)	EI (%)	FS (MPa)	RA (%)
With rolling	1041	1470	14.3	2945	27.2
Without rolling	953	1715	9.2	2100	21.2

The work hardening rate is plotted against the true stress for both the bainitic steel after 90 minutes of isothermal heat treatment with or without rolling. Similar to the 90min sample without a rolling process, the gradual yielding, or extensive elasto-plastic

transition, is still contributing to the high work hardening behavior for material after rolling. However, this transition stage in the ausformed specimen is complete at true stress below 1300MPa, while the elasto-plastic transition is dominant in the non-ausformed specimen at stress below 1700MPa. At true stress higher than 1300MPa, the slope of the work hardening rate curve of the ausformed specimen starts to flatten and fluctuate with an increase of true stress.



**Figure 84 Work-hardening rate of the specimen after 90 minutes of isothermal heat treatment with and without ausforming by rolling**

This different work hardening behavior suggests that other than the kinematic work hardening that was discussed in Chapter 3, the TRIP effect may also contribute to the

work hardening. The fluctuation of the work hardening rate vs. true stress plot during the gradual yielding stage occurs especially under stress to the rolled bainitic steel above 1300MPa. The change in volume fraction of retained austenite shown by EBSD analysis (Figure 82) before and after the tensile test corresponds to the TRIP effect. An austenite volume fraction of 15-20% is retained at room temperature with much lower carbon content and blockier morphology. The volume fraction of retained austenite is reduced from 15-20% before deformation in tension to ~2.5% after tensile testing. The transformation from austenite to martensite might occur during the work hardening stage of deformation to further delay the onset of necking.

The TRIP effect was not a significant factor in the work hardening behaviour of the carbide free bainitic steel with normal heat treatment procedure as discussed in Chapter 3, since the retained austenite is too stable to transform before the onset of necking. In the case of the ausformed carbide free bainitic steel, the TRIP effect might be more influential on the work hardening behavior. As shown in the work hardening rate plot in Figure 84, the solid line representing the work hardening rate of the rolled bainitic steel fluctuates before reaching the Considere criterion. The fluctuation is caused by the TRIP effect since the soft austenite is replaced by martensite with higher strength. Thus, the retained austenite is mostly transformed to martensite during plastic deformation and contributes to the improvement of work hardening. The transformation from austenite

to martensite might occur during the work hardening stage of deformation to further delay the onset of necking.

The blocky morphology of the retained austenite in the rolled carbide free bainitic steel also influences its fracture behavior. The fracture properties and the fracture surface micrographs are shown in Table 10 and Figure 85 respectively, comparing the specimen after bainite heat treatment at 300°C for 90 minutes with that and without rolling.

**Table 10 Fracture properties at room temperature of the specimens after 90 minutes of isothermal bainite transformation treatment with and without ausforming by rolling**

Isothermal heat treatment at 300°C for 90 minutes	FS (MPa)	RA (%)
With ausforming	2945	27
Without ausforming	2100	21.2

FS is the true Fracture stress; RA is the reduction of area

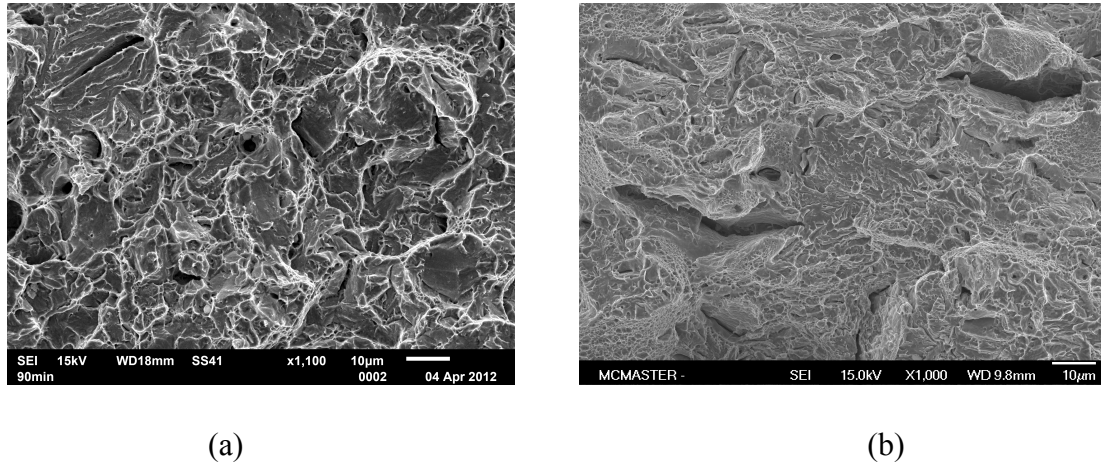


**Figure 85 SEM image on the fracture surface topography on the specimen after bainite heat treatment at 300°C for 90min (a) without ausforming and (b) with ausforming**

As discussed in the previous chapter, the appearance of some cleavage facets with feather patterns accompanied by adjacent dimpled areas are shown on the fractograph of the specimen after 300°C for 90 min without ausforming (Figure 85(a)). Additional information provided by microstructural examinations illustrates that the non-ausformed specimen is mainly composed of carbide-free ductile bainite as the matrix, and granular martensite as the brittle second phase. Intergranular fracture or cleavage may occur in the brittle martensite-rich region. As the volume fraction of the relatively carbide free bainite increases, the material is more ductile that may fail by microvoids link-up instead. These are characterized by dimples covering the fracture surface.

By rolling the specimen, more parent austenite is retained at room temperature instead of transformation to martensite. As revealed by the EBSD analysis, the fracture surface is

composed of fibrous features with fine dimples, representing ductile fracture caused by void coalescence without any obvious cleavage facets observed. More austenite is retained at room temperature, the average carbon content of the austenite is lower than that in same steel without ausforming. At the same time, the austenite is presented in the blocky morphology instead of in thin film shape sandwiched by the bainitic ferrite lath. Therefore, it is reasonable to suggest that the carbon-enriched retained austenite is softer in the ausformed specimen. The reduction in hardness as well as the increment in the volume fraction of austenite make the material more ductile.

The existence of a larger amount of soft retained austenite with the potential to cause TRIP effect contributes to the increase of both the fracture strength and area reduction (true fracture strain) as shown in Table 10. As a result, ausforming at 350°C just before bainite transformation caused by rolling improves both the strength and toughness by stabilizing more austenite at room temperature. The fracture surface of the specimen ausformed by Gleeble is observed by SEM as shown in Figure 79 is comparable to that of the specimen ausformed by rolling shown in Figure 85.

## **5 New material design**

The aim of the work presented and discussed in chapters 3 and 4 was to establish the nature of the relationship between the mechanical properties and the microstructure of carbide free bainitic steel. All those experimental results are based on the 0.4C-2.8Mn-2Si (wt%) steel. However, this steel grade cannot be applied to industry for commercial uses, because its carbon content is over the upper limit for acceptable weldability and its flangeability is inconsistent (based on hole expansion test) mainly due to its heterogeneous microstructure (banding structure). These problems are addressed by a new set of steel chemistries. The weldability of the newly designed alloy is improved by reducing the overall carbon content. By modifying the substitutional alloying elements in the material, the alloy element segregation is reduced while maintaining good hardenability.

### **5.1 Carbon content**

With carbon content low enough, the bainite will form in the heat-affected zone replacing the brittle martensite phase. The welded part after the heating cycle is more resistance to crack initiation and propagation, resulting from the reduction in hydrogen embrittlement and transformation stresses. [41] Furthermore, by reducing the carbon content of the alloy, the maximum volume fraction of bainitic ferrite is increased, and both the ductility and



toughness of the material improve as well.

The cutback in carbon content also tends to decrease both the yield strength and ultimate tensile strength, since it gives coarser bainitic ferrite structure as well as the reduction in solid solution hardening contribution. As shown in the summary of the previous work generated in the diagram (Figure 86), there is a linear relationship between the carbon content and the tensile strength of the carbide free bainitic steel, regardless of the heat treatment procedure details.

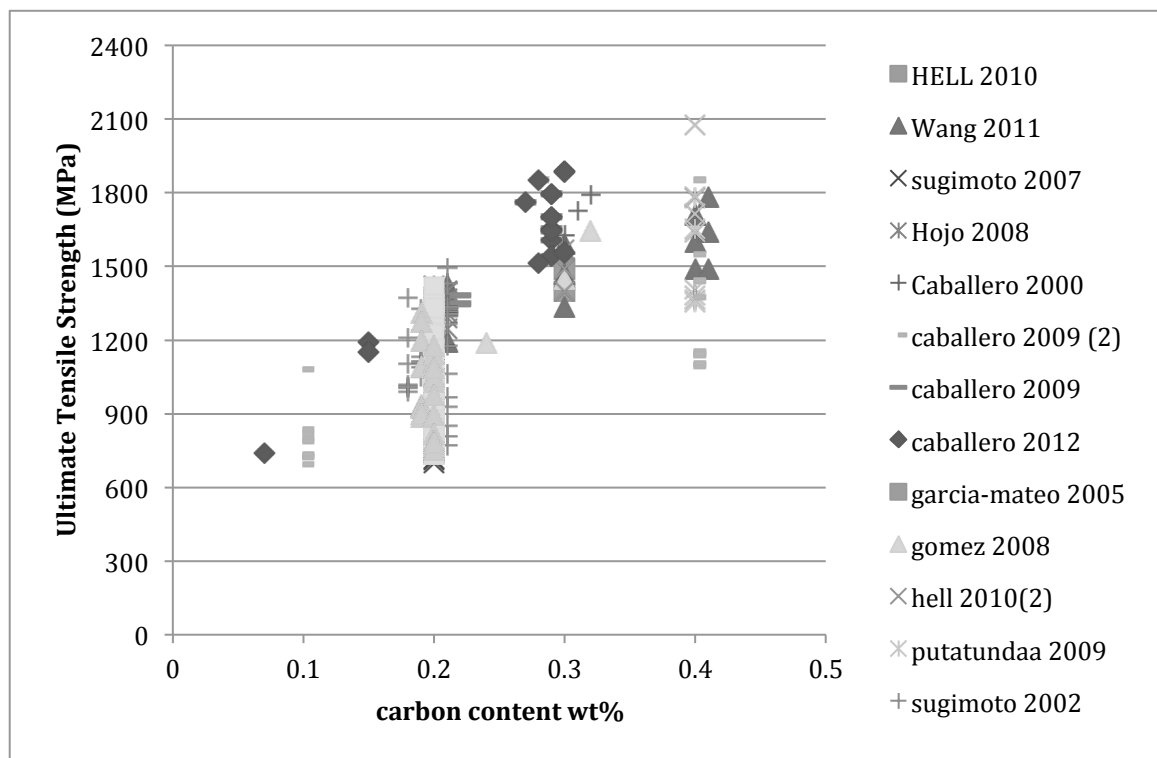


**Figure 86 A summary of the ultimate tensile strength of carbide free bainitic steel with different carbon content.**

Thus, the carbon content should be set to reach the maximum limit for acceptable weldability in order to achieve the highest possible strength of the steel alloy. It is

suggested that with carbon content lower than 0.3wt% and the addition of substitutional alloy elements including Mn, Ni or Cr, the steel is readily weldable. [41] The carbon content of the new chemistry of the carbide free bainitic steel is reduced to be 0.3wt%.

## **5.2 Alloying Elements**

The motivation of addition of substitutional alloying elements in the first place is to replace some Mn content in the material, which is the leading cause of the banding structure due to its segregation throughout the microstructure. Alloying elements such as Cr, Mo, Ni and B are all considered as great candidates to partially replace Mn, as they contribute to the hardenability of the material.

The addition of Cr is suggested for two main reasons. First, it prohibits polygonal ferrite formation during cooling from austenite and forms lamellar bainitic matrix instead. [2] Second, it will help to depress the  $M_s$  temperature, allowing lower bainite transformation temperature for finer structure. [18]. Moreover, chromium also reduces graphitization while exposed at an elevated temperature for a prolonged period of time. [18]

Boron suppresses the pearlite and proeutectoid ferrite [77] by segregation at the prior austenite grain boundaries to delay their nucleation. However, the boron segregation is also not preferred for bainitic ferrite nucleation as it postpones and slows down the bainite transformation. [21] Therefore, boron is not selected as one of the alloy elements in the chemistry designed for new carbide free bainite.

Cobalt is added to the design of the new bainitic steel in order to accelerate the bainite transformation. The increased rate of bainite reaction is a consequence mainly of the increase in the free energy difference between the ferrite and austenite phases. [11]

At least 1.5wt% of Si is added, as mentioned previously, to avoid carbide precipitation during isothermal bainite transformation. Moreover, it is possible to increase the retained austenite volume fraction with extra silicon introduced to the material. [115]

### **5.3 Chemistry design**

The present aim is to use the background information described above to design a set of materials with new chemistry that can achieve excellent and consistent mechanical properties with good hardenability and acceptable weldability. Following a series of investigations based on background knowledge from previous works, Thermo-Cal is applied to calculate the segregation ratio of each element during solidification and phase diagrams are computed to guide the design process.

The compositions of eight new alloys are proposed following a series of theoretical investigations and are shown in the Table 11. The base alloy system Fe-0.3C-(1.5-2.5)Si-(1-3)Mn (wt%) is proposed. Addition of 1.5wt% of Ni and Cr are introduced to alloy #3, 6, 7, 8 and #4, 6, 8 respectively to reduce the manganese amount in the material. An addition of 0.8wt% Co is introduced to partially replace the Mn content in alloy #5 and 8. The silicon content is increased from 1.5 to 2.5wt% in alloy

#2 to investigate how the extra Si amount would affect the final microstructure and properties.

**Table 11 Chemical composition of the new alloys**

<b>Alloy</b>	<b>C wt%</b>	<b>Si wt%</b>	<b>Mn wt%</b>	<b>Ni wt%</b>	<b>Cr wt%</b>	<b>Co wt%</b>
#1	0.3	1.5	3	0	0	0
#2	0.3	2.5	3	0	0	0
#3	0.3	1.5	1.5	1.5	0	0
#4	0.3	1.5	1.5	0	1.5	0
#5	0.3	1.5	1.5	0	0	0.8
#6	0.3	1.5	1.5	1.5	1.5	0
#7	0.3	1.5	1.5	1.5	0	0.8
#8	0.3	1.5	1.5	1.5	1.5	0.8

All these alloys were casted by arc-melting, hot-rolled and homogenized before being analyzed by a dilatometer. All the alloys are heated above  $A_{c3}$  for full austenitisation and then cooled to room temperature under various cooling rate ranging from 0.3 to 70°C/s (0.3, 1, 3, 9, 25 and 70°C/s). The measured  $A_{c3}$  and  $M_s$  temperature are presented in Table 12 and the CCT diagrams are plotted based on the dilatometer results in Figure 87-94.

**Table 12 The  $A_{c3}$  and  $M_s$  temperature measured by the dilatometer**

<b>Alloy</b>	<b><math>A_{c3}</math> (Celsius)</b>	<b><math>M_s</math> (Celsius)</b>
#1	850	315
#2	920	315
#3	830	330
#4	870	325
#5	880	335
#6	830	325
#7	840	330
#8	810	320

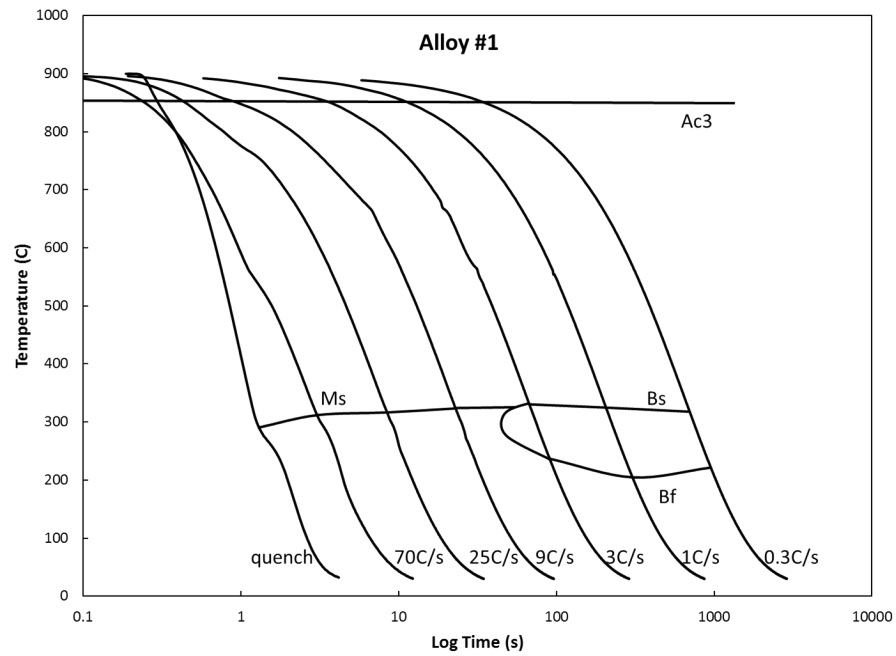


Figure 87 CCT diagram of alloy #1

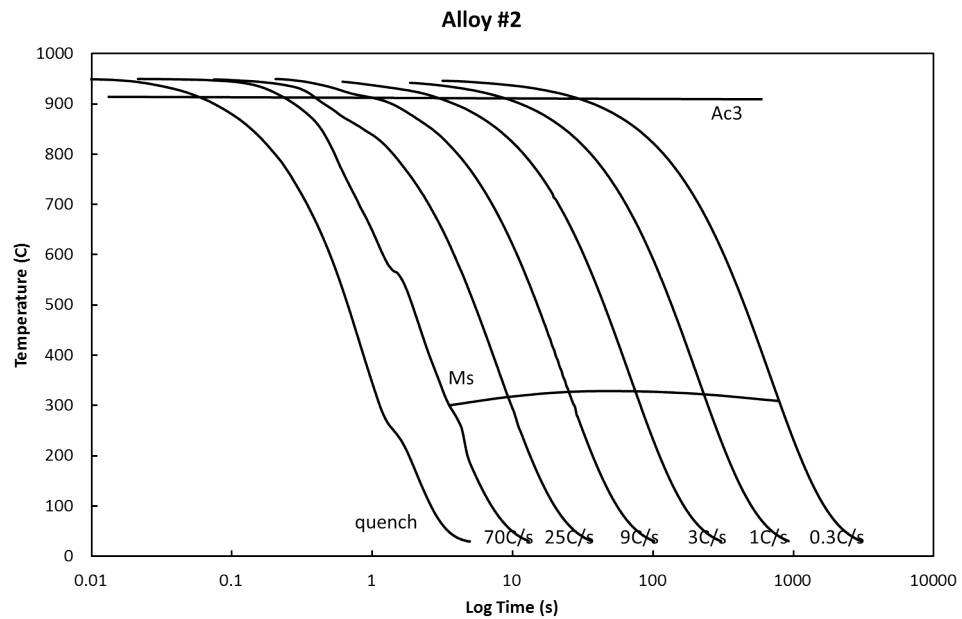


Figure 88 CCT diagram of alloy #2

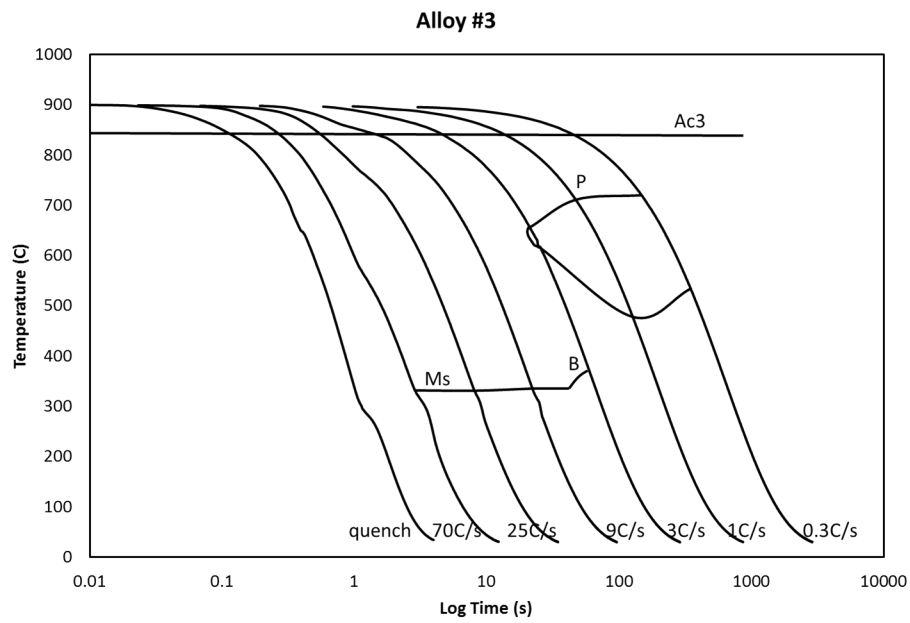


Figure 89 CCT diagram of alloy #3

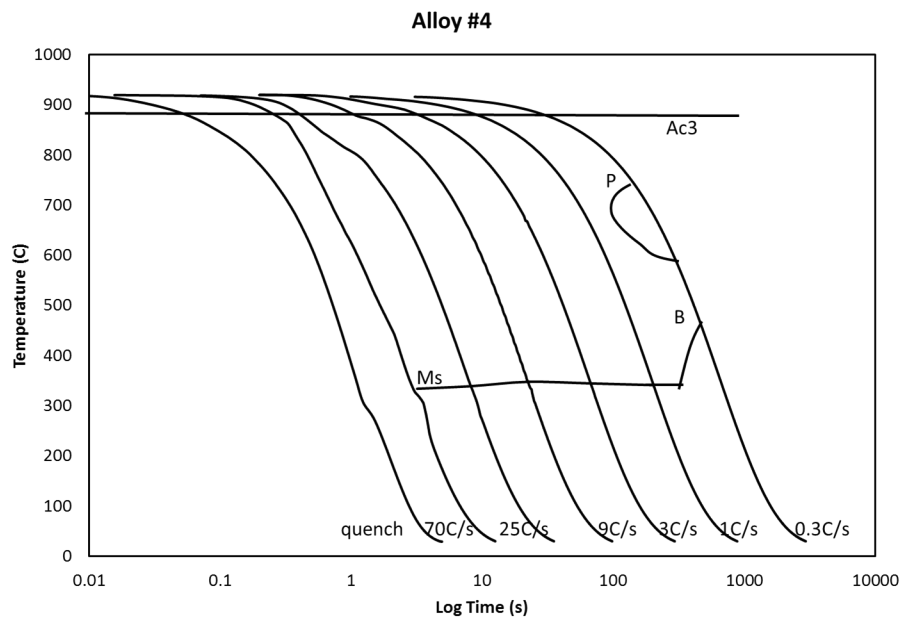
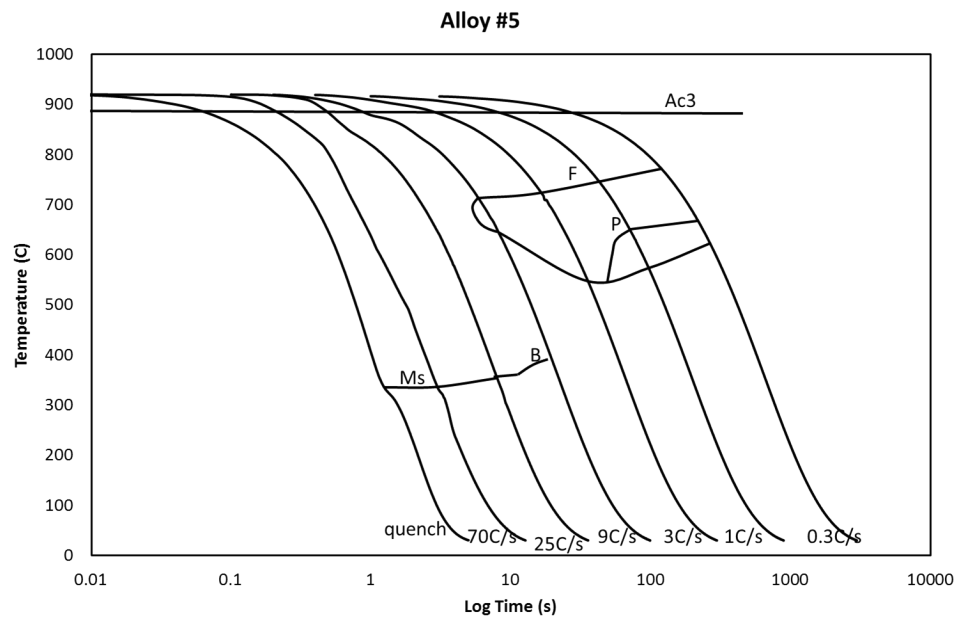
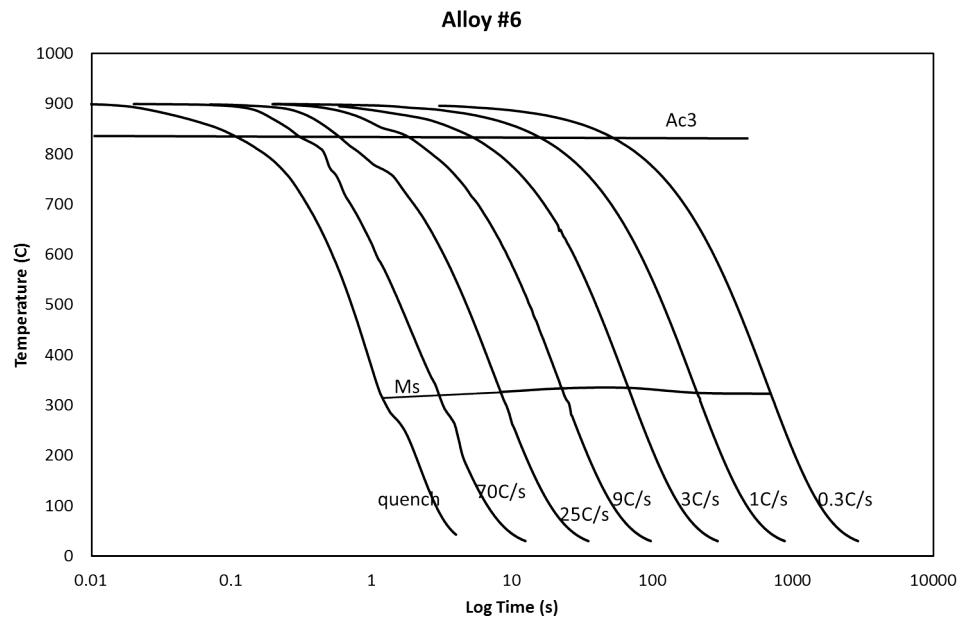


Figure 90 CCT diagram of alloy #4



**Figure 91 CCT diagram of alloy #5**



**Figure 92 CCT diagram of alloy #6**



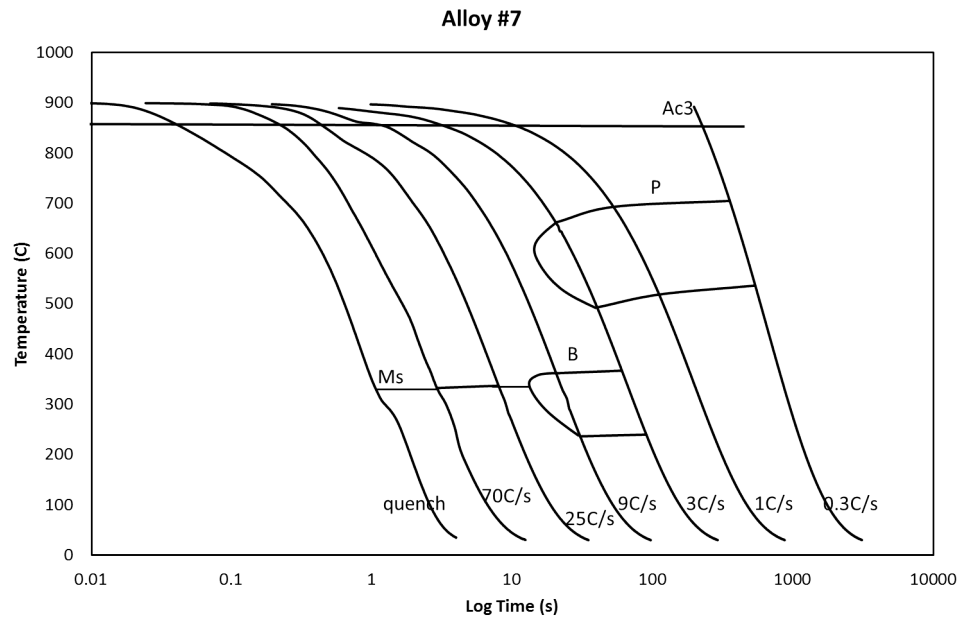


**Figure 93 CCT diagram of alloy #7**

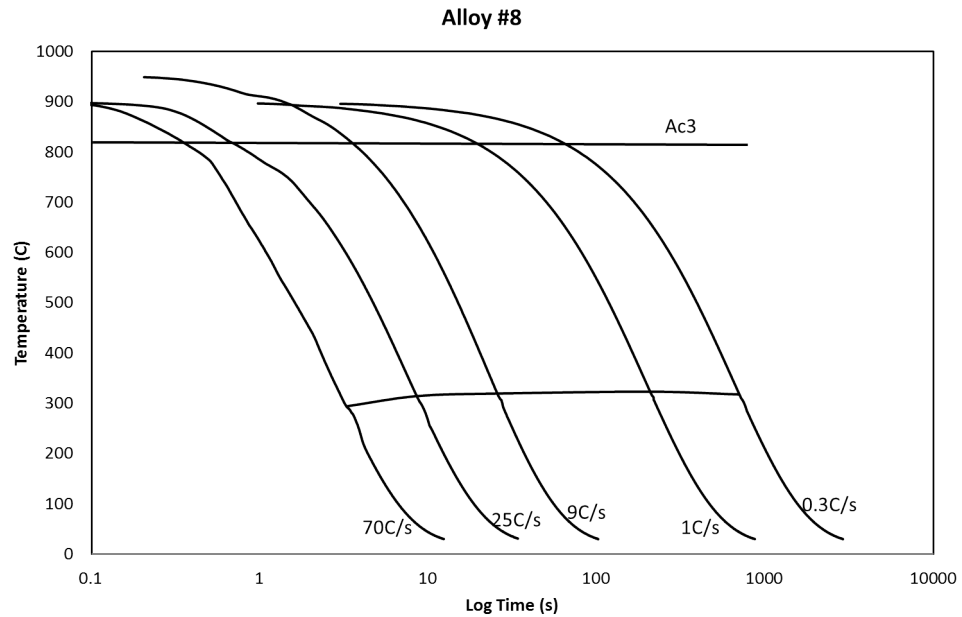


**Figure 94 CCT diagram of alloy #8**

Based on these computed CCT diagrams of alloy #1-8, it shows that some alloys are

suitable for carbide free bainite transformation and some are not. The differences between the  $M_s$  and  $B_s$  temperatures of alloy #1 and 7 are negligible. The bainite phase was not formed in the alloy #2, 6 and 8, even at the slowest cooling rate which is  $0.3^\circ\text{C/s}$  from the austenitisation stage to room temperature. Therefore, alloy # 1, 2, 6, 7 and 8 are not ideal candidates for bainite phase transformation. Moreover, in alloy #5 the proeutectoid ferrite or pearlite forms at the cooling rate between  $25^\circ\text{C/s}$  to  $9^\circ\text{C/s}$ . In order to produce only bainite phase, the cooling rate from the parent austenite phase needs to be at least  $25^\circ\text{C/s}$  to avoid any ferrite or pearlite formation. As result, alloy # 5 is not a good candidate for production of bainitic steel due to its low hardenability. For alloy #3, the bainite can be formed at cooling rate slower than  $9^\circ\text{C/s}$ . Based on the CCT diagram of this alloy, the isothermal bainite transformation heat treatment procedure can be designed. The specimen of alloy #3 need to be austenitized at temperature above  $830^\circ\text{C}$  and then cooled to the temperature range between  $330^\circ\text{C}$  and  $380^\circ\text{C}$  with cooling rate of  $9^\circ\text{C/s}$ . This heating procedure is applicable in laboratory making carbide free bainitic steel. It is a similar case for alloy #4 that the specimen can be cooled to a temperature range between  $325$  and  $480^\circ\text{C}$  with cooling rate faster than  $1^\circ\text{C/s}$ . In conclusion, alloy #3 and 4 are the best candidates for the production of the carbide free bainitic steel.

## **6 Conclusion and Future Work**

### **6.1 Summary of results and trends**

#### **6.1.1 Correlation of tensile strength with microstructure**

The highest tensile strength is achieved at the shortest transformation time (highest martensite fraction). With increasing bainitic transformation time, the strength of the steel decreases and the uniform elongation increases. There is an inverse relationship between bainitic ferrite platelet thickness and the yield strength. The ferrite lath refinement is the main microstructural contributor to the yield strength.

#### **6.1.2 Work-hardening response**

The gradual yielding (i.e. extended elasto-plastic transition) of the material is responsible for the high apparent work-hardening rate. The back-stresses measured by the Bauschinger test suggest that kinematic work hardening is a major contribution to the high work hardening behavior. The high work hardening rate of this carbide free bainitic steel is mainly due to the mixture of phases or elements with a variety of yield strengths in the microstructure. The elastic back stresses due to plastic incompatibility between different constituents in the carbide free bainitic steel can be measured by the Bauschinger test. This Bauschinger effect plays an important role in the high initial

work hardening behavior of the carbide free bainitic steel.

### **6.1.3 Banding structure**

The banding structure is composed by regions with different Mn content. As a result, the microstructure may be composed of bands with mainly martensite and bands with mainly bainite after bainite heat treatment. The banding structure may have a composite effect to the mechanical behavior, both on the strength and on the fracture. The material may be reinforced or embrittled by this banding structure depending on the thickness of the bands and the orientation corresponding to the applied stress. Moreover, residual stress between bands with mainly martensite and bainite after quenching also affect the mechanical response to deformation of the material. Since these factors are difficult to control or monitor, the intensity of banding should be reduced or minimized.

### **6.1.4 Aging effect**

The static strain aging effect at room temperature can not be overlooked in the carbide free bainitic steel. After isothermal bainite heat treatment, the yield strength of the material is increased by about 80MPa, and the ultimate tensile strength is improved by more than 100MPa after aging at room temperature for one week. It is mainly caused by the high dislocation density and over-saturated carbon content in the bainitic ferrite lath. The mobile carbon atoms can pin the dislocation from slipping, thus the yield strength is

improved after aging at room temperature. The residual stress within the microstructure after bainite transformation generates a driving force of carbon migration. Moreover, the true fracture strength is increased by 400MPa, and the area reduction undergoes a significant incrementation after aging for seven days. There is a transition of the fracture mechanism from brittle, intergranular fracture at short aging period to more ductile, transgranular fracture at longer aging time at room temperature. Examination of the fracture behavior indicated that the prior austenite grain boundaries play an important role in the fracture process. After aging, the prior austenite grain boundaries may be strengthened by the carbon dissipation, and reduce the possibility of crack initiation under deformation. Both hydrogen embrittlement and stress-corrosion cracking are studied to find out the main factor to cause the improvement in fracture resistance after aging at room temperature.

### **6.1.5 Retained austenite and TRIP effect**

The retained austenite in thin film can blunt crack propagation and prevent bainitic ferrite coarsening, thus it can directly improve the resistance to fracture and indirectly increase the strength of the material. The retained austenite with a significant amount of carbon is ultra-stable, which is proven by X-ray diffraction and TEM analysis. The possible contribution of the phase transformation from austenite to martensite (TRIP effect) to the high work-hardening rate is excluded in the present case because of the high carbon

content in austenite. The retained austenite is highly-enriched by carbon which is stabilized at room temperature with the  $M_s$  temperature estimated to be below room temperature.

### **6.1.6 Fracture behavior**

The fracture behavior of the carbide free bainitic steel is a transition from brittle, intergranular fracture at short transformation times to more ductile, transgranular fracture at long transformation times. After 30 minutes of bainite transformation, the fracture mechanism is brittle intergranular along the prior austenite grain boundaries. This gives inconsistent fracture behavior due to high volume fraction of martensite in the final product. With increasing bainitic transformation time, the fracture becomes more ductile as expected and the former austenite grain-boundaries appear to play a less important role in the fracture process. The ductile fracture may be controlled or triggered by decohesion of certain features of the microstructures due to solute segregation or plastic incompatibility stresses.

### **6.1.7 Mechanical behavior of ausformed CFB**

The motivation to study the ausformed carbide free bainitic steel is to accelerate the bainite transformation kinetics for industrial applications in the future. In all these previous studies on the effect of the ausforming process of the carbide free bainitic steel,

most of the focus is on the bainite transformation kinetics. In this work, the exclusive study on the ausforming of the carbide free bainitic steel is emphasizing on its final microstructure and its mechanical behavior.

Higher amount of retained austenite is stabilized at room temperature after the thermal-mechanical treatment. The ausformed structure has greater potential to transform to martensite during plastic deformation (the TRIP effect). Based on its mechanical behavior under tensile test and microstructural analysis by EBSD, the TRIP effect may contribute to the work hardening behavior. The ausformed carbide free bainite reaches higher uniform elongation as well as greater fracture resistance under uniaxial tensile deformation. This improvement in ductility and toughness is not only due to the fact that austenite is the softest phase in the final product, but also the TRIP effect that may occur during work hardening and crack propagation.

The changes in morphology and the variant selection of the bainitic ferrite lath in the ausformed carbide free bainitic steel were also investigated. More retained austenite grains were observed in granular shape by EBSD. The bainitic ferrite laths are finer in thickness after ausformation due to the dislocation substructures introduced during plastic deformation of the parent austenite phase. The bainitic ferrite grains are not only nucleated from the prior austenite grain boundaries but also at the ferrite/austenite interfaces. The variant selection of the bainitic ferrite lath in the ausformed material is

also found by EBSD analysis. The residual stress between austenite grains after ausforming affects the following bainite transformation. Since bainite formation is accompanied by shape change, there is some preferred variant from the parent austenite grain to compensate the existing residual stress in the parent phase. As a result, variant selection of bainitic ferrite is found within some parent austenite grain in the ausformed carbide free bainitic steel. The variant selection of the ausformed bainite depends on the level of the strain during ausforming.

## **6.2 Conclusion**

In conclusion, the great combination of strength and ductility of this carbide free bainitic steel is mainly due to the mixture of phases or elements with a variety of yield strength in the microstructure. The former austenite grain boundary is playing an important role in the fracture mechanism of the material, especially for the one with greater amount of martensite. Retained austenite is enriched in carbon due to the suppression of carbides in the microstructure. It not only contributes to the fracture resistance but also has the potential to cause TRIP effect during work hardening. The aging effect at room temperature can not be overlooked in the carbide free bainitic steel. It is mainly caused by the high dislocation density and over-saturated carbon content in the bainitic ferrite lath. The banded structure is the result of the high manganese content in the steel. Banding should be reduced or eliminated in order to avoid early failure and to attain



reproducible and consistent mechanical behavior. The effects of ausforming to the final microstructure and mechanical behavior of the carbide free bainitic steel have been investigated. Greater amount of retained austenite in the ausformed material (corresponding to a lower carbon content and a reduced stability) triggers the TRIP contributing to the work hardening behavior. The changes in morphology and variant selection of the bainitic ferrite lath in the ausformed carbide free bainitic steel are also observed.

### **6.3 Future work**

Future study on the ausforming of the the CFB steel may include further analysis on the mechanical behavior of the ausformed specimens. More tensile tests could be performed to the specimens ausformed by Gleeble in tension to study the fundamental mechanical properties including strength, ductility, work hardening and fracture mechanism. The Bauschinger test may also apply to study the residual stress in the ausformed CFB steel. In order to have a deeper understanding in the bainitic ferrite nucleation, growth and morphology during the thermo-mechanical procedure by Gleeble, it is worth to examine the microstructure of the specimen after shorter period of bainite transformation (5 or 10 minutes at 300°C) after deformation of austenite. Further EBSD analysis can be done on the ausformed material to study the variant selection in bainitic ferrite. The correlation between the dislocation slip bands in the prior austenite and the

morphology and texture of the microstructure.

Further analysis on the aging effect at room temperature of the CFB steel can be done in numbers of approaches. The carbon content of the bainitic ferrite lath and retained austenite film after aging at room temperature for different period of time can be studied by atom probe. Since the solubility of carbon in bainitic ferrite is negligible in room temperature, the interstitial carbon atoms tend to dissipate from the ferrite lath to the neighboring retained austenite films, dislocations or grain boundaries. This set of experiment using atom probe will give a quantitative analysis on the evolution the carbon concentration in bainitic ferrite and austenite with aging time at room temperature.

The banding structure of the CFB steel due to manganese segregation may be examined by Electron Probe Micro-Analysis (EPMA). EPMA performs quantitative elemental analysis including determine the elemental composition and the thickness from nanometer to millimeter by recording WDS spectra (Wavelength Dispersive Spectroscopy). Due to the internal property of WDS, it gives more accurate result than standard EDS (Energy Dispersive Spectroscopy). [ref] The quantitative manganese segregation distribution may be examined by EPMA to further calculate the homogenization procedure and determine the correlation between the banding structure and the mechanical behavior of the CFB steel.

## Reference

- [1] Matlock, D. K. and Speer, J. G. (2009). *Microstructure and Texture in Steels and Other Materials*. (p. 185). (A. Haldar, S. Suwas and D. Bhattacharjee, Eds.) India: Springer Science & Business Media.
- [2] Hell, J. C. et al. (2010). Microstructural and Mechanical Characterizations of Carbide-free Bainitic Steels. In *Proceedings of the 2nd International Conference on Super-High Strength Steels SHSS*. Italy.
- [3] Altstetter, C. J., Bentley, A. P., Fourie, J. W., Kirkbride, A. N. (1986). *Mater. Sci. Eng.*, 82, 13.
- [4] Karbasian, H. and Tekkaya, A. E. (2010). *Journal of Materials Processing Technology*, 210, 2103–2118.
- [5] Suehiro, M., Kusumi, K., Miyakoshi, T., Maki, J. and Ohgami, M. (2003). *Nippon Steel Tech. Rep.*, No. 88, 16.
- [6] Turetta, A., Bruschi, S. and Ghiotti, A. (2006). *J. Mater. Process. Technol.*, 177, 396.
- [7] Bhadeshia, H. K. D. H. and Edmonds, D. V. (1983). *Metal Science*, 17, 420.
- [8] Caballero, F. G., Bhadeshia, H. K. D. H., Mawella, J. A., Jones, D. G. and Brown, P. (2001). *Mater Sci Technol.*, 17, 512-516.
- [9] Caballero, F. G., Bhadeshia, H. K. D. H., Mawella, K. J. A., Jones, D. G., and Brown, P. (2001). *Materials Science and Technology*, 17, 517-522.

- [10] Caballero, F. G. and Bhadeshia, H. K. D. H. (2004). *Current Opinion in Solid State and Materials Science*, 8, 251-257.
- [11] Garcia-Mateo, C. and Caballero, F. G. (2005). *Materials Transactions*, 46, 1839-1846.
- [12] Somers, B. R. (1993). Introduction to the selection of carbon and low-alloy steels, in: *ASM handbook*, 6<sup>th</sup> ed., ASM International, Metals Park, Ohio.
- [13] Caballero, F. G., Santofimia, M. J., Garcia-Mateo, C., Chao, J. and Garcia de Andres, C. (2009) *Materials and Design*, 30, 2077-2083.
- [14] Caballero, F. G., Garcia-Mateo, C., Capdevila, C. and Garcia de Andres, C. (2007) *Materials and Manufacturing Processes*, 22, 502-506.
- [15] Allain, S. and Iung, T. (2008). *Revue de Metallurgie*, 105, 520-530.
- [16] Sugimoto, K. I. (2009). *Materials Science and Technology*, 25, No. 9, 1108-1117.
- [17] Soliman, M., Mostafa, H., El-Sabbagh, A. S. and Palkowski, H. (2010). *Materials Science and Engineering A*, 527, 7706-7713.
- [18] Putatunda, S. K., Singar, A. V., Tackett, R. and Lawes, G. (2009). *Materials Science and Engineering A*, 513–514, 329–339.
- [19] Graville, B. A. (1976). Cold cracking in welds in HSLA steels. in: *Welding of HSLA (microalloyed) structural steels*, Proc. Int. Conf., American Society of Metals.
- [20] Davenport, E. S. and Bain, E. C. (1930). *Trans. TMS-AIME*, 90, 117-154.

- [21] Bhadeshia, H. K. D. H. (2001). *Bainite in steels*. London: Institute of Materials.
- [22] Kumar, R. (1968). *Physical Metallurgy of Iron and Steel*,. Bombay: Asia Publishing House.
- [23] Singh, S. B. (2012). *Mechanisms of bainite transformation in steels in Phase Transformations, in Steels: Fundamentals and Diffusion-controlled Transformations*. (E. Pereloma and D. Edmonds, Eds.) Cambridge: Woodhead Publishing.
- [24] Hehemann, R. F. (1970). *The bainite transformation, in Phase transformations*. (H. Aaronson and V. Zackay, Eds.) Metals Park, OH: ASM.
- [25] Bhadeshia, H. K. D. H. (1990). *Metallurgy, welding, and qualification of microalloyed (HSLA) Steel Weldments*. (J. Hickey, D. Howden, & M. Randall, Eds.) Miami, FL: American Welding Society.
- [26] Oblak, J. M. and Hehemann, R. F. (1967). *Transformations and Hardenability in Steels* (pp. 15-30). Ann Arbor, MI: Climax Molybdenum.
- [27] Hehemann, R. F., Kinsman, K. R. and Aaronson, H. I. (1972). *Metall Mat. Trans.*, 3, 1077-1094.
- [28] Pickering, F. B. (1967). *Transformations and Hardenability in Steels* (pp. 109-132). Ann Arbor, MI: Climax Molybdenum.
- [29] Mehl, R. (1939). *Mechanism and rate of decomposition from austenite. In Hardenability of alloy steels* (p. 1–65). ASM.

- [30] Singh, S. B. and Bhadeshia, H. K. D. H. (1998). *Materials Science and Engineering A*, 245A, 72-79.
- [31] Furuhashi, T., Kawata, H., Morito, S. and Maki, T. (2006). *Materials Science and Engineering A*, 431, 228-236.
- [32] Sawada, M., Tsuzaki, K. and Maki, T. (1994). *Unpublished Research*, Kyoto University.
- [33] Ohmori, Y., Ohtani, H. and Kunitake, T. (1971). *Transactions ISIJ*, 11, 250-259.
- [34] Habraken, L. J. and Economopolous, M. (1967). *Transformations and Hardenability in Steels* (pp. 69–108). Ann Arbor, MI: Climax Molybdenum.
- [35] Vilella, J. R. (1940). *Trans. AIME*, 140, 332.
- [36] Hillert, M. (1957). *Jernkontoret. Ann.*, 141, 757.
- [37] Josefsson, B. and Andren, H. O. (1988). *Proc. 35th International Field Emission Symposium, IFES 88* (pp. 18–22). (M. K. Miller, Ed.) Oak Ridge, TN: J. de Phys. 49–C6.
- [38] LeHouillier, R., Begin, G and Dube, A. (1970). *Metall. Mat. Trans. A*, 2, 2645-2653.
- [39] Zajac, S., Komenda, J., Morris, P., Dierickx, P., Matera, S. and Penalba, F. (2005). *Quantitative structure–property relationship for complex bainitic microstructures in Technical Steel Research report no. EUR 21245EN*, Luxembourg: European Commission.

- [40] Reed Hill, R. E. (1973). *Physical Metallurgy Principles* (2nd ed.). New York: D. Van Nostrand Company.
- [41] Porter, D. A., Easterling, K. E. and Sherif, M. Y. (2009). *Phase Transformations in Metals and Alloys* (3rd ed.). Hoboken: CRC Press.
- [42] Lee, H. J., Spanos, G., Shiflet, G. J., Aaronson, H. I. (1988), *Acta Metallurgica*, 36, 1129-1140.
- [43] Hultgren, J.(1926), *J. Iron. Steel Inst.*, 114, 421–422.
- [44] Wever, F. and Jellinghaus, W. (1932). *Transformation kinetics of austenite II. dilatometry investigations of austenite decomposition* (Vol. 14, p. 85). Eisenforch: Mitt. Kaiser-Wilhelm-Inst.
- [45] Portevin, A. and Chevenard, P. (1937). *The transformations during the cooling of steels* (204, p. 772). P. Compt. Rend.
- [46] Zener, C. (1946), *Trans. Am. Inst. Min. Metall. Eng.*, 167, 550–595.
- [47] Vilella, J. R., Guellich, G. E. and Bain, E. C. (1936), *Trans. ASM*, 24, 225–261.
- [48] Ko, T. and Cottrell, S. A. (1952), *J. Iron. Steel Inst.*, 172, 307–313.
- [49] Speich, G. R. and Cohen, M. (1960), *Trans. Metall. Soc. AIME*, 218, 1050–1059.
- [50] Goodenow, R. H., Matas, S. J. and Hehemann, R. F. (1963), *Trans. Met. Soc. AIME*, 227, 651–658.
- [51] Bhadeshia, H. K. D. H. and Christian, J. W. (1990), *Metall. Mat. Trans. A*,

21A,767-797.

- [52] Bhadeshia, H. K. D. H. and Honeycombe, S. R. (2006). The bainite reaction. In *Steels: Microstructure and Properties* (3rd ed., pp. 129-154). Oxford: Butterworth-Heinemann.
- [53] Fielding, L. C. D. (2013), *Materials Science and Technology*, 29, 383-399.
- [54] Swallow, E. and Bhadeshia, H. K. D. H. (1996). *Materials Science and Technology*, 12, 121-125.
- [55] Robertson, J. M. (1929) *J. Iron. Steel Inst.*, 119, 391–424.
- [56] Hultgren, A. (1947) *Trans. ASM*, 39, 915–1005.
- [57] Hillert, M. (1953). *Paraequilibrium* in *Technical report*. Stockholm: Swedish Institute for Metals Research.
- [58] Davenport, E. S. (1939). *Trans. ASM*, 27, 837–886.
- [59] Hillert, M. (1960). *The Growth of Ferrite, Bainite and Martensite* in *Internal report*, Stockholm, Swedish Institute for Metals Research
- [60] Simonen, E. P., Aaronson, H. I. and Trivedi, R. (1973). *Metall. Trans.*, 4,1239.
- [61] Chattopadhyay, K. (1985). *Materials Science Forum*, 3, 231-246.
- [62] Aaronson, H. I. (1969). *The Mechanisms of Phase Transformations in Crystalline Solids* (pp. 270-281). London: The Institute of Metals.
- [63] Aaronson, H. and Zackay, V. (1962). *Decomposition of Austenite by Diffusional*



*Processes*. New York: Interscience

- [64] Townsend, R. D. and Kirkaldy, J. S. (1968). *Trans ASM*, 61, 605-619.
- [65] Simonen, E. P., Aaronson, H. I. and Trevedi, R. (1973). *Metall. Mat. Trans. A*, 4, 1239-1245
- [66] Shackleton, D. N. and Kelly, P. M. (1967). *Acta Metall.*, 15, 979-992.
- [67] Klier, E. P. and Lyman, T. (1944). *Trans. AIMME. Met. Technol.*, 395–422.
- [68] Aaronson, H. I., Laird, C. and Kinsman, K. R. (1970). *Phase Transformations* (pp. 313-396). Metals Park, OH: ASM.
- [69] Miodownik, A. P. (1956). *Inst. Met. Monograph Rep.*, 18, 319.
- [70] Ko, T. and Cottrell, S. A. (1952), *J. Iron. Steel Inst.*, 172, 307–313.
- [71] Bowles, J. S. and Mackenzie, J. K. (1954). *Acta Metall.*, 2, 129–138.
- [72] Fang, H., Yang, J., Yang, Z. and Bai, B. (2002). *Scr. Mater.*, 47, 157–162.
- [73] Sandvik, B. P. J. (1982). *Metallurgical Transactions A*, 13A, 777-787.
- [74] Moritani, T. (2003). *PhD Thesis*. Kyoto University.
- [75] Shackleton, D. N. and Kelly, P. M. (1965). Morphology of bainite. In *Physical properties of martensite and bainite* (Vol. Special Report 93, p. 126–134). London: Iron and Steel Institute.
- [76] Mehl, R.F., Barrett, C.S. and Smith, D. W. (1933). *Trans. AIME*, 105, 215-258.
- [77] Irvine, K. J. and Pickering, F. B. (1963). *J. Iron Steel Inst.* 201, 518–531.

- [78] Hahn, G. T., Averbach, B. L., Owen, W. S., and Cohen, M. (1959). *Proceedings of Swampscott Conference on Fracture* (p. 91–114). (B.L. Averbach, D.K. Felbeck, G.T. Hahn, D.A. Thomas, Eds.) New York: Wiley.
- [79] Edmonds, D. V. and Cochrane, R. C. (1990). *Metallurgical Transactions A*, 21A, 1527-1540.
- [80] Bhadeshia, H. K. D. H. and Edmonds, D. V. (1983). *Metal Science*, 17, 411.
- [81] Miihkinen, V. T. T. and Edmonds, D. V. (1987). *Mater. Sci. Technol.*, 3, 441-49.
- [82] Bhadeshia, H. K. D. H., and Honeycombe, R. W. K. (2011). *Steels: Microstructure and Properties* (3rd ed.). Amsterdam: Elsevier, Butterworth-Heinemann.
- [83] Juvinall, R., and Marshek, K. (2006). *Fundamentals of machine component design* (4th ed., p. 69). New York: J. Wiley.
- [84] Petty, E. R. (1970). *Physical Metallurgy of Engineering Materials*. London: George Allen and Unwin.
- [85] Bhadeshia, H. K. D. H. and Edmonds, D. V. (1979). *MetaU. Trans. A*, 10A, 895-907.
- [86] Kirkaldy, J. S., Destinon-Forstmann, J. and Brigham, R. J. (1962). *Canadian Metallurgical Quarterly*, 59, 59-81.
- [87] Thompson, S. W., Howell, P. R. (1992). *Mater. Sci. Technol.*, 8, 777–784.
- [88] Courtney, T. H. (2005). *Mechanical Behavior of Materials* (2nd ed.). Long Grove, IL: Waveland Press.

- [89] Hosford, W. F. (2010). *Mechanical Behavior of Materials* (2nd ed.). Cambridge: University Press.
- [90] Bhadeshia, H. K. D. H. (1982). *Metal Sci.*, *16*, 159–165.
- [91] Bhadeshia, H. K. D. H. (2005). Hard Bainite. In *Solid Phase Transformations in Inorganic Materials* (Vol. 1, pp. 469-484). TMS.
- [92] Caballero, F. G., Bhadeshia, H. K. D. H., Mawella, K. J. A., Jones, D. G. and Brown, P. (2002). *Mater. Sci. Technol.*, *18*, 279–284.
- [93] Parker, R. (1977). *Metall. Trans.*, *8A*, 1025.
- [94] Sandvik, B.P.J. and Nevalainen, H.P. (1981). *Met. Technol.*, *15*, 213-220.
- [95] Chang, L.C. and Bhadeshia, H. K. D. H. (1995). *Mater. Sci. Tech.*, *11*, 874-881.
- [96] Nemoto, M. (1974). *High voltage electron microscopy* (p. 230). New York: Academic Press.
- [97] Cornide, J., Miyamoto, G., Caballero, F. G., Furuhashi, T., Miller, M. K. and Garcia-Mateo, C. (2011). *Solid State Phenomena*, *172-174*, 117-122.
- [98] Irani, J. S. (1967). *British Iron and Steel Research Association Rep. No. MG/A/60/67*. London: BISRA.
- [99] Edwards, R.H. and Kennon, N.F. (1978). *Metall. Trans. A*, *9A*, 1801-09.
- [100] Fondkar, M. K., Rao, A. M. and Mallik, A. K. (1970). *Metall. Trans.*, *1*, 885.
- [101] Kinsman, K. R. and Aaronson, H. I. (1967). *Transformations and Hardenability*

- in Steels* (pp. 33-38). Ann Arbor, MI: Climax Molybdenum.
- [102] Vasudevan, P., Graham, L. W., and Axon, H. J. (1958). *J. Iron Steel Inst.*, 190, 386-91.
- [103] Bhadeshia, H. K. D. H. and Waugh, A. R. (1982). *Acta Metall.*, 30, 775-84.
- [104] Stark, I. (1988). *D.Phil. Dissertation*. Oxford: University of Oxford.
- [105] Zhang, M. X. and Kelly, P. M. (1998) *Mater. Character.*, 40, 159–168.
- [106] Peet, M., Babu, S. S., Miller, M. K. and Bhadeshia, H. K. D. H. (2004). *Scripta Mater.*, 50, 1277–1281.
- [107] Caballero, F. G., Miller, M. K., Mateo, C. G., Capdevila, C. and Babu, S. S. (2008). *Acta Mater.*, 56, 188–199.
- [108] Cottrell, A. H. and Bilby, B. A. (1949). *Proc. Phys. Soc. A*, 62, 49-62.
- [109] Hehemann, R. F., Kinsman, K. R. and Aaronson, H. I. (1972). *Met Trans.*, 3, 1077-1093.
- [110] Miihkinen, V. T. T. and Edmonds, D. V. (1987). *Mater. Sci. Technol.*, 3, 422-431.
- [111] Miihkinen, V. T. T. and Edmonds, D. V. (1987). *Mater. Sci. Technol.*, 3, 432-441.
- [112] Garcia-Mateo, C., Caballero, F. G., Bhadeshia, H. K. D. H. (2003). *J. Phys. Colloque*, 112, 285–288.

- [113] Garcia-Mateo, C., Caballero, F. G. and Bhadeshia, H. K. D. H. (2003). *ISIJ Int.*, 43, 1238-1243.
- [114] Caballero, F.G., Chao, J., Cornide, J., García-Mateo, C., Santofimia, M. J., Capdevila, C. (2009). *Materials Science and Engineering A*, 525, 87–95.
- [115] Sugimoto, K. I., Nakano, K., Song, S. M., Kashima, T. (2002). *ISIJ International*, 42, No. 4, 450–455.
- [116] Sugimoto, K. I., Iida, T., Sakaguchi, J., Kashima, T. (2000). *ISIJ International*, 40, No. 9, 902–908.
- [117] Sugimoto, K. I., Sakaguchi, J., Iida, T., Kashima, T. (2000). *ISIJ International*, 40, No. 9, 920–926.
- [118] Sugimoto, K. I., Muramatsu, T., Hashimoto, S. I., Mukai, Y. (2006). *Journal of Materials Processing Technology*, 177, 390-395.
- [119] Sugimoto, K. I., Murata, M and Song, S. M. (2010). *ISIJ International*, 50, No. 1, 162–168.
- [120] Hell, J. C. (2011). *D.Phil. Dissertation*. Metz: L'Universite Paul Verlaine De Metz.
- [121] Valiev, R. Z., Islamgaliev, R. K. and Alexandrov, I. V. (2000). *Prog. Mater. Sci.*, 45, 103.
- [122] Sugimoto, K., Kanda, A., Kikuchi, R., Hashimoto, S., Kashima, T. and Ikeda, S.

- (2002). *ISIJ International*, 42, 910-15.
- [123] Sugimoto, K., Tsunezawa, M., Hojo, T. and Ikeda, S. (2004). *ISIJ International*, 44, 1608.
- [124] Caballero, F., Miller, M., and Garcia-Mateo, C. (2010). *Acta Materialia*, 58, 2338-2343.
- [125] Ryu, J. H., Kim, D. I., Kim, H. S., Bhadeshia, H. K. D. H. and Suh, D. W. (2010). *Scripta Materialia*, 63, 297–299
- [126] Sinha, A. K. (2003). *Physical metallurgy handbook*. New York: McGraw-Hill.
- [127] Diehl, J. Z. (1956). *Metallkunde*, 47, 331.
- [128] Kocks, U. F. and Mecking, H. (2003). *Progress in Materials Science*, 48, 171-273.
- [129] Prager, W. (1955). *Proc. Inst. Mech. Eng., London*, 169, 41.
- [130] Sowerby, R., Uko, D. K. and Tomita, Y. (1979). *Materials Science and Engineering*, 41, 43-58.
- [131] Fisher, J. C., Hart, E. W. and Pry. R. H. (1953). *Acta Met.*, 1, 336.
- [132] Masing, G. (1923). *Wiss. Veroff. Siemens-Werken*, 3, 231.
- [133] Asaro, R. J. (1975). *Acta Metall.*, 23, 1255-1265.
- [134] Baird, J. D. (1963). *Strain Ageing of Steel – A Critical Review*, reprinted from Iron and Steel.

- [135] Liu, A. F. (2005). *Mechanics and mechanisms of fracture an introduction*.  
Materials Park, Ohio: ASM International.
- [136] Benham, P. P., Crawford, R. J., and Armstrong, C. G. (1996). *Mechanics of Engineering Materials*, 2nd ed., Burnt Mill: Longman Group Limited
- [137] Wulpi, D. J. (1999). *Understanding How Components Fail*, 2nd ed., ASM international.
- [138] Puttick, K. E. (1959). *Philos. Mag.*, 4, 964-969.
- [139] Becker, W. T. and McGarry, D. (2002). *Mechanisms and Appearances of Ductile and Brittle Fracture in Metals*. In *ASM Handbook, Failure Analysis and Preventions* (Vol. 11, pp. 587-626). ASM International.
- [140] Brooks, C. R. and Choudhury, A. (2002). *Failure Analysis of Engineering Materials*. McGraw-Hill.
- [141] Becker, W. T. and Lampman, S. (2002). *Mechanisms and Appearances of Ductile and Brittle Fracture in Metals*. In *ASM Handbook, Failure Analysis and Preventions* (Vol. 11, pp. 559-586). ASM International.
- [142] Atlas of Fractographs. In *ASM Handbook, Fractography* (Vol. 12, pp. 223).  
ASM International.
- [143] Inoue, T., Matsuda, S., Okamura, Y., and Aoki, K. (1970). *Trans. Jpn. Inst. Met.*, 11, 36-43

- [144] Lampman, S. (2002). *Intergranular Fracture*. In ASM Handbook, Failure Analysis and Prevention (Vol. 11, pp. 641-649). ASM International.
- [145] Zackey, V. F., et al., (1963). *The Relation between Microstructure and Mechanical Properties* (p. 847). London: H. M. S. O.
- [146] Singh, S. B. and Bhadeshia, H. K. D. H. (1996). *Mater. Sci. Technol.*, 12, 610.
- [147] Maki, T. (1993). *The Minerals, Metals and Materials Society* (p. 3–16) (K. A. Taylor, Ed.). Warrendale.
- [148] Freiwillig, R., Kudrman, J. and Chraska, P. (1976) *Metal Trans A*, 7A, 1091.
- [149] Jin, X. J., Min, N., Zheng, K. Y., Hsu, T. Y. and Xu, Z. Y. (2006). *Mater Sci Eng A*, 170, 438–440.
- [150] Bhadeshia, H. K. D. H. (1999). *Mater Sci Eng A*, 58, 273–275.
- [151] Shipway, P. H. and Bhadeshia, H. K. D. H. (1995). *Mater Sci Technol*, 11, 1116.
- [152] Chiou, C. S., Yang, J. R. and Huang, C. Y. (2001). *Mater Chem Phys*, 69, 113.
- [153] Larn, R. H. and Yang, J. R. (2000). *Mater Sci Eng A*, 278, 278.
- [154] Yang, J. R., Huang, C. Y., Hseich, W. H. and Chiou, C. S. (1996). *Mater Trans JIM*, 37, 579.
- [155] Lee, C. H., Bhadeshia, H. K. D. H. and Lee, H. C. (2003). *Mater Sci Eng A*, 360, 249.
- [156] Xu, G. (2010). *Internal Project Report*, McMaster University.



- [157] Debourg A. (2009). *Summer Project Report*, McMaster University.
- [158] Stoltz, R. E. and Pelloux, R. M. (1976). *Metallurgical Transactions A (Physical Metallurgy and Materials Science)*, 7, 1295-1306.
- [159] Wang, X. (2011). *Internal Project Report*, McMaster University.
- [160] Rundman, K. B., Moore, D. J., Hayrynen, K. L., Dubensky, W. J., and Rouns, T. N. (1988). *J. Heat Treat.*, 5, 79-95.
- [161] Pampillo, C. A. and Paxton, H. W. (1972). *Metall. Trans*, 3A, 2895.
- [162] Pande, C. S., Masumura, R. A. and Armstrong, R. W. (1993). *Nanostructured MATERIALS*, 2, 323-331.
- [163] Brozzo, P., Buzzichelli, G., Mascanzoni, A. and Mirabile, M. (1977). *Met. Sci.*, 11, 123-29.
- [164] Bhadeshia, H. K. D. H. (2010). *Proc. R. Soc. A*, 466, 3–18.
- [165] Harynen, K. L., Moore, D. J. and Rundman, K. B. (1990). *AFS Trans.*, 98, 471.
- [166] Masing, G. (1926). *Proc. 2nd Int. Congr. Applied Mechanics* (p. 332–335). Zurich.
- [167] Kocks, U. F. (1976). *J. Eng. Mater. Tech.*, 98, 76-85.
- [168] Mecking, H. and Kocks, U. F. (1981). *Acta Metallurgica*, 29, 1865-1875.
- [169] Brenner, S. S. (1958). *Growth and Perfection of Crystals* (p. 157–190) (R. H. Doremus, B. W. Roberts and D. Turnbull, Eds.). New York: Wiley.

- [170] Dieter, G. E. (1986). *Mechanical Metallurgy* (3rd ed., p. 283). New York: McGraw-Hill Book.
- [171] Wang, X., Zurob, H. S., Xu, G., Ye, Q., Bouaziz, O. and Embury, D. (2013). *Metallurgical and Materials Transactions A*, 44, 1454-61.
- [172] Kalish, D. and Cohen, M. (1970). *Mater Sci Eng*, 6, 156-166.
- [173] Caballero, F. G., Miller, M. K., Babu, S. S. and Garcia-Mateo, C. (2007). *Acta Materialia*, 55, 381–390.
- [174] Totten, G. (2002). *Handbook of residual stress and deformation of steel*. Materials Park, OH: ASM International. And references within.
- [175] Gorsky, W. S., Phys. (1935). *Zeitschr. Sowjetunion*, 8, 457.
- [176] Jacques, P. J. (1998). *PhD thesis*. UCL.
- [177] Caballero, F. G., Garcia-Mateo, C., Santofimia, M. J., Miller, M. K. and García de Andrés, C. (2009). *Acta Mater.*, 57, 8–17.
- [178] Hell, J., M. Dehmas, S., Allain, J., Prado, M., Hazotte, A. and Chateau, J. (2011). *ISIJ International*, 51, 10, 1724-1732.
- [179] Tasan, C. C., Hoefnagels, J. P. M. and Geers, M. G. D. (2010). *Scr. Mater.* 62, 835-838.
- [180] Kunio, T., Shimizu, M., Yamada, K. and Suzuki, H. (1975). *Eng. Fract. Mech.* 7, 411-417.

- [181] Liu, C. T., White, C. L. and Horton, J. A. (1985). *Acta Metall.*, 33, 2, 213-229.
- [182] Grabke, H., Tauber, G., and Viefhaus, H. (1975). *Scr. Metall.*, 9, 1181.
- [183] Khlestov, V. M., Konopleva, E. V. and McQueen, H. J. (1998). *Can Metall Quart*, 37, 75.
- [184] Strife, J. R., Carr, M. J. and Ansell, G. S. (1976). *Metall Trans A*, 8, 1471.
- [185] Tsuzaki, K., Fukasaku, S., Tomota, Y. and Maki, T. (1991). *Mater Trans JIM*, 32, 222.
- [186] Gong, W., Tomota, Y., Adachi, Y., Paradowska, A. M., Kelleher, J. F. and Zhang, S. Y. (2013). *Acta Materialia*, 61, 4142-4154.
- [187] Hu, H. J., Zurob, H. S., Xu, G., Embury, D. and Purdy, G. R. (2015). *Materials Science and Engineering A*, 626, 34-40
- [188] Davenport, A. T. (1977). *TMS-AIME*, New York, USA, 517–536.
- [189] Umemoto, M., Bando, S. and Tamura, I., (1986). *Proc Int Conf Martensitic Transformation*, Tamura, I. et al eds., Sendai, Japan. The Jpn Inst Met, 1987, 595.
- [190] He, B. B., Xu, W. and Huang, M. X. (2015). *Philosophical Magazine*, 95, 11, 1150-1163
- [191] Wang, X. (2013). *Internal Project Report*, McMaster University.
- [192] Magee, C. L. (1966). *Ph.D. thesis*. Carnegie Mellon University.
- [193] Leblond, J. B., Devaux, J., and Devaux, J. C. (1989). *Int. J. Plasticity*, 5,

551-572.

- [194] Olson, G. B. *Deformation, Processing and Structure*: American Society for Metals, (pp. 391-424). (1982). Metals Park, Ohio: American Society for Metals.